Design of Ultra Precision Fixtures for Nano-Manufacturing

by

Kartik Mangudi Varadarajan

B.Tech., Mechanical Engineering (2003)

Indian Institute of Technology – New Delhi, INDIA

Submitted to the Department of Mechanical Engineering in
Partial Fulfillment of the Requirements for the Degree of
Master of Science in Mechanical Engineering

at the

Massachusetts Institute of Technology

February 2005

Signature of Author_____
Department of Mechanical Engineering
January 20, 2005

Certified by_____
Martin L. Culpepper
Rockwell International Assistant Professor of Mechanical Engineering
Thesis Supervisor

Accepted by_____
Professor Lallit Anand
Chairman, Department Committee on Graduate Students

Design of Ultra-Precision Fixtures for Nano-manufacturing

by

KARTIK MANGUDI VARADARAJAN

Submitted to the Department of Mechanical Engineering on
January 20, 2005 in Partial Fulfillment of the Requirements for the
Degree of Master of Science in Mechanical Engineering

ABSTRACT

This thesis presents the design, modeling, fabrication and experimental validation of an active precision fixturing system called the Hybrid Positioning Fixture (HPF). The HPF uses the principles of exact constraint, combined with principles and means of Nanomanipulation to fixture components with tens of nanometer accuracy and repeatability. Achieving this level of performance requires addressing three fundamental limitations of precision fixtures; (1) Elimination of stiction via integrated compliance, (2) Integration of sensors and actuators to enable correction of systematic and time variable alignment errors, and (3) Improvement of fixture contacts' stability and longevity via hard coatings. Conceptual and analytic models are developed for the integration of compliant elements, sensors and actuators within the fixture. The validity of these concepts/models is tested via a prototype HPF. Analytic models and design rules are provided to guide designers in the use of thin coatings for precision fixture contacts. These are based upon non-linear finite element analysis. The effects of hard and soft interlayer, which reduce coating stresses and improve coating adherence, are also analyzed.

The performance of the HPF is measured in two modes, passive (constant voltage supplied to piezoelectric actuators) and active (actuators supplied with different input voltages). The HPF is shown to be capable of 3σ, passive repeatability of 100nm in x, y, and repeatability of 2μradian in θx, θy and θz. Active tests indicate that the HPF is capable of accuracy of better than 5nm. The fixture is shown to have a load capacity of 450 N and stiffness of 7N/μm.

The combination of nanometer-level accuracy, repeatability and high load capacity make the HPF suitable for a range of current and emerging applications such as photonics packaging, mask to wafer alignment, nanomanufactring, nano-scale research experiments and automated transfer lines.

Thesis Supervisor: Martin L. Culpepper

Title: Rockwell International Assistant Professor of Mechanical Engineering

Acknowledgements

I would foremost like to thank my parents for providing me with the opportunity to pursue my goals and for their love and affection, which has been helped me through the most trying times.

I would like to thank my advisor Prof. Martin L. Culpepper for his guidance and constant motivation that has enabled me to complete my research work. I would also like to thank him for the opportunities that he has made available to me.

I would like to acknowledge my teachers at the Indian Institute of Technology at New Delhi (IIT-DELHI), who have shaped me both academically and personally.

I would like to thank all my lab mates at Precision Compliant Systems (PCS) Laboratory for keeping company during long days and nights spent working in the lab and for the enjoyable times outside of work.

Finally, I would like to acknowledge Gerald Wentworth and Mark Belanger of the Lab for Manufacturing and Productivity (LMP), for training and assisting me in using the equipment and manufacturing parts for my research.

Contents

List of Figures

List of Tables

Chapter 1 - Introduction

1.1 Motivation

The purpose of this research is to generate the knowledge required to design ultra-precision fixturing systems for nanometer-level accuracy and repeatability. This is important as maintaining acceptable costs and quality in many current and emerging products requires nanometer-level positioning and fixturing. For instance, the fields of photonics packaging, semiconductor test equipment, mask to wafer alignment and the like, require positioning in six axes with nanometer-level and micro-radian accuracy. In such applications, several parts might need to be positioned at many different machines, for instance in a manufacturing line. It is desirable that the fixturing system used to align and affix the part provide rapid, repeatable and accurate means to place and remove the parts. The stiffness and load capacity of fixtures are also important as these characteristics place limits on the fixture's accuracy and suitablility for various applications.

This work has focused on generating the knowledge engineers and scientists will need to design, fabricate and implement fixtures that satisfy the characteristics discussed above. Towards this end, this chapter will provide the reader with the background information required to understand the important characteristics of precision fixtures, nanomanipulators and the fundamental limitations that prevent the extension of current technologies to provide nanometer-level performance. A summary of the research approaches to addressing the fundamental limitations is also provided.

1.2 Precision fixture and positioning systems

1.2.1 Review of precision fixture technologies

A fixturing system or fixture provides means to locate or fix one component with respect to another. Numerous fixturing methods are utilized to achieve this. Typically they are passive and may be categorized into elastic-averaging and exact-constraint based methods. Elastic-averaging methods, for instance those shown in Figure 1.1, achieve precision by averaging errors over a large number of contact points. The averaging effect enables them to have high load capacity and stiffness. However they are by nature overconstrained, limiting their repeatability to about 5μm [1]. Here repeatability refers to the variation in position of the part over several cycles of placement and subsequent removal.

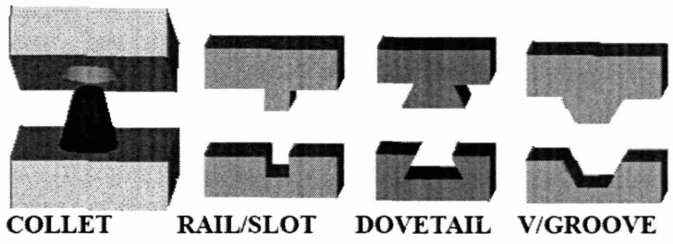

Figure 1.1: Elastically averaged alignment methods (figure by M.L. Culpepper, Design and Application of Compliant Quasi-Kinematic Couplings [1])

On the other hand, exact constraint methods have number of constraints exactly equal to the number of degrees of freedom to be controlled. This makes the system deterministic and exact-constraint methods such as kinematic couplings, may provide sub-micron repeatability. Figure 1.2 shows two common configurations of kinematic couplings. As such, kinematic couplings have long been used in instrumentation design to provide economical means to locate components precisely [2]. These couplings date back to the 1800's, when Willis, Kelvin and Maxwell used them as fixtures in their experiments [3]. Kinematic couplings achieve precise positioning by providing six constraints or small-

area contacts to define the six degrees of freedom of the system.

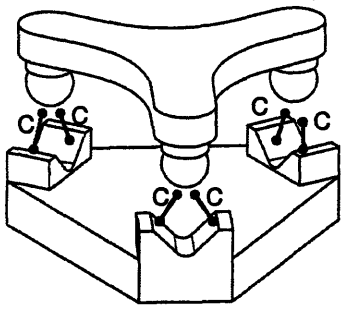

(a) Three - groove

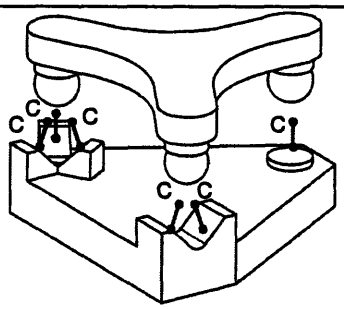

(b) Tetrahedron-flat-vee (Kelvin clamp)

Figure 1.2: Kinematic couplings, C = constraint (adaptation of figure by L.C. Hale, Principles and techniques for designing precision machines [4])

Much work has been done in formalizing the design process of these couplings [2,3]. Over the years these couplings and others, based on them, have been used in applications such as locating a chuck with respect to faceplate of a lathe [5], repeatable tool holders [6], locating parts onto machininig centers in an assembly line [7], Quasi-kinematic couplings for automotive assembly [1], two degree of freedom XY micro-stage [8], quick change industrial robot interface, modular high precision microscope [9] and the like. The principle limitations of traditional kinematic couplings were relatively low stiffness (compared to that of machine structure, approximately 50N/μm) and high contact stresses that limited their load capacity and life. These limitations were addressed through the use of high modulus ceramic materials and larger area contacts (canoe balls) [9]. Performance limitations resulting from contact friction have been partly addressed through the use of ceramic materials (repeatability approximately 0.3μm using SiN) [10] and more recently, by using low cost surface coatings [11]. More work is required to restrict friction-induced errors to below the nanometer-level. Incorporation of flexures within these coupling has also shown to reduce frictional hysteresis to 0.1μm [12]. This work has not addressed the use of flexures to improve repeatability.

From the past work, we know that kinematic couplings and other passive fixtures may generally be designed to have the requisite stiffness and load capacity for most

instrumentation and manufacturing applications. Unfortunately, the accuracy of passive fixtures is strongly coupled to manufacturing and assembly tolerances. Here accuracy refers to the deviation of the average position of the part from the desired location. As a result, a passively fixtured system may be repeatable but not necessarily accurate. It is for this reason that passive positioning methods require either repeated calibration or ultra precision fabrication methods to minimize errors due to manufacturing and assembly of the fixture components. Additionally, thermal errors, which are time variable, cannot be addressed with the use of passive fixtures.

To address this limitation, fixtures incorporating actuators and mechanisms, are being developed to provide active correction capability. One such fixture is the ARKC (Accurate and Repeatable Kinematic Coupling) which has 1σ repeatability of approximately $1.9\mu m/3.6\mu radian$ [13] and accuracy on the order of $1\mu m/10\mu radian$. This was a first step in providing accurate and repeatable fixtures, but the performance falls short of the nanometer-level goals of this work.

1.2.2 Review of generic positioning systems

Positioning systems that provide nanometer-level positioning, e.g. nanomanipulators, require active elements to sense and correct errors. The alignment elements of these machines are self-contained and therefore a locating interface is required to position parts with respect to the nanomanipulator. As such, these systems do not provide means to rapidly place and remove components. Each time a part is removed and then replaced on the positioning stage, its location may vary over several microns. Calibration is therefore required each time a part is attached to the manipulator. We must also consider that these systems use delicate machine elements, which limits system load capacity (20 – 50 N). Higher load capacities are needed to accommodate forces from weight of parts and from manufacturing and assembly operations. The stiffness of these systems is also low, resulting in low resonance frequencies and load induced errors. Due to the above discussed limitations, these systems are generally limited for use in low rate, low force

applications.

Fixturing and positioning systems contain between them the requisite characteristics for future fixturing-alignment equipment. In this work, we investigate the means to combine the desired characteristics while eliminating those characteristics, which make either method unsuitable for the task. As this work addresses both fixturing and positioning requirements, the system developed herein is called a Hybrid Positioning Fixture (HPF).

1.3 Hypothesis and research goals

In spite of the limitations mentioned earlier, kinematic couplings form a good starting point to develop the next generation of ultra-precision fixtures. Kinematic couplings have been shown to be repeatable to better than 300 nm [10]. They can also be easily and rapidly engaged and disengaged. Additionally, their stiffness and load capacity may be set to satisfy most instrumentation and manufacturing requirements. They only lack the capability to become accurate and repeatable at the nanometer level. The hypothesis of this work is that nanometer-level accuracy and repeatability may be achieved by:

1. By incorporating high resolution, high stiffness actuators and hysteresis free compliant mechanisms within traditional kinematic couplings, active fixtures capable of six-axis corrective motion with nanometer-level accuracy may be developed.
2. One of the factors limiting repeatability of traditional kinematic couplings is the presence of friction at contact points. To achieve nanometer-level repeatability at reasonable costs, flexures may be incorporated to reduce frictional hysteresis at contact interfaces.
3. Additional performance improvement may be obtained through surface treatment of interfaces. This will promote the stability and longevity of the fixture contact geometry.

Toward this end, this work has the following research tasks/goals:

1. **Integration of actuators and mechanisms:** To achieve nanometer-level accuracy, active error correction in six axes is required. This necessitates the generation of a fixture design with integrated actuators, mechanisms and sensors. A kinematic theory is needed to relate actuator commands to fixture position and orientation. It should also be noted that incorporating actuators and mechanisms would modify the fixture's stiffness characteristics. Thus, a stiffness model for the fixture is to be developed that would enable design optimizations to simultaneously achieve the desired stiffness and kinematic characteristics.
2. **Integration of flexures at contact interface:** Stick-slip at contacts in fixtures limits their repeatability. A main goal of this work is to design contact interfaces with integral flexures that prevent stick-slip. Flexure concepts are to be generated. Parametric models will be derived for the flexures and used to tune their stiffness so that they may prevent stick-slip.
3. **Surface coatings:** One means of improving repeatability and reducing fixture contact wear is to use hard surface coatings [11]. The design of coated interfaces for precision fixtures requires the knowledge of stresses in the coating, interface and substrate. Though much work has been done to understand the behavior of these stresses [14,15], literature on stresses in thin coatings $\left\{\left(\frac{t_c}{a}<0.1\right)\text{tc} = \text{coating thickness, a} = \text{contact radius}\right\}$ is not available. This class of coatings $\left(\frac{t_c}{a}<0.1\right)$ corresponds to typical coating configurations in practical fixturing applications. Design rules for thin coatings will be developed utilizing non-linear finite element analysis.
4. **Experimental validation:** The utility of new design concepts, the accuracy of engineering models, and the utility of the new design rules will be tested via experiments on a prototype Hybrid Positioning Fixture (HPF).

1.4 Hybrid Positioning -Fixture (HPF) Overview

This work has culminated in a new positioning device, the HPF. The prototype consists of the two parts as shown in Figure 1.3. The first part, shown in Figure 1.3 (a), is comprised of high-resolution piezoelectric actuators, flexural "V" grooves and compliant transmission mechanisms. The second part, shown in Figure 1.3 (b), consists of three 1-inch diameter stainless-steel balls affixed to a plate. The test setup, shown in Figure 1.3 (c), was used to characterize repeatability, accuracy and stiffness of the HPF.

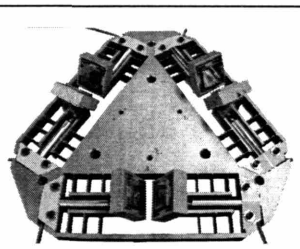

(a)Active component

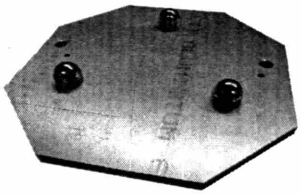

(b) Passive component

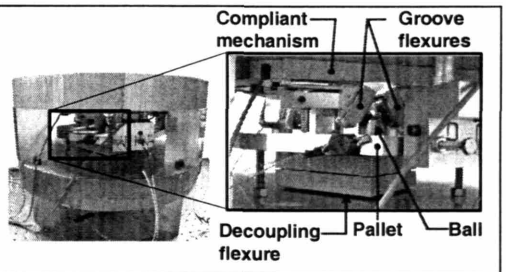

(c) Test setup

Figure 1.3: Ultra-precision fixture prototype – Hybrid Positioning Fixture (HPF)

Table 1.1 summarizes the key characteristics of the HPF. The HPF has the potential to form the basis for the design of fixtures for the next generation of instrumentation, ultra-precision and nano-manufacturing processes.

Table 1.1: Summary of key performance characteristics of the HPF

Axes	Range	Accuracy		Repeatability	Stiffness
		Open loop	Closed loop		(N/μm)
6	50μm & 625 μradians	100 nm & 2μradians	5nm	100 nm & 2μradians	7

An important application of the HPF is in palletized manufacturing. Figure 1.4 shows an example of a palletized system. Balled pallets are marked with passive identifiers (bar code or RFID tag) characterizing their systematic error sets (SES). A systematic error set

is a data set that contains all systematic errors for the balled pallet. Such errors would include manufacturing and assembly errors. The SES is obtained via calibration exercises. Each machining station is equipped with the active grooved component and the SES of the machine. When a fixture is engaged, the machining station reads the SES of the balled component and uses models to determine how the active elements should be commanded in order to achieve a desired fixture position and orientation.

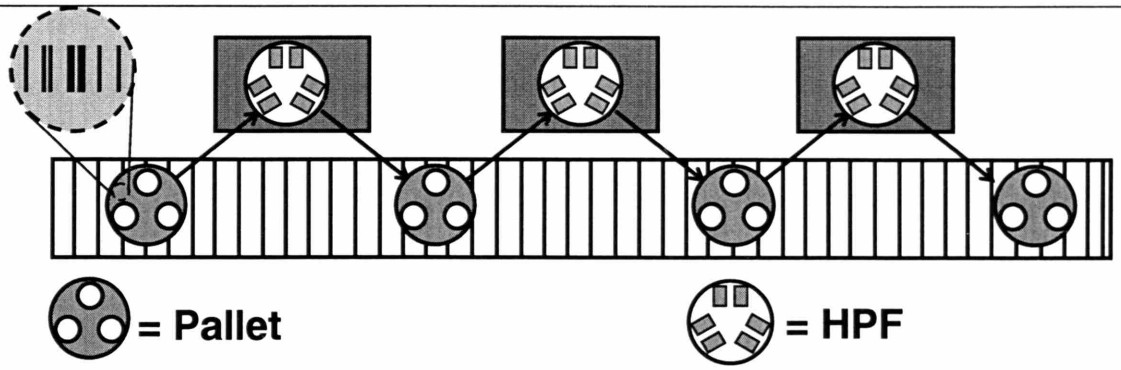

Figure 1.4: Integration of the HPF into a palletized machining process

1.5 Thesis overview

This thesis covers the modeling, design and characterization of the Hybrid Positioning Fixture. Chapter 2 presents the state-of-the art in detachable fixtures and other competing technologies. Chapter 3 covers the design of the HPF. Chapter 4 details the analytical models of the fixture's kinematics and stiffness. Chapter 5 presents the experimental performance characterization. Chapter 6 covers non-linear finite element analysis of thin coatings and design guidelines for the use of thin coatings in precision fixtures. Chapter 7 presents the conclusions, a summary of the fundamental contributions of the work and potential topics of future work.

Chapter 2 - State-of-the-art

This chapter presents the state-of-the-art in active fixtures and a comparison of these fixtures with nano-positioning systems.

2.1 Active precision fixtures

Much research on precision fixtures has been focused on passive fixtures, mainly kinematic couplings. These fixturing systems are limited to micron-level accuracy and repeatability, and are therefore not suited for next generation nano-manufacturing and ultra-precision applications. The Hybrid Positioning Fixture (HPF) with its nanometer-level accuracy and repeatability meets this need. It is important to understand the prior art in active precision fixtures before one can appreciate the advances embodied in the HPF. Toward this end, two active fixtures are presented in the subsequent sections. These systems are representative of the state-of-the-art prior to this work.

2.1.1 Precision X-Y micro-stage

Figure 2.1 shows a micro-positioning system developed by Taylor J.B. and Tu J.F [8]. The stage consists of a base plate with three "V" grooves placed 120° apart. The upper plate contains three spheres that mate with the "V" grooves in the base plate. One of the spheres is rigidly fixed while the remaining two may be maneuvered within their respective slots using linear actuators. The part to be positioned is connected to the upper plate at the point C shown in Figure 2.1 (b). The position of point C is of interest here and is controlled by motion of the actuators. The micro-positioning stage was shown to have a resolution of 1μm over a range of 40 x 40mm. The authors suggest the use of such systems in light load applications such as microelectronics particularly in a transfer line environment where the detachable and repeatable nature of the fixture is an automatic advantage.

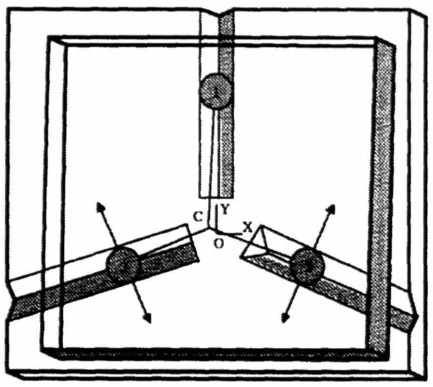

(a) X-Y micro-stage schematic

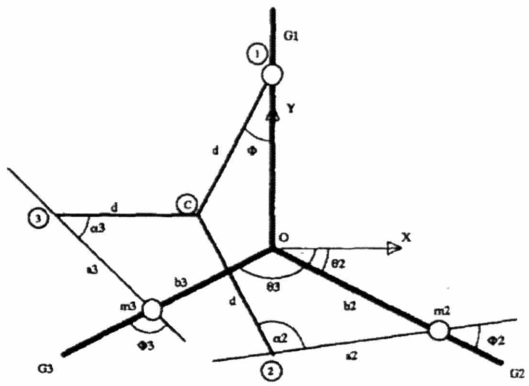

(b) Geometric model of X-Y stage

Figure 2.1: X-Y micro-stage with maneuverable kinematic coupling mechanism (figure by J.B Taylor and J.F Tu, Precision X-Y micro-stage with maneuverable kinematic coupling mechanism [8])

However, the system has the following limitations:

1. Its performance is not adequate for applications requiring nanometer-level accuracy. In these applications, positioning methods with resolution of about 0.1μm are utilized [8].
2. The in-plane motion of the stage is highly coupled and the system cannot position in any given position and orientation on the XY plane. The authors propose to address this problem through use of an additional linear actuator for the third sphere. Even with the modification, the system is limited to having three degrees of freedom. This implies that the system cannot compensate for out-of-plane errors.

2.1.2 Accurate and repeatable kinematic coupling (ARKC)

In 2003, the accurate and repeatable kinematic coupling was developed at the PCSL MIT [13,16]. The ARKC is shown in Figure 2.2. It combines the repeatability of traditional kinematic couplings with six-axis adjustment to attain micron-level accuracy and repeatability. This system addressed the limited degree of freedom of the XY micro-stage. The ARKC consists of two components; the active component consisting of three dual-

axis stepper motors and a passive component consisting of three "V" grooves. Each actuator shaft is connected to a ball such that the shaft axis is offset from the ball-center. Rotation of the shafts causes in-plane motion of the balled component whereas linear translation of the shafts causes out-of-plane motion. Thus, correction in six axes is possible. The ARKC has a measured 1σ repeatability of approximately 1.9μm/3.6μradian [13] and open loop accuracy on the order of approximately1μm/10μradian.

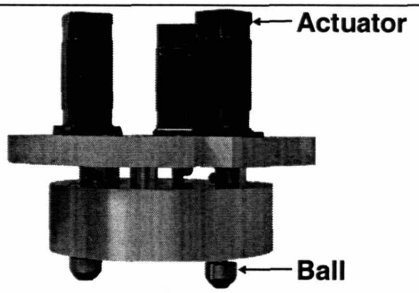

(a) Component with actuators and balls

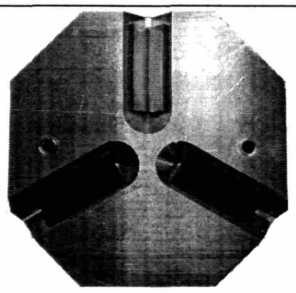

(b) Component with grooves

Figure 2.2: Accurate and Repeatable Kinematic Coupling (figure by M.L Culpepper, et al., Design of integrated mechanisms and exact constraint fixtures for micron-level repeatability and accuracy [13])

Though the ARKC has a range of applications in photonics and automotive industry, nanometer-level accuracy and repeatability were elusive due to hysteresis associated with use of rolling element bearings, stick-slip at contact interfaces and resolution of stepper motors. These limitations are addressed by the present work.

2.2 Competing technology - Nano-positioning stages

Nano-positioning stages are used in a wide range of applications including photonics packaging, semiconductor test equipment, precision mask and wafer alignment, scanning interferometry, biotechnology, micromanipulation and the like [17]. These positioning stages are capable of nanometer-level accuracy. These systems would be close competitors of active fixturing systems if they could provide easy means to place and remove parts on the stage, or in other words, provide mate-unmate capability.

Many state-of-the-art nano-positioning systems utilize piezoelectric driven flexure stages to achieve nanometer-level accuracy and resolution. Piezoelectric actuators in combination with closed loop control can provide sub-nanometer-level resolution and accuracy. Additionally, flexures may be used to achieve hysteresis free motion transmission. The HPF utilizes both flexures and piezoelectric acuators to achieve nanometer-level positioning [18].

Commercial nano-positioners include both serial and parallel kinematic stages. Figure 2.3 shows a schematic of serial and parallel kinematic, nano-positioning stages.. Serial kinematic stages have several limitations including higher inertia, high center of gravity, inability to correct for off-axis errors and moving cables that are the source of compliance and vibration errors. Thus parallel kinematic stages are best suited for nano-positioning applications [18].The HPF has a parallel kinematic architechture that avoids the limitations of serial stages.

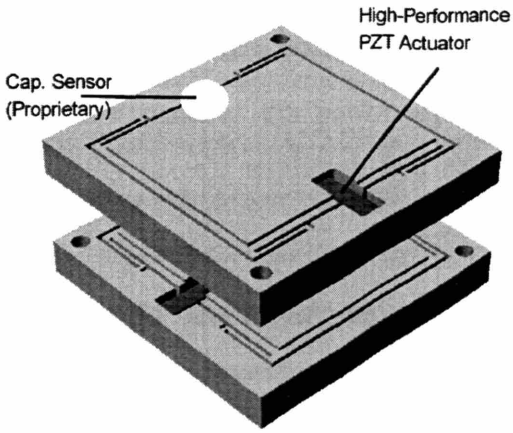

(a) stacked serial kinematic 2-DOF stage

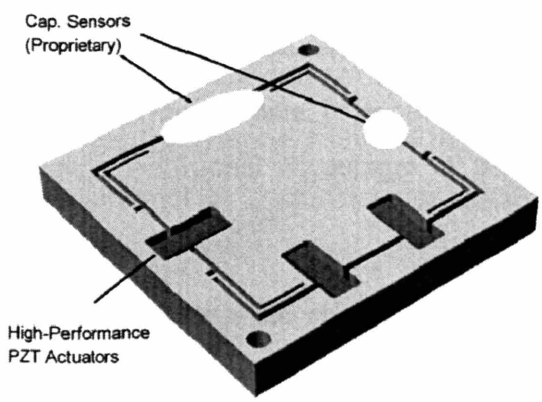

(a) Monolithic parallel 3-DOF stage

Figure 2.3: Serial vs. parallel kinematic nano-positioning stages (figure from TECHNOTE: State-of-the Art NanoPositioning System [18])

Table 2.1 compares the performance of the detachable fixtures including HPF and state-of-the-art nano-positioners from Physik Instrumente.

Table 2.1: State-of-the-art detachable fixtures and nano-positioning systems

	Axes	Resolution (μm/μrad)	Accuracy (μm/μrad)	Repetability 1σ (μm/μrad)	Stiffness (N/μm)	Load capacity [N]	Natural freq (Hz)
XY [8,16] stage	2	1/-	1/-	400/-	150	4000	unknown
ARKC [16]	6	1/10	1/10	2/4	150	4000	unknown
HPF	6	0.003/-	0.1/2***	0.1/2	10	450	202**
P-762 [19]	5	0.01/0.5	unknown	N/A	unknown	20	200**
P-587 [17]	6	0.008/0.1*	unknown	N/A	unknown	50	103**

*Closed loop operation

**In-plane XY

***Open loop operation followed by 2-3 adjustment steps (see Section 5.3.2)

The HPF matches the performance of the best nano-positioners in terms of motion capability (axes), resolution and natural frequency. Additional advantages of the HPF include:

1. The HPF has about 10 times larger load capacity than the state-of-the-art nano-positioning systems.
2. The HPF is amenable to use in large scale applications as part of the assembly or transfer line. This is due to the ease with which the fixture may engage-disenage and yet retain nanometer-level repeatability.
3. The "drop and forget" capability makes integration into automated production/testing lines easy. The part to be positioned may be attached to the passive balled component (pallet) and the active grooved component may be fixed to the machining or testing center. A robotic arm may pick up the part (attached to the pallet) and place it roughly over the grooved component. The balled component automatically aligns to the

correct position on the grooved component. This is termed as "drop and forget," meaning that the balled component is droped on to the grooved component without assessing the subseqent alignment accuracy. The kinematics of the HPF ensures that it attains the correct position. This is shown schematically in Figure 2.4.

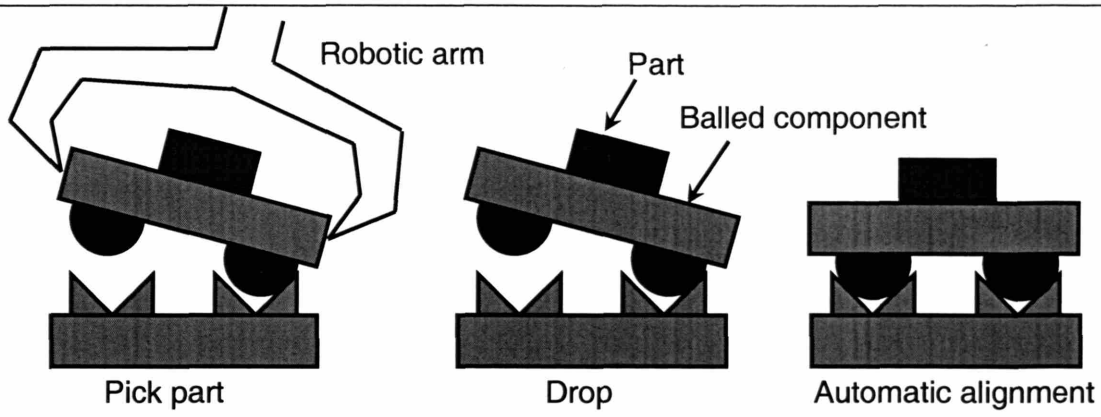

Figure 2.4: "Drop and forget" capability of kinematic fixtures like HPF

Chapter 3 - Design of the HPF

This chapter focuses on the concepts and system-level design choices, which were made in designing the prototype Hybrid Positioning Fixture. The goal of this chapter is to provide a discussion that outlines the thought process, which drove the decisions made in setting up the architecture of the HPF. When appropriate, quantitative data is provided, although sound engineering knowledge/experience is also used to decide on the best embodiment of a sub-system or system design. Subsequent chapters will provide assessment and application of quantitative analyses.

The chapter is organized into three sections. The first section discusses the fundamental issues associated with designing precision fixtures for nanometer-level accuracy. The second section discusses the conceptual design, while the third section details the design of the individual components. Detailed component drawings are available in Appendix A.

3.1 Fundamental issues

3.1.1 Exact constraint design

The fundamental principle of designing precision fixturing systems is the provision of exact constraint. In order to determinstically locate a rigid body in three dimensional space, six constraints are required. If the fixturing system provides exactly six constraints, the location of component is uniquely determined. This makes the fixture performance predictable and enables closed-form modeling, thereby reducing engineering costs associated with design iterations [20]. Provision of extra constraint or "over constraint" of the system will often lead to parts binding together or parts being too loose. As a result, the relative position of these parts is not well defined. Figure 3.1 shows schematically the constrast between exact constraint and over constraint.

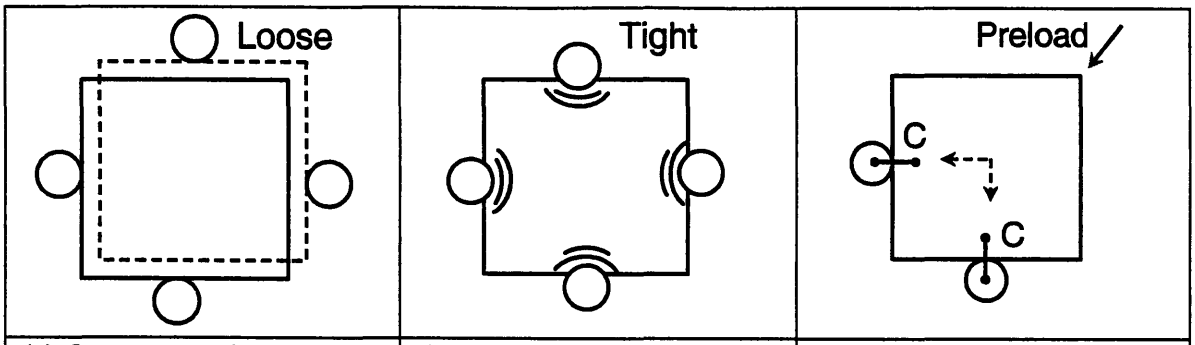

(a) Over constraint - Loose	(b) Over constraint - Tight	(c) Exact constraint

Figure 3.1: Over constraint vs. exact constraint (figure by D.L. Blanding, Exact Constraint: Machine Design Using Kinematic Principles [21])

"Elastic-averaging" based alignment methods, use the averaging effect of competition between "extra" constraints to obtain high stiffness, load capacity and moderate repeatability. These methods are not well-suited (repeatability limited to approximately 5μm) for emerging precision alignment needs due to problems associated with over constraint.

3.1.2 Repeatability vs. Accuracy

The two primary issues in the design of precision fixtures are "repeatability" and "accuracy".

"Precision (of position), also called repeatability, is the degree to which a part or a feature on a part, will return to exactly the same position time after time." [21]

"Accuracy (of position) is the degree to which location of a part or feature exactly coincides with its desired or intended location." [21]

These concepts are illustrated schematically in Figure 3.2, wherein a ball is constrained within a "V" shaped groove. Figure 3.2 shows how exact constraints may be employed to insure that the ball returns to the same position (with a small spread) even after repeated engagement-disengagement sequences. This indicates that the system is "repeatable" and its repeatability is given by the variation in relative location (r). Figure 3.2 also shows

that, even with a small spread, the system could still be far from the desired location. In other words, it is not "accurate" and its accuracy (a) is given by difference in actual and desired positions. Typically, repeatability may be achieved independent of accuracy, as is done in kinematic couplings. Accuracy on the other hand, depends on factors such as manufacturing and assembly tolerances, and time variable error sources such as external loads and thermal effects.

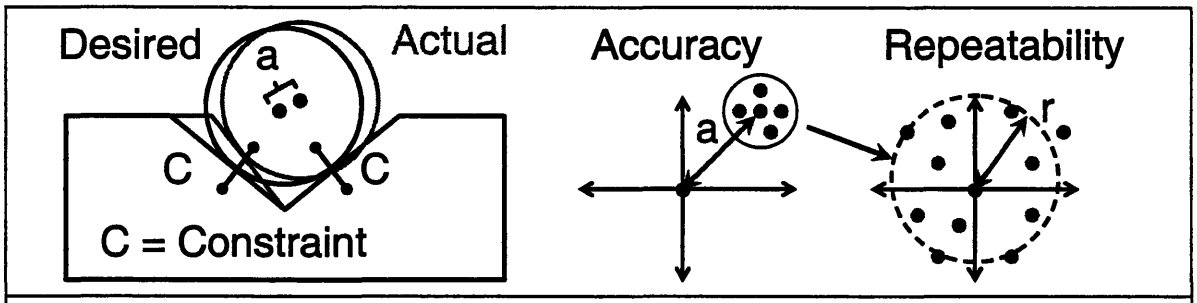

Figure 3.2: Repeatability and accuracy

3.1.3 Friction and wear

The repeatability of kinematic couplings is limited by friction and wear of contact interfaces. The effect of friction on repeatability may be estimated using Equation 3.1 [22].

$$\frac{f}{k} \approx \mu \left(\frac{2}{3R}\right)^{1/3} \left(\frac{P}{E}\right)^{2/3} \tag{3.1}$$

Where:

R = equivalent radius of curvature

E = equivalent Young's modulus

P = external load

μ = coefficient of friction.

The frictional force acts on the compliance of the contact interface to pull the fixture off position. The estimate is obtained as a product of frictional force ($f = \mu P$) and compliance ($1/k$) of a single Hertzian contact under load P.

The magnitude of non-repeatable errors associated with friction-induced stick slip and wear may be reduced by:

1. Increasing contact stiffness or modulus (E)
2. Decreasing coefficient of friction (μ)
3. Minimizing contact damage and wear
4. Minimizing relative motion between ball and groove

With the use of specialized ceramic materials for the ball-groove interface, positioning repeatability of about 300nm has been achieved [10]. The high stiffness, wear resistance and low friction coefficient of the ceramic materials endows them with excellent performance capability. However, custom coupling components made from ceramic materials are difficult and expensive to manufacture. With these considerations, hard-coated ball-groove surfaces are to be explored as a cost-effective alternative to high-cost ceramic components [11]. Frictional hysteresis, a component of non-repeatability, is theoretically zero if there is no relative motion at the contact interfaces. By increasing compliance in direction parallel to that of the relative motion, hysteresis may be reduced [12].

3.1.4 Active vs. passive fixtures

Though repeatable, the accuracy of passive fixtures is strongly coupled to manufacturing and assembly tolerances. To overcome these limitations, actuators and mechanisms must be integrated within the fixture so that they may be utilized to provide active correction capability. Figure 3.3(a) shows the limitation imposed on the accuracy of a passive fixture due to manufacturing errors. Figure 3.3(b) shows the improved accuracy which may be obtained by incorporating an active element (actuator = A) within the fixture. The

mated position in (a) is "actuated" to obtain the more accurate position shown in (b).

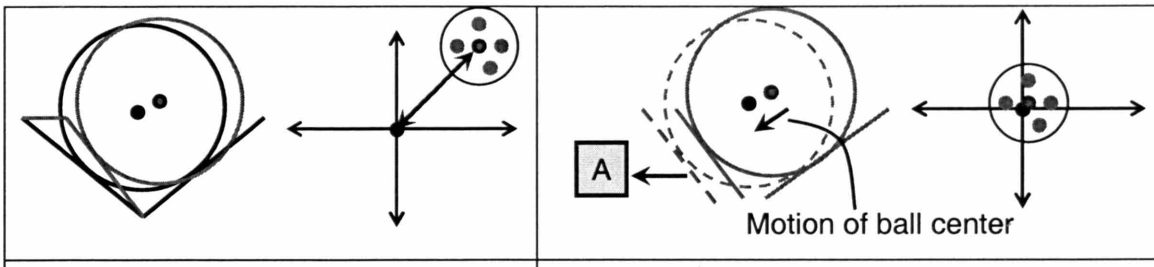

(a) Passive fixture | (b) Active fixture

Figure 3.3: Active vs. passive fixture

3.2 Conceptual design

3.2.1 Design for nanometer-level accuracy

To actively compensate for errors, actuators and mechanisms, which are integrated into the fixture should be able to work together to provide error correction in six-axes. We can gain insight into how this is best accomplished by examining the mechanism nature of kinematic couplings. A kinematic coupling's six-constraints are analogous to the constraints in a Stewart platform. This is shown schematically in Figure 3.4. Stewart platforms generate motion by changing the constraints on the platform, therefore it should be possible to adjust a kinematic coupling's position and/or orientation by adjusting the location of the constraining elements (balls and/or grooves) [13].

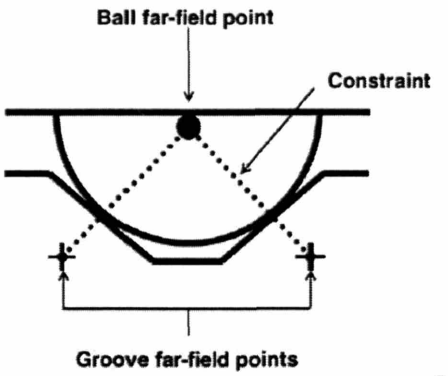

(a) Two constraints at a ball-groove interface

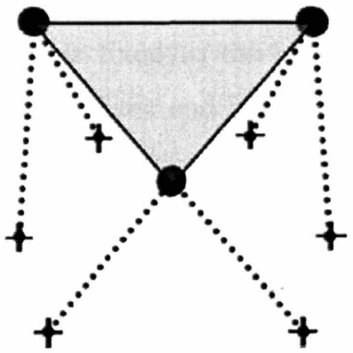

(b) Six constraints in a kinematic fixture

Figure 3.4: Analogy between a kinematic fixture and a Stewart platform (figure by M.L Culpepper, et al., Design of integrated mechanisms and exact constraint fixtures for micron-level repeatability and accuracy [13])

Two concepts, which have been used to achieve six-axis adjustment were presented in [13] and are shown in Figure 3.5.

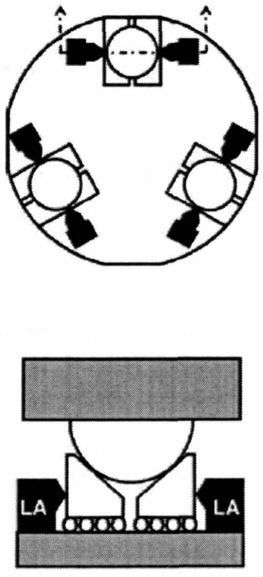

(a) Linear groove motion concept

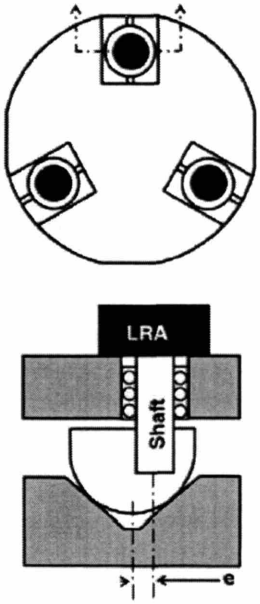

(b) Eccentric ball-shaft concept

Figure 3.5: Concepts for achieving six-axes correction (figure by M.L Culpepper, et al., Design of integrated mechanisms and exact constraint fixtures for micron-level repeatability and accuracy [13])

In concept (a), the component to be positioned is mounted on the balled part of the fixture while the grooved part, containing the active elements, is fixed to the ground. This concept utilizes six linear actuators to move the groove surfaces and hence the balled component. Concept (b), on which the ARKC is based, consists of three balls mounted on eccentric shafts connected to dual-axis stepper motors. Rotation of the shafts causes in-plane motion of the balled component whereas linear translation of the shafts causes out-of-plane motion. Rolling element bearings are utilized to permit rotation and translation of the ball-shaft sub-assemblies. In this design, the part to be positioned is connected to the grooved component while the balled component is fixed to the ground.

Concept (a) was chosen for the HPF since it is amenable to implementation with piezoelectric actuators and flexural bearings. The hysteresis free nature of flexure bearings and sub-nanometer resolution of the piezoelectric actuators may be used to avoid the limitations imposed by the rolling element bearings (friction) used in the alternate design. Thus, nanometer-level accuracy may be achieved. The kinematics of the HPF is discussed in more detail in Section 4.1.

3.2.2 Design for nanometer-level repeatability

In a traditional "V" groove, as the ball mates with the "V" groove the interface is compressed elastically. This compression is accompanied by a tangential motion of the contact point, in conformance to the constraints. The tangential motion leads to macro slip at the contact interface and lends uncertainty to the position of the contact point and hence the ball center. This uncertainty is termed as hysteresis. Figure 3.6 depicts this process schematically.

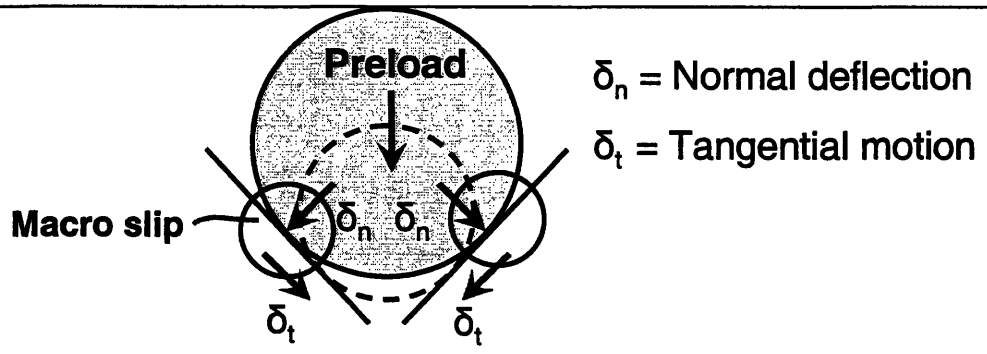

Figure 3.6: Macro slip at the interface between a ball and a "V" groove

Figure 3.7 presents results from [12], which shows the hysteresis associated with loading and unloading of a kinematic coupling. This hysteresis is the difference between compression of the contact as the preload increases and as the preload decreases. Figure 3.7 (a) shows that for a coupling with flexure grooves the hysteresis is reduced by a factor of 10, compared to traditional grooves. Figure 3.7(b) shows flexure hinges cut into groove surfaces; the flexure has relatively high compliance, C_t, tangential to the surface and low compliance, C_n, normal to the surface. The low tangential compliance permits the ball to adjust in the groove without causing relative motion between the ball and groove surfaces. The preload on the coupling is cycled without disengaging the balled and grooved components. Hence, the effect on repeatability over several cycles of engagement and disengagement of the coupling components is uncertain. As a result, the potential for this design concept to eliminate the effects of stick slip (this is not hysteresis) and hysteresis, which result from the engaging-disengaging of the contacts, is uncertain. As both sources of error must be addressed to obtain nanometer-level accuracy, the subsequent sections will focus on the design of flexures that address these errors.

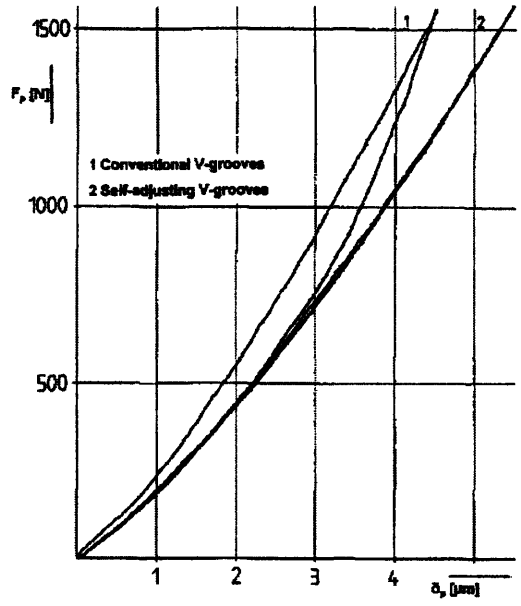

(a) Measurements of preload force F_p and elastic deflection δ_p

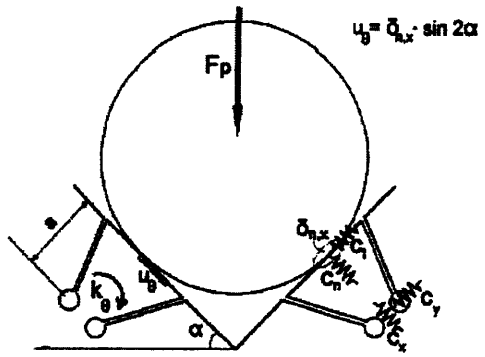

(b) Ball in V-groove with elastic hinges

Figure 3.7: Measurements of preload force F_p and elastic deflection δ_p (figure by C.H. Schouten, et al., Design of a kinematic coupling for precision applications [12])

In designing the flexure, high stiffness in direction normal to interface is desirable, with regard to both repeatability and overall stiffness of the fixture. On the other hand, high compliance in the tangential direction is required to minimize relative motion. However, reduction in tangential stiffness also reduces overall stiffness of the fixture. In a conventional ball-groove contact the ratio of tangential to normal contact stiffness is approximately 0.83. This implies that the tangential stiffness is nearly equal to the normal stiffness. To achieve a balance between fixture stiffness and reduction of sliding motion between the contacts, the design requirement for the groove flexure was chosen to be

$$K_t \leq 10 \cdot K_n$$

Where:

K_t = Tangential stiffness

K_n = Normal stiffness

3.3 Component design

The HPF consists of two major components: the grooved component and the balled component. The grooved component, incorporates the actuators, bearings, and groove flexures. This part is analogous to the component containing "V" grooves in a traditional, three-groove kinematic coupling. The balled component contains three balls that are press fitted into a plate. This component is identical to the balled component of a three-groove kinematic coupling. Sections 3.3.1 to 3.3.5 describe elements of the grooved component and while Section 3.3.6 describes the balled component.

3.3.1 Actuators

Several actuators were considered for the design, including electromagnetic, lead-screw-stepper motor combinations, however piezoelectric actuators were the only type capable of delivering tens of microns stiffness and nanometer-level resolution. PA50-14 SG (stack type) piezoelectric actuators supplied by piezosystem jena Inc., are used in the prototype. The key characteristics of the piezoelectric actuators used in the design and testing of the HPF are listed below [23]:

- Input voltage (-)15 to (+)100 V
- Range - 50μm
- Resolution - 0.07nm
- Stiffness - 20 N/μm
- Load capacity - 1000 N
- Integrated strain gauge for displacement measurement
- Maximum tensile loads approximately150N

3.3.2 Flexure bearings

In the present application, traditional linear bearings cannot be utilized to transmit motion of the actuator to the groove surfaces due to stick slip between the bearings and their races. This limitation does not exist for flexure bearings, which utilize elastic deformation

to achieve motion. When the flexure bearing is placed in series with the actuator, the stiffness of bearings in the direction of actuator motion should be small, e.g. less than 0.1 of the actuators stiffness. This ensures that the actuator range is not reduced by more than 10%. It is also important for the flexure bearing to possess high stiffness in other directions. This helps to reduce parasitic errors and errors due to loads that act in directions other than the actuation direction, e.g. preload error loads or other external disturbance forces. The six-beam flexure design (SBF), shown in Figure 3.8, was chosen to guide the motion of the piezoelectric actuator. Although the design could have used four, eight or more flexure beams, it was found that six beams would provide the requisite compliance in the actuation direction and high stiffness in other directions. The motion of the bearing is small enough, (about 50 μm) that stiffening effects in the beams may be neglected. Detailed stiffness characteristics of the groove flexure are presented in Section 4.2.4.

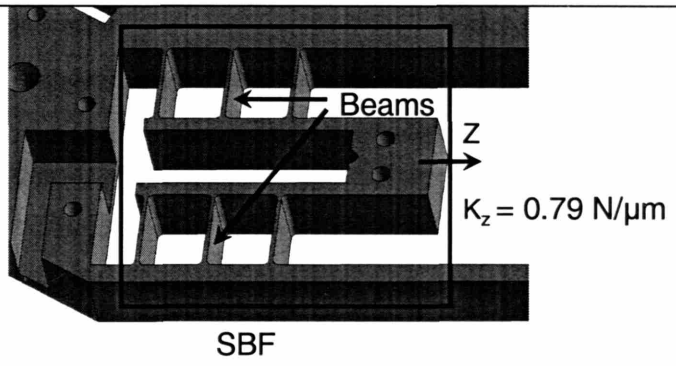

Figure 3.8: Six beam flexure

3.3.3 Actuator mounting

The stack type piezoelectric actuators used in the HPF are primarily "push" type and the mounting must be designed to eliminate any tensile or torsion loads. The mounting method consists of a ball mounted to the tip of the actuator, which engages a "V"-groove on the SBF. This provides constraint in two directions while eliminating torsion loads on the actuator tip. Additional constraints are provided by the actuator clamps and the flat face supporting the back of the actuator. Figure 3.9 shows the grooved component with

the actuators and six beam flexures.

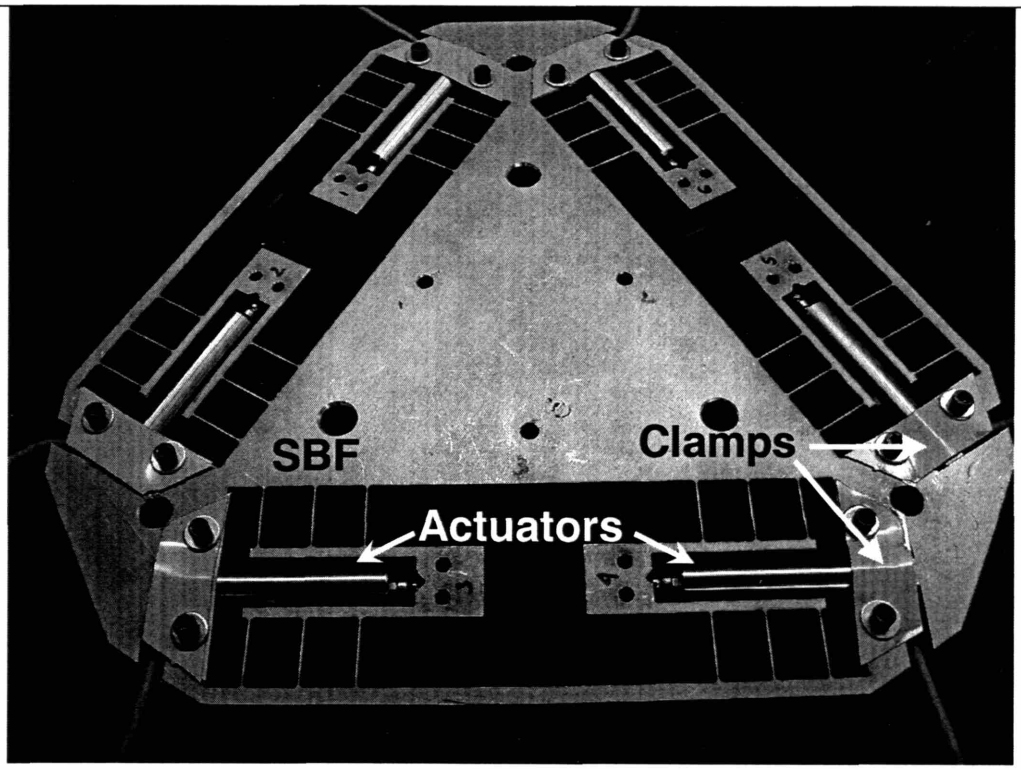

Figure 3.9: Grooved component with actuators mounted

1.1.1 Groove flexure

Different concepts were considered for the groove flexures and are shown in Figure 3.1.

Concepts	(a)	(b)	(c)
	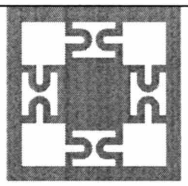		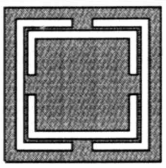
Achieving tangential compliance	-1	-3	0
Modeling complexity	-1	2	0
Error / parasitic motion	0	-3	0
Total	-2	-4	0
Figure 3.1: Groove flexure concepts			

The concepts were compared based on:

1. **Ease of achieving desired tangential stiffness for a given flexure size:** Concept (a) is assigned a negative value due to the difficulty in packaging the flexural spring elements to achieve the desired tangential compliance. Concept (b) is assigned a higher negative value due to the relative manufacturing complexity and the large flexure height or thin neck size that is required.
2. **Modeling:** As we wish to develop an analytic stiffness model for the fixture, the flexure concept should be amenable to parametric modeling. Concept (a) is assigned a negative value due to relative complexity of modeling the spring elements. For concept (b), analytical models are readily available in literature. Concept (c) is composed of simple beam elements and is therefore easier to model and manufacture than concept (a).
3. **Parasitic errors:** The flexure-associated motions of the groove flexure in directions normal and tangential to the groove's contact surface should be decoupled to enable independent stiffness tuning. This is expressed as error or parasitic motion, which implies motion in a direction(s) leading to undesired motion in another. With respect

to this parameter, concept (b) has relatively large susceptibility for parasitic motion. Rotation about the center of the necked portion leads to undesired motion normal to the flexure surface.

Based on the concept comparison shown in Figure 3.10, concept (c) was chosen as the best concept. The final design of the groove flexure is shown in Figure 3.11. The groove flexures were manufactured using 6061 Aluminum, with a 316 stainless steel plate bonded to the surface that forms the contact surface. These groove plates may easily be replaced with other materials if required.

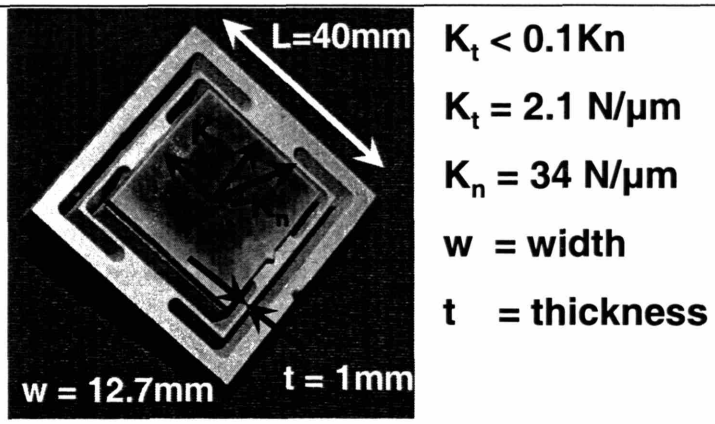

Figure 3.11: Groove flexure – final design

3.3.5 Groove flexure mounting

With regard to mounting the groove flexure on the six-beam flexure, the challenge is to minimize vertical deflection of the flexure resulting from the applied preload. Figure 3.12 shows a CoMeT simulation [24] of the flexure's deflection under a vertical load.

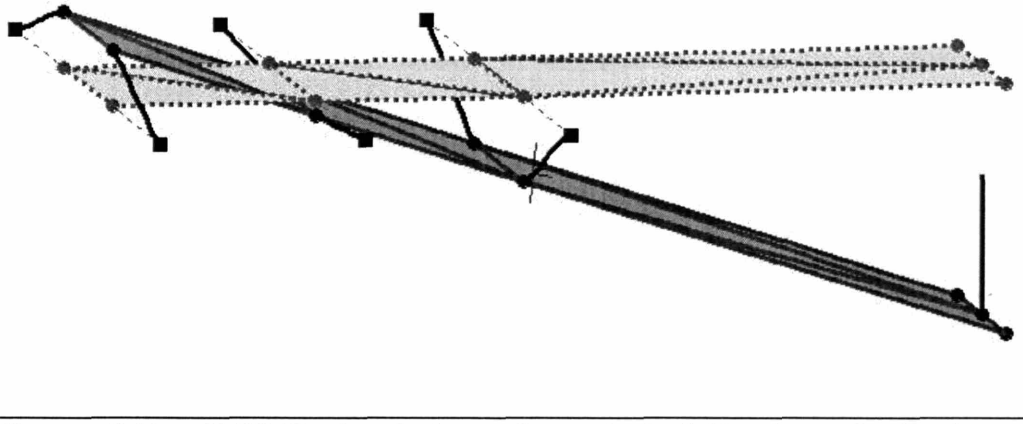

Figure 3.12: CoMeT simulation of vertical deflection of six beam flexure (displacement shown is exaggerated for clarity)

The normal force on the groove surface may be decomposed into components F_z and F_y as shown in Figure 3.13. These force components result in moment M_x about the X- axis of the SBF and is given by Equation 3.2.

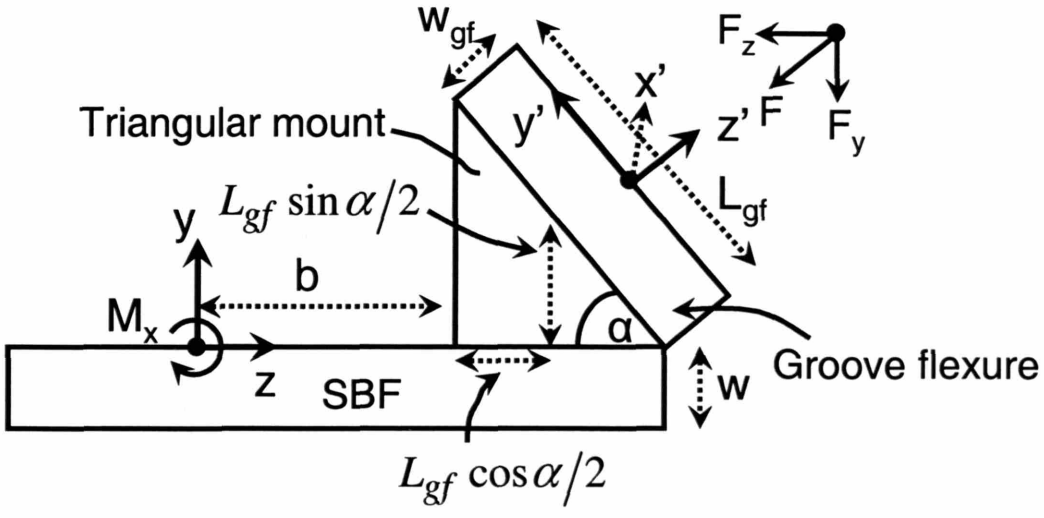

Figure 3.13: Groove flexure mounting

$$M_x = Fx * \left(w_{gf} \cos\alpha + \frac{L_{gf} \sin\alpha}{2} + \frac{w}{2} \right) - Fy * \left(b + \frac{L_{gf} \cos\alpha}{2} + w_{gf} \sin\alpha \right)$$

$$F_x = F \sin\alpha \ , \ F_y = F \cos\alpha \qquad \textbf{(3.2)}$$

By appropriately selecting the dimension b, the moment M_x may be balanced to minimize the twist and thereby the deflection of the flexure. Equation 3.3 gives the required dimension b.

For $M_x = 0$, from Equation 3.2

$$b = \frac{\left(w_{gf}\cos\alpha + \frac{L_{gf}\sin\alpha}{2} + \frac{w}{2}\right)\sin\alpha}{\cos\alpha} - \left(\frac{L_{gf}\cos\alpha}{2} + w_{gf}\sin\alpha\right) \qquad \textbf{(3.3)}$$

$$\Rightarrow b = \frac{L_{gf}(\sin^2\alpha - \cos^2\alpha)}{2\cos\alpha} + \frac{w\tan\alpha}{2}$$

For a groove angle (α) of 60° $b = \frac{L_{gf}}{2} + \frac{w\sqrt{3}}{2}$ results in $M_x = 0$, thereby minimizing the vertical deflection of the flexure. Figure 3.14 shows the complete grooved component with all the sub-elements, namely the actuators, flexure bearings (SBF) and the groove flexures.

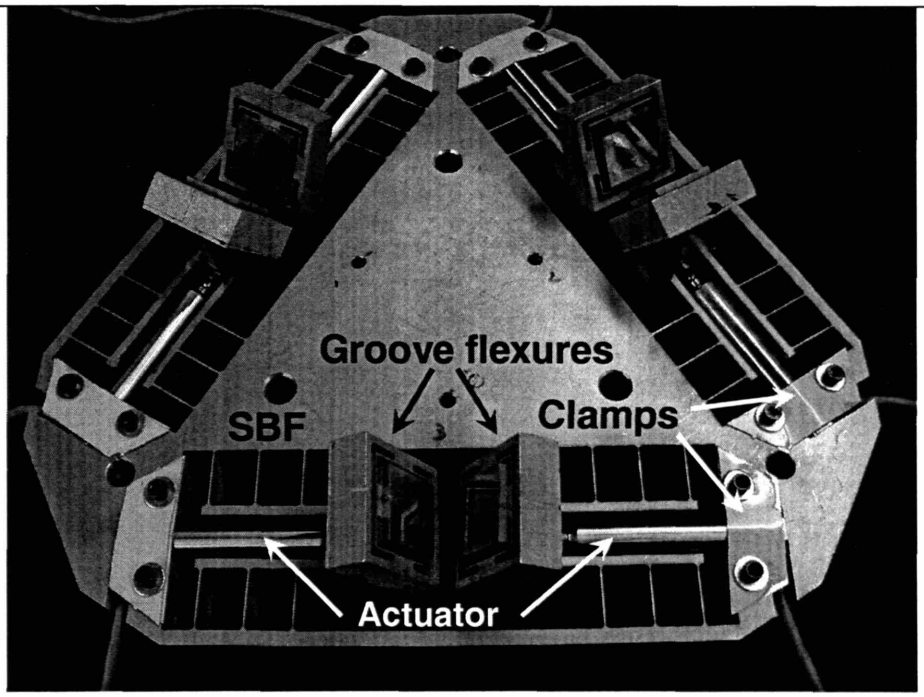

Figure 3.14: Grooved component with flexure grooves

3.3.6 Capacitance probe mount

To monitor the position of the fixture's balled component in six axes, a minimum of six probes are needed. Three of these probes are mounted on the test setup and are used to measure the in-plane motion. For further details, see Section 5.2. Three other probes, which are mounted on the grooved component, measure the out-of-plane motion of the balled component. Figure 3.15 shows the probe mount, which is attached to the grooved component and used to hold the out-of-plane sensors.

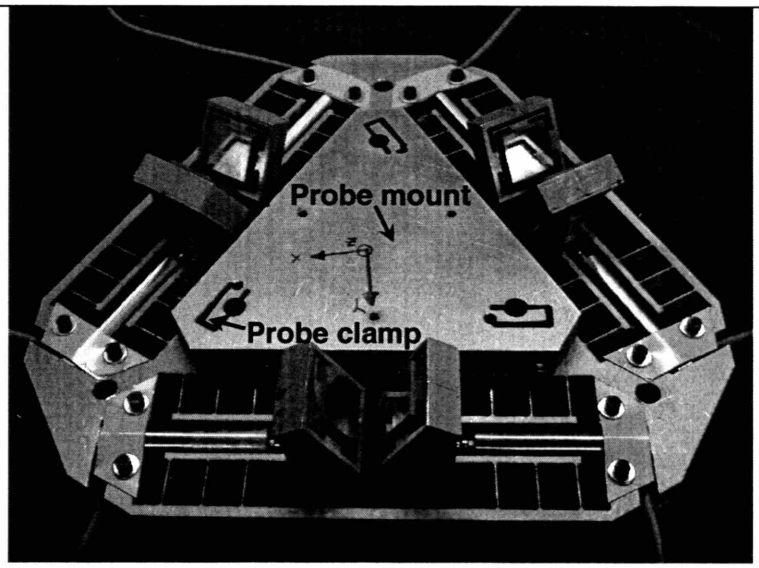

Figure 3.15: Grooved component with probe mount

3.3.7 Balled component

The balled component consists of three 316 stainless steel balls, pressed into sleeves that are in turn pressed into an aluminum plate. The sleeves are utilized instead of directly pressing the balls into the plate, to avoid interference with the groove flexures. The sleeves themselves consist of a smaller sleeve fitted into a bigger sleeve. The height of the smaller sleeve is designed such that a little more than half of the ball is within the sleeve. Figure 3.16 shows the balled component and a cross sectional view of the sleeves.

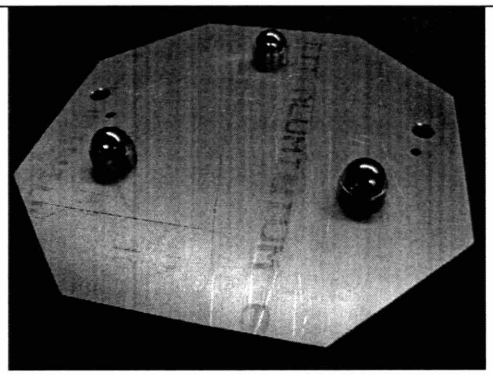

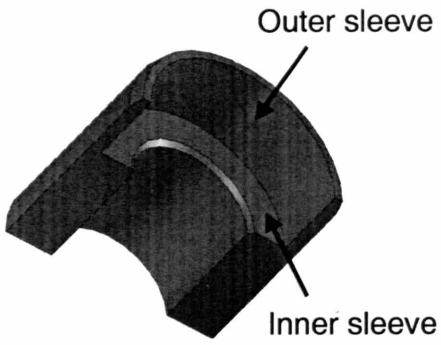

(a) Balled component | (b) cross sectional view of sleeve

Figure 3.16: Balled component

Figure 3.17 shows an exploded view of the Hybrid Positioning Fixture.

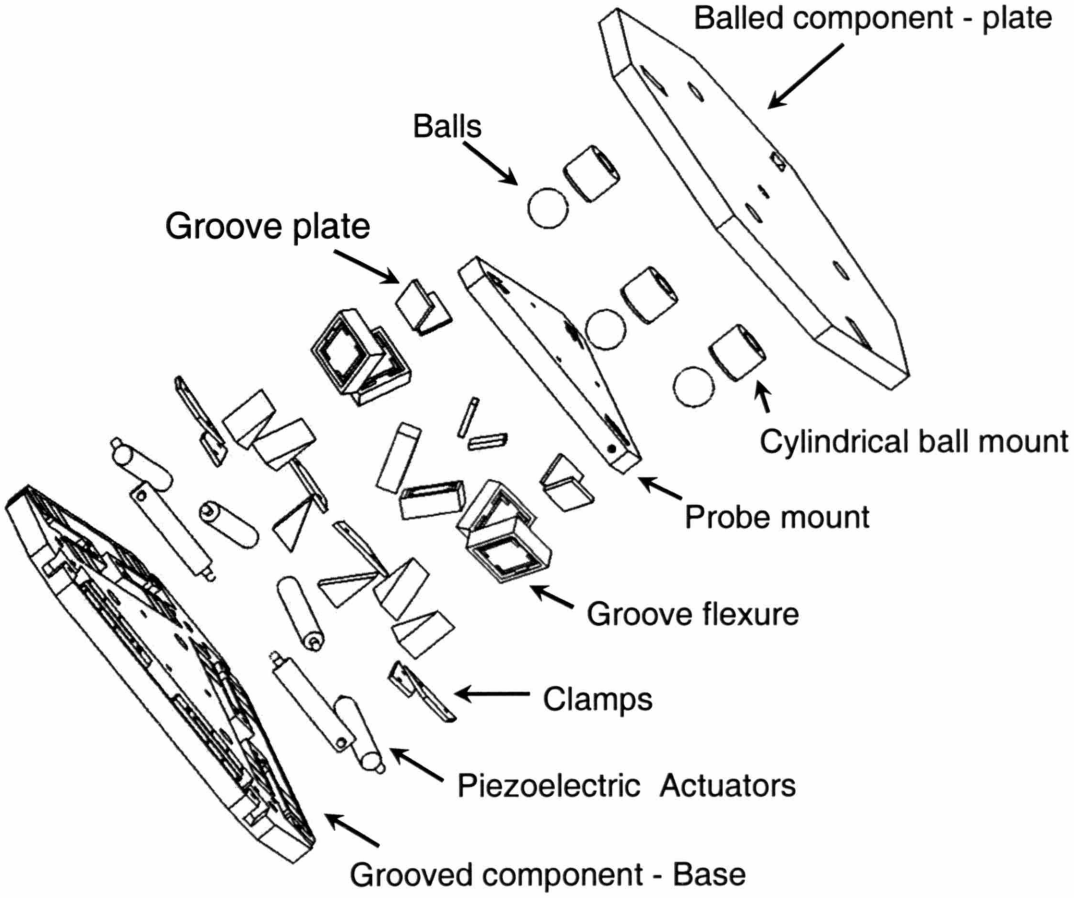

Figure 3.17: Exploded view of Hybrid Positioning Fixture

Chapter 4 - Analytic modeling

The chapter is organized into two segments. The first segment covers the kinematic modeling of the HPF and the second segment describes stiffness modeling. The former, deals with modeling the forward and inverse kinematics that define the relationship between motion of the actuators and that of the HPF. The later, gives a relationship between the external forces applied to the fixture and the resulting deflections, which must be added to the kinematic analysis to capture the true position of the HPF.

4.1 Kinematic modeling

4.1.1 Overview

To achieve improved accuracy, active correction in six axes is required. This requires a deterministic kinematic model of the system that relates input from the active element (actuator) to the motion of the fixture. Common terminologies used in this regard are "forward kinematics" that determines the motion of the system resulting from a given set of actuator inputs and "inverse kinematics" that determines the actuator inputs required for a desired motion of the fixture.

The part to be positioned is connected to the balled-component. Therefore, in developing the kinematics of the fixture, we are interested in studying the motion of the balled-component's coupling centroid. The position of the balled-component is defined by position of the three ball centers. The basic principle, behind the adjustable kinematics of the HPF is that the motion of the groove surfaces leads to motion of the corresponding ball centers. This is demonstrated schematically in Figure 4.1. Equations 4.1-4.2 describe this relationship mathematically. Here the inward motion (towards the ball center) of the grooves is considered positive since it corresponds to the positive displacement of the actuators.

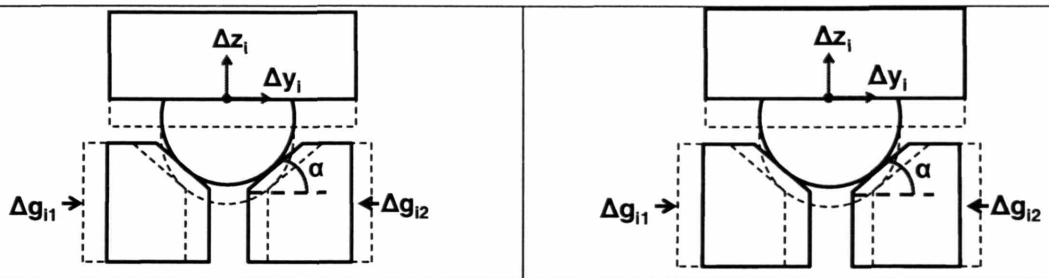

(a) In-plane motion of ball center | (b) Out-of-plane motion of ball center

Figure 4.1: Relationship between groove and ball center motion

$$\Delta y_i = \frac{\Delta g_{i1} - \Delta g_{i2}}{2} \tag{4.1}$$

$$\Delta z_i = \left(\frac{\Delta g_{i1} + \Delta g_{i2}}{2} \right) . \tan \alpha \tag{4.2}$$

The six-axis motion of the HPF is achieved by a combination of motions of the groove surfaces. Examples of the HPF's motion are provided in Figure 4.2.

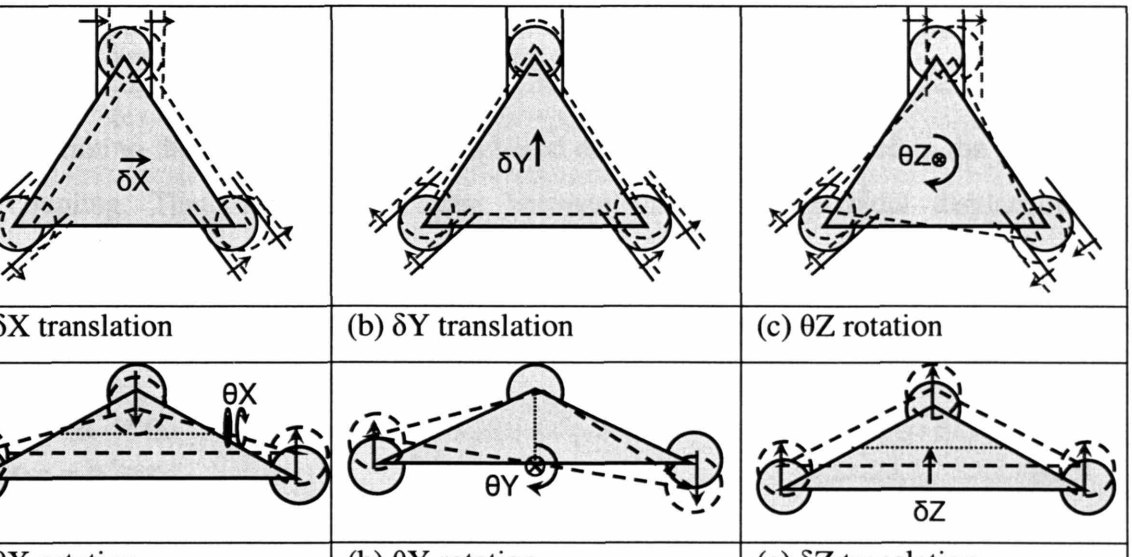

(a) δX translation | (b) δY translation | (c) θZ rotation

(a) θX rotation | (b) θY rotation | (c) δZ translation

Figure 4.2: HPF six-axis motion

4.1.2 In-plane motion

Figure 4.3 depicts two configurations of the coupling. One, wherein the balled component coincides and the other where it is displaced with respect to the coordinate system CS_0 attached to the grooved component.

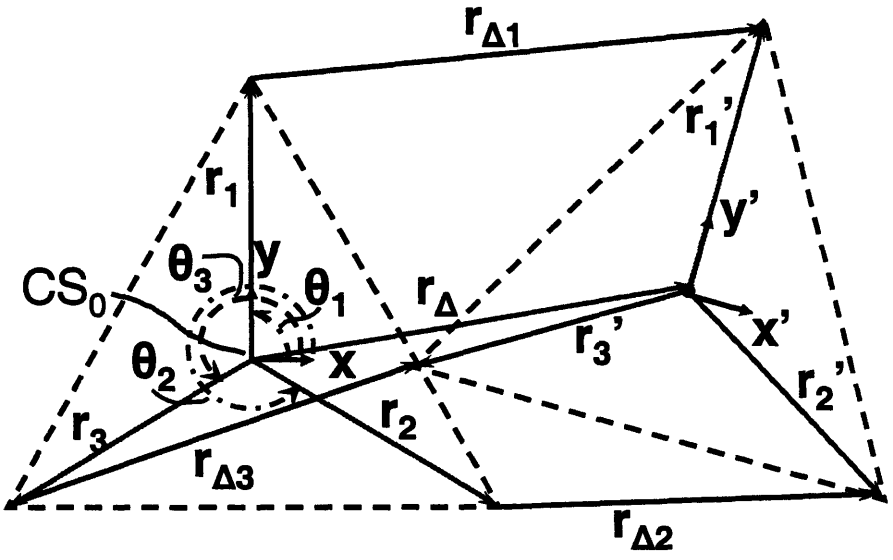

Figure 4.3: Vector based model for in-plane motion

The solution to the in-plane kinematics is based on vector loops projected in the plane of the coupling. The vector loops share between them the centroidal displacement $r_\Delta = X_c.i + Y_c.j$. Three vector loops may be written corresponding to each ball-groove mate, to obtain Equation 4.3.

$$\begin{aligned} r_1 + r_{\Delta 1} - r_1' &= r_\Delta \\ r_2 + r_{\Delta 2} - r_2' &= r_\Delta \\ r_3 + r_{\Delta 3} - r_3' &= r_\Delta \end{aligned} \tag{4.3}$$

Where:

$$r_q = x_q \cdot \hat{i} + y_q \cdot \hat{j} + z_q \cdot \hat{k} \tag{4.4}$$

This method of vector loops is similar to that utilized in [13]. These equations may then be expanded to obtain relationship between displacement of the ball centers and balled-component's centroid. In developing these equations, small angle approximations have been made (assuming $\theta z_c < 1000$ μradians) - $\sin(\theta z_c) \approx \theta z_c$ and $\cos(\theta z_c) \approx 1$.

$$\begin{bmatrix} x_1+\Delta x_1 & x_2+\Delta x_2 & x_3+\Delta x_3 \\ y_1+\Delta y_1 & y_2+\Delta y_2 & y_3+\Delta y_3 \\ z_1+\Delta z_1 & z_2+\Delta z_2 & z_3+\Delta z_3 \\ 1 & 1 & 1 \end{bmatrix} = \begin{bmatrix} 1 & -\theta_{zc} & 0 & X_c \\ \theta_{zc} & 1 & 0 & Y_c \\ 0 & 0 & 1 & 0 \\ 0 & 0 & 0 & 1 \end{bmatrix} \begin{bmatrix} L_1.c[\theta_1] & L_2.c[\theta_2] & L_3.c[\theta_3] \\ L_1.s[\theta_1] & L_2.s[\theta_2] & L_3.s[\theta_3] \\ 0 & 0 & 0 \\ 1 & 1 & 1 \end{bmatrix} \quad \textbf{(4.5)}$$

$$X_c = \Delta x_1 + \left(\frac{L_1.s[\theta_1].(\Delta y_2 - \Delta y1)}{L_2.c[\theta_2] - L_1.c[\theta_1]} \right) \quad \textbf{(4.6}$$

$$Y_c = \Delta y_2 - \left(\frac{L_2.c[\theta_2].(\Delta y_2 - \Delta y1)}{L_2.c[\theta_2] - L_1.c[\theta_1]} \right) \quad \textbf{(4.7)}$$

$$\theta_{zc} = \frac{\Delta y_2 - \Delta y_1}{L_2.c[\theta_2] - L_1.c[\theta_1]} \quad \textbf{(4.8)}$$

Where $r_i = x\hat{i} + y\hat{j}$, $r'_i = (x+\Delta x)\hat{i} + (y+\Delta y)\hat{j}$, θz_c is rotation about Z-axis and $L_i = |r_i|$.

Figure 4.4 shows the coordinate systems attached to the grooved component. The global coordinate system CS_0 is attached to centroid of the component and three local coordinate systems CS_i's are placed at the vertices corresponding to the ball-groove mates. Equation 4.9 defines the transformation between the global (CS_0) and the local (CS_i) coordinate systems.

$$\begin{bmatrix} x_i \\ y_i \\ z_i \\ 1 \end{bmatrix}_{CS_i} = \begin{bmatrix} c[\theta_i] & -s[\theta_i] & 0 & 0 \\ s[\theta_i] & c[\theta_i] & 0 & 0 \\ 0 & 0 & 1 & 0 \\ 0 & 0 & 0 & 1 \end{bmatrix} \begin{bmatrix} x_{i0} \\ y_{i0} \\ z_{i0} \\ 1 \end{bmatrix}_{CS_0} \quad \textbf{(4.9)}$$

This transformation is required to relate motion of ball centers $(\Delta x_i, \Delta y_i)$ to the motion of the groove surfaces.

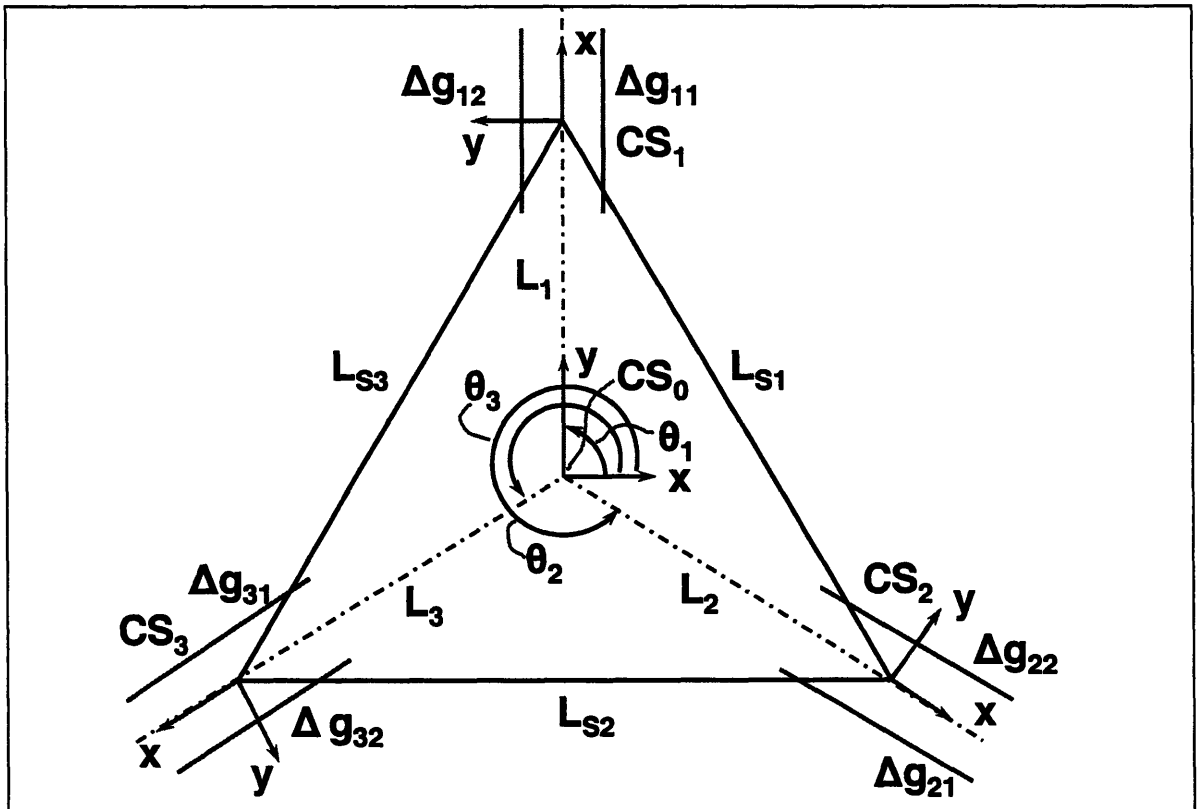

Figure 4.4: Global (CS_o) and local (CS_i) coordinate systems

4.1.3 Out-of-plane motion

Out-of-plane motions (θ_{xc}, θ_{yc} and Z_c) are captured using translations of the ball centers perpendicular to part containing the grooves. Figure 4.5 shows the planes formed by the homed and displaced position of the ball centers. Given the equations of each plane, the difference between the out-of-plane positions is found using Equations 4.10 - 4.12 [13].

$$\theta_{xc} \approx -\left(\frac{L_1.(s[\theta_1].\theta_z - c[\theta_1]).(\Delta z_2 - \Delta z_3) + L_2.(s[\theta_2].\theta_z - c[\theta_2]).(\Delta z_3 - \Delta z_1) + L_3.(s[\theta_3].\theta_z - c[\theta_3]).(\Delta z_1 - \Delta z_2)}{L_1.L_2.s[\theta_2 - \theta_1] + L_2.L_3.s[\theta_3 - \theta_2] + L_3.L_1.s[\theta_1 - \theta_3]} \right) \quad \textbf{(4.10)}$$

$$\theta_{yc} \approx \left(\frac{L_1.(s[\theta_1] + c[\theta_1].\theta_z).(\Delta z_2 - \Delta z_3) + L_2.(s[\theta_2] + c[\theta_2].\theta_z).(\Delta z_3 - \Delta z_1) + L_3.(s[\theta_3] + c[\theta_3].\theta_z).(\Delta z_1 - \Delta z_2)}{L_1.L_2.s[\theta_2 - \theta_1] + L_2.L_3.s[\theta_3 - \theta_2] + L_3.L_1.s[\theta_1 - \theta_3]} \right) \quad \textbf{(4.11)}$$

$$Z_c \approx L_1(\theta_{yc}.c[\theta_1] - \theta_{xc}.s[\theta_1]) + \Delta z_1 \quad (4.12)$$

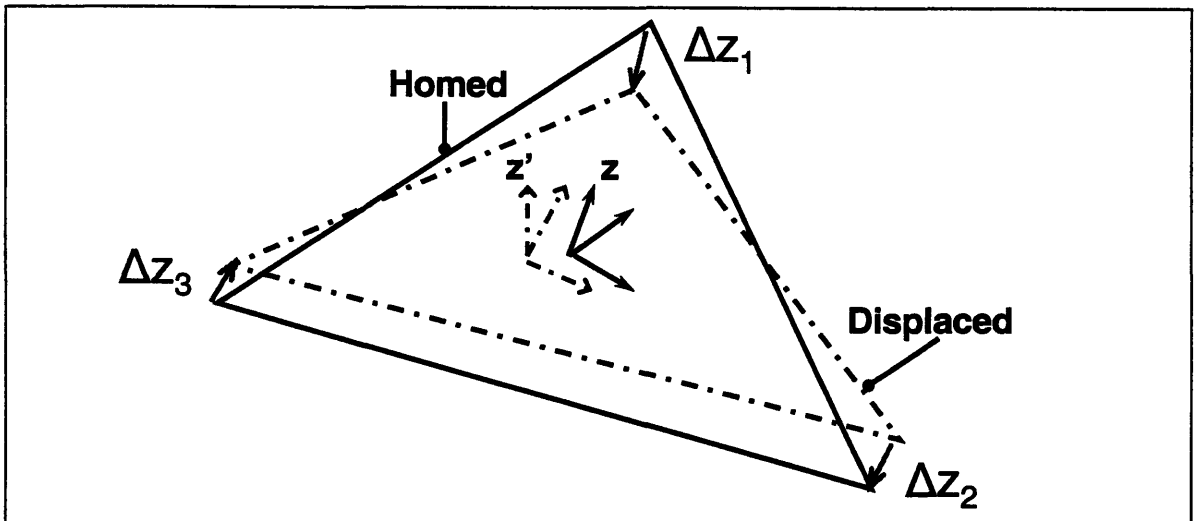

Figure 4.5: Out-of-plane motion – homed and displaced locations

In these Equations, Δz_i is the out-of-plane motion of the ball center. As in developing the in-plane kinematics, small angle approximations have been made - $\sin(\theta_{xc}) \approx \theta_{xc}$, $\sin(\theta_{yc}) \approx \theta_{yc}, \cos(\theta_{xc}) \approx 1$ and $\cos(\theta_{yc}) \approx 1$.

4.1.4 Inverse kinematics

Given the desired displacement of the coupling centroid, the task is to find the groove motions required to achieve the same. From Equations 4.6-4.8 and 4.12, we obtain the displacement of the ball centers for given displacement of coupling centroid.

$$\Delta x_{i0} = X_c - L_i.s[\theta_i].\theta_{zc} \quad (4.13)$$

$$\Delta y_{i0} = Y_c + L_i.c[\theta_i].\theta_{zc} \quad (4.14)$$

$$\Delta z_{i0} = Z_c - L_i.(\theta_{yc}.c[\theta_i] - \theta_{xc}.s[\theta_i]) \quad (4.15)$$

Equation 4.9 is used to transform the displacements to the local coordinate system CS_i.

$$\Delta x_i = \Delta x_{io}.c[\theta_i] + \Delta y_{io}.s[\theta_i] \tag{4.16}$$

$$\Delta y_i = -\Delta x_{io}.s[\theta_i] + \Delta y_{io}.c[\theta_i] \tag{4.17}$$

$$\Delta z_i = \Delta z_{io} \tag{4.18}$$

Using Equations 4.1-4.2 and 4.13-4.18, we obtain the required groove motions.

$$\Delta g_{i1} = \left(\frac{Z_c - L_i.(\theta_{yc}.c[\theta_i] - \theta_{xc}.s[\theta_i])}{\tan\alpha}\right) + \left(-(X_c - L_i.s[\theta_i].\theta_{zc}).s[\theta_i] + (Y_c + L_i.c[\theta_i].\theta_{zc}).c[\theta_i]\right) \tag{4.19}$$

$$\Delta g_{i2} = \left(\frac{Z_c - L_i.(\theta_y.c[\theta_i] - \theta_x.s[\theta_i])}{\tan\alpha}\right) - \left(-(X_c - L_i.s[\theta_i].\theta_{zc}).s[\theta_i] + (Y_c + L_i.c[\theta_i].\theta_{zc}).c[\theta_i]\right) \tag{4.20}$$

4.1.5 Forward Kinematics

This entails determining the position and orientation of the coupling centroid, given the motion of the groove surfaces. Once the groove motions are known, Equation 4.1 and 4.2 are used to find Δy_i and Δz_i in the local coordinate system, CS_i. However Δx_i is not known. It is obtained by solving the constraints given in Equation 4.21, which signify that the triangle formed by the ball centers has constant dimensional lengths (Ls_i).

$$\begin{aligned}
(\Delta x_{10} - \Delta x_{20})^2 + (\Delta y_{10} - \Delta y_{20})^2 + (\Delta z_{10} - \Delta z_{20})^2 &= {Ls_1}^2 \\
(\Delta x_{20} - \Delta x_{30})^2 + (\Delta y_{20} - \Delta y_{30})^2 + (\Delta z_{20} - \Delta z_{30})^2 &= {Ls_2}^2 \\
(\Delta x_{30} - \Delta x_{10})^2 + (\Delta y_{30} - \Delta y_{10})^2 + (\Delta z_{30} - \Delta z_{10})^2 &= {Ls_3}^2
\end{aligned} \tag{4.21}$$

Where, Δx_{i0}, Δy_{i0} and Δz_{i0} are written in terms Δx_i, Δy_i and Δz_i using Equations 4.16 - 4.18. Once Δx_{i0}, Δy_{i0} and Δz_{i0} are known, Equations 4.6-4.8 and 4.10-4.12 are used to obtain position and orientation of coupling centroid. Using the parametric model for the HPF's kinematics presented in Sections 4.1.1-4.1.5 the fixture design may be optimized for range and resolution, in six axes. Details regarding the derivations of the kinematics

and an Excel worksheet that is based upon them are available in Appendix B.

4.2 Stiffness modeling

One of the important characteristics of a fixture, as highlighted in Chapter 1, is its stiffness. To minimize positioning errors resulting from external forces, (from assembly, machining or other operations) high fixture stiffness is desirable. Higher stiffness also corresponds to higher natural frequency, which is desirable for high-speed, dynamic applications and disturbance insensitivity and rejection. This stiffness should ideally be higher than that of the machine structure, which is typically about 50 N/μm [6]. A parametric model would make it possible to (a) identify and understand factors affecting the fixture stiffness, and (b), enable design optimization to obtain desired stiffness characteristics. Absence of a model for the system would result in difficult and costly design iterations, particularly for active fixtures like the HPF, which incorporate actuators and mechanisms within their structure. Figure 4.6 depicts schematically, the contribution of actuators and mechanisms to the fixture's stiffness.

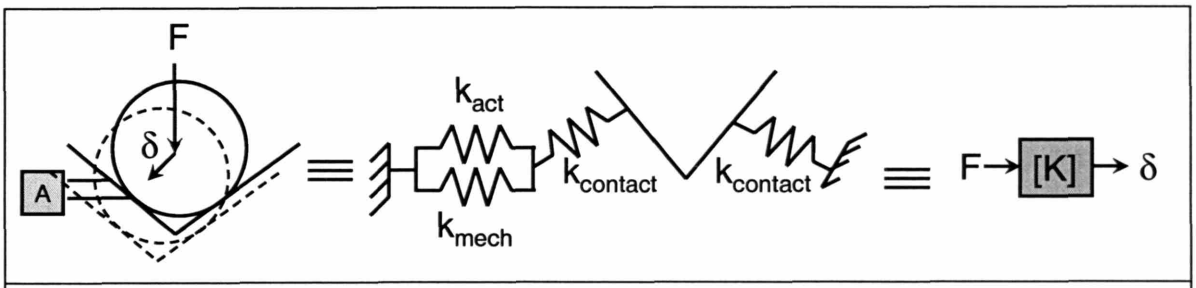

Figure 4.6: Stiffness modeling

4.2.1 Modeling overview

The first step in the modeling is to identify the components that have significant effect on the coupling's stiffness. The next step is to develop a stiffness model for each of those components. The model is expressed in terms of a 6x6 matrix relating applied forces and moments to resulting displacements in an appropriately chosen coordinate frame. This

matrix is termed the stiffness matrix, while its inverse is called the compliance matrix. Typically, these matrices are denoted by letters $\boldsymbol{K}$ and $\boldsymbol{C}$ respectively. Once the individual components have been modeled and their stiffness expressed in their respective coordinate frames, the next step is to combine them to obtain the stiffness of the whole system. To do so, the stiffness of each component is transformed to a common coordinate frame and then the stiffness are added, depending on whether the equivalent springs depicting the components act in series or in parallel. The components to be modeled are shown in Figure 4.7. Here the component marked actuator depicts both the piezoelectric actuator and its connection to six-beam flexure. The general methodology is based on parametric modeling method for flexure systems presented in [4].

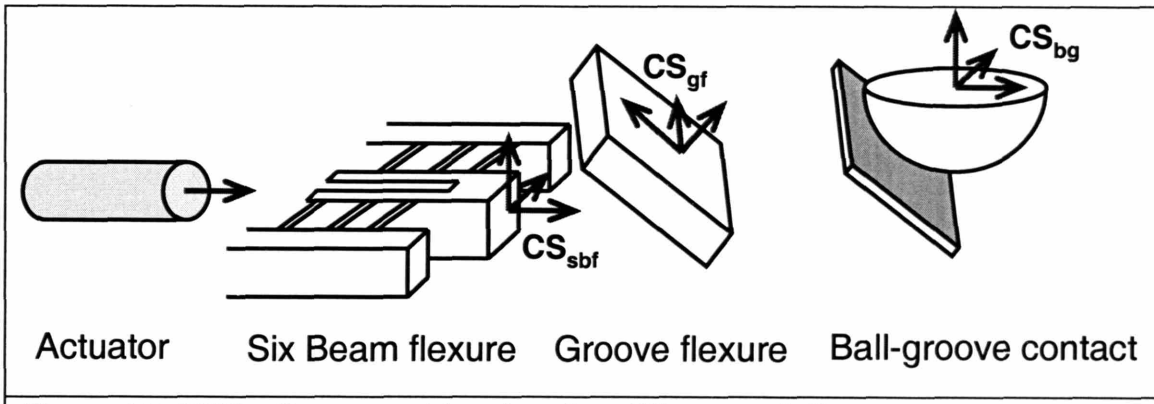

Figure 4.7: HPF – Component breakup for stiffness modeling

Figure 4.8 summarizes the above-discussed stiffness modeling steps.

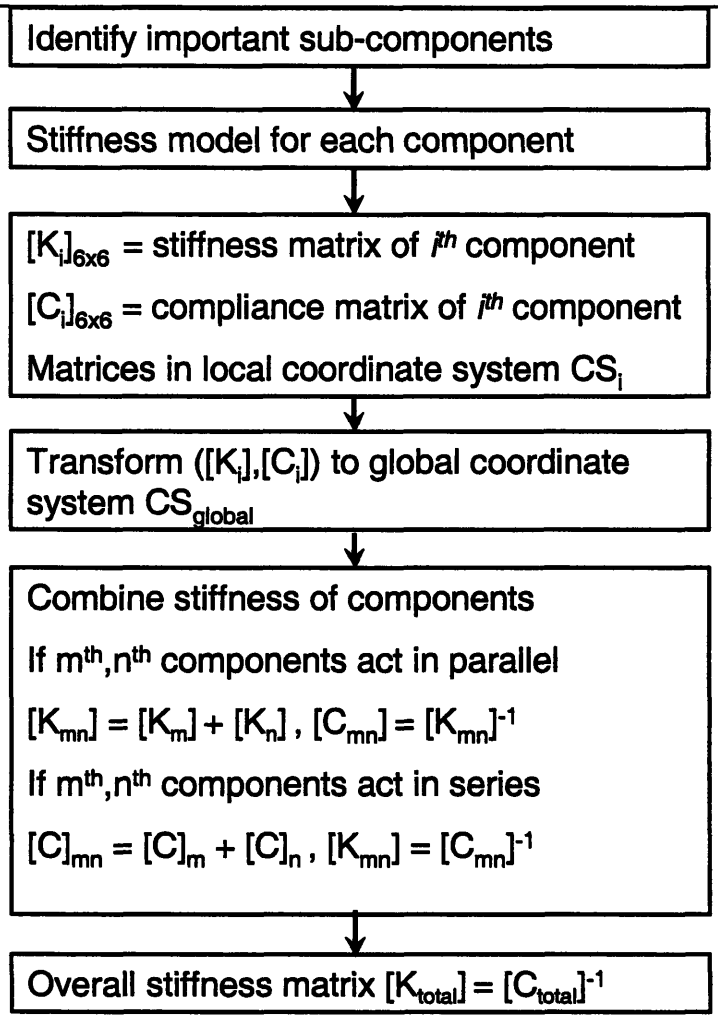

Figure 4.8: Stiffness modeling steps

4.2.2 Ball-groove contact

In developing the stiffness model for the ball-groove contact, Hertz theory for elastic contacts [23] is utilized. The stiffness of contact is a function of the force applied to it. Hence, the first step is to determine the normal force at each of the six ball-groove interfaces, given the external loads acting on the HPF. This is done by solving the equilibrium Equations 4.22 – 4.27; these equations have been adapted from [2]. The model allows for up to three sets of preload forces (Fp_j), and one set of external load (L).

The applied loads and normal contact forces are shown in Figure 4.9.

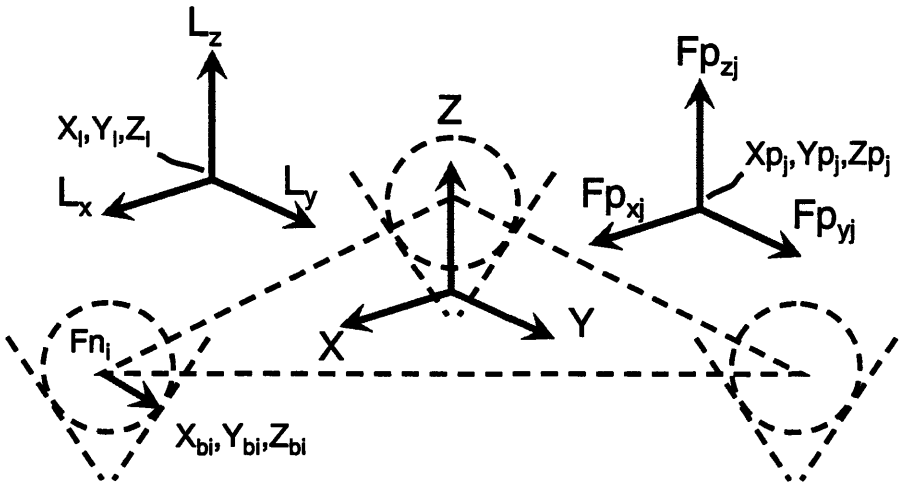

Figure 4.9: Forces acting on the HPF

To solve for the six contact forces (one for each contact), six independent equations are needed. Three equations are obtained by summing forces acting on the fixture in the X, Y and Z directions .These are given by Equations 4.22-4.24. The remaining three equations are obtained by summing the moments from the external forces about the X, Y and Z axis. These are given by Equations 4.25-4.27.

Force Equilibrium:

$$\textbf{X-axis: } \sum_{i=1}^{6} Fn_i \alpha_i + \sum_{j=1}^{3} Fp_{xj} + L_x = 0 \qquad \textbf{(4.22)}$$

$$\textbf{Y- axis: } \sum_{i=1}^{6} Fn_i \beta_i + \sum_{j=1}^{3} Fp_{yj} + L_y = 0 \qquad \textbf{(4.23)}$$

$$\textbf{Z-axis: } \sum_{i=1}^{6} Fn_i \gamma_i + \sum_{j=1}^{3} Fp_{zj} + L_z = 0 \qquad \textbf{(4.24)}$$

Fn_i are the normal contact forces

α_i, β_i and γ_i are the contact force direction cosines

Moment Equilibrium:

$$\textbf{X-axis: } \sum_{i=1}^{6} Fn_i(-\beta_i Z_{bi} + \gamma_{bi} Y_{bi}) + \sum_{j=1}^{3}(-Fp_{yj} Zp_j + Fp_{zj} Yp_j) - L_y Z_l + L_z Y_l = 0 \quad \textbf{(4.25)}$$

$$\textbf{Y- axis: } \sum_{i=1}^{6} Fn_i(\alpha_i Z_{bi} - \gamma_{bi} X_{bi}) + \sum_{j=1}^{3}(Fp_{xj} Zp_j - Fp_{zj} Xp_j) + L_x Z_l - L_z X_l = 0 \quad \textbf{(4.26)}$$

$$\textbf{Z-axis: } \sum_{i=1}^{6} Fn_i(-\alpha_i Y_{bi} + \beta_{bi} X_{bi}) + \sum_{j=1}^{3}(-Fp_{xj} Yp_j + Fp_{yj} Xp_j) - L_x Y_l + L_y X_l = 0 \quad \textbf{(4.27)}$$

Where:

X_{bi}, Y_{bi} and Z_{bi} are the coordinates of the ball-groove contacts

Fp_{xj}, Fp_{yj} and Fp_{zj} are component of the preload forces

X_{pj}, Y_{pj} and Z_{pj} are the coordinates of the preload forces

L_x, L_y and L_z are the components of the externally applied force

X_l, Y_l and Z_l are the coordinates of the external load

By solving the equilibrium equations for given coupling geometry and applied loads, the normal force at each ball-groove interface may be obtained. This information is then used to calculate the ball-groove contact stiffness. The ball-groove contact stiffness is calculated in coordinate system CSg_i, which is shown in Figure 4.10.

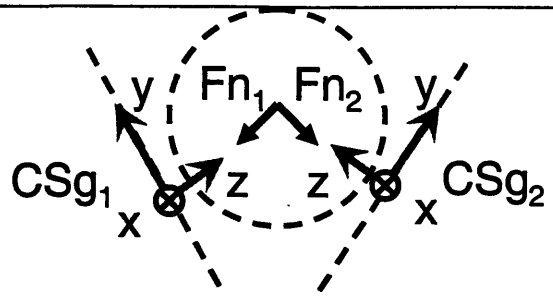

Figure 4.10: Ball-groove contact schematic

The tangential component of the ball-groove contact stiffness is given by Equation 4.28

$$K_x, K_y = \frac{16 \cdot a \cdot G_e}{3} \tag{4.28}$$

Where, Equation 4.29 gives the contact radius a and Equation 4.32 gives the equivalent shear modulus G_e.

$$a = \sqrt[3]{\frac{3Fn_i R_e}{4E_e}}, \text{Contact radius} \tag{4.29}$$

In Equation 4.29, Fn_i is the normal force acting on the i^{th} contact, R_e is the equivalent radius of curvature given by Equation 4.30 and E_e is the equivalent Young's modulus given by Equation 4.31.

$$R_e = \left\{ 0.5 \times \left(\frac{1}{R_{b1}} + \frac{1}{R_{b2}} + \frac{1}{R_{g1}} + \frac{1}{R_{g1}} \right) \right\}^{-1}, \text{Equivalent radius of curvature} \tag{4.30}$$

Where:

R_{b1}, R_{b2} (Principal radii of curvatures of ball)

R_{g1}, R_{g2} (Principal radii of curvatures of groove)

$$E_e = \left(\frac{1-\nu_b^{\,2}}{E_b} + \frac{1-\nu_g^{\,2}}{E_g} \right)^{-1}, \text{Equivalent Young's modulus} \qquad \textbf{(4.31)}$$

Where:

ν_b (Poisson's ratio - ball)

ν_g (Poisson's ratio - groove)

E_b (Young's modulus - ball)

E_g (Young's modulus - groove)

$$G_e = \left(\frac{2-\nu_b}{G_b} + \frac{2-\nu_g}{G_g} \right)^{-1}, \text{Equivalent Shear modulus} \qquad \textbf{(4.32)}$$

Where:

G_b (Shear modulus - ball)

G_g (Shear modulus - groove)

The normal contact stiffness K_z is given by Equation 4.33

$$K_z = \frac{Fn_i}{\delta_n} \qquad \textbf{(4.33)}$$

Where δ_n is the displacement normal to the contact, resulting from the normal force Fn_i and is given by Equation 4.34.

$$\delta_n = \sqrt[3]{\frac{9Fn_i^2}{16R_eE_e^2}} \tag{4.34}$$

The stiffness matrix for the i^{th} ball-groove contact is given by Equation 4.35

$$\boldsymbol{Kbg_i} = \begin{bmatrix} Kx & 0 & 0 & 0 & 0 & 0 \\ 0 & Ky & 0 & 0 & 0 & 0 \\ 0 & 0 & Kz & 0 & 0 & 0 \\ 0 & 0 & 0 & 0 & 0 & 0 \\ 0 & 0 & 0 & 0 & 0 & 0 \\ 0 & 0 & 0 & 0 & 0 & 0 \end{bmatrix}_{6x6} \tag{4.35}$$

The compliance matrix is given by Equation 4.36

$$\boldsymbol{Cbg_i} = \boldsymbol{Kbg_i}^{-1} \tag{4.36}$$

Equation 4.35 and 4.36 may be used to optimize the stiffness of the ball-groove contacts.

4.2.3 Groove flexure

The groove flexure is modeled as a combination of eight cantilever beams, as shown in Figure 4.11. The stiffness matrix is obtained by treating the flexure as combination of springs in series and parallel. The first step involves transforming stiffness of each cantilever to the base coordinate system (CS_{gf}). Each of the beam pairs 1-8, 2-3, 4-5 and 6-7 form a set of springs in series, hence compliance of the pair equals the sum of individual compliances. Finally, the overall stiffness of the flexure is obtained by adding stiffness of these pairs (since they act in parallel).

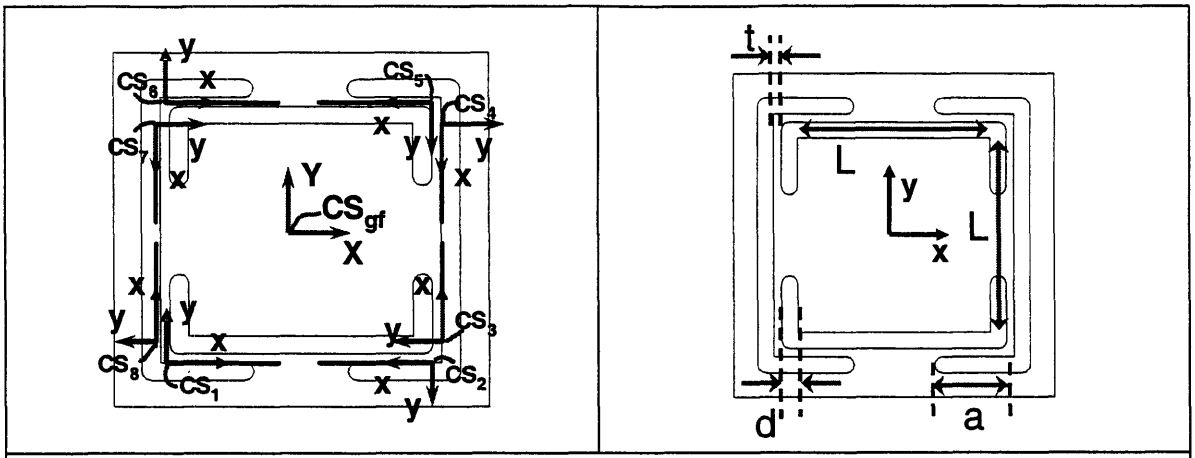

Figure 4.11: Schematic of groove flexure

A compliance matrix for a single cantilever beam is given by Equation 4.37.

$$C_{beam} = \begin{bmatrix} \frac{1}{Kxx} & 0 & 0 & 0 & 0 & 0 \\ 0 & \frac{1}{Kyy} + \frac{a}{G \cdot w \cdot t} & 0 & 0 & 0 & \frac{-1}{K\theta zy} \\ 0 & 0 & \frac{1}{Kzz} + \frac{a}{G \cdot w \cdot t} & 0 & \frac{-1}{K\theta yz} & 0 \\ 0 & 0 & 0 & \frac{1}{K\theta xx} & 0 & 0 \\ 0 & 0 & \frac{-1}{Kz\theta y} & 0 & \frac{1}{K\theta yy} & 0 \\ 0 & \frac{1}{Ky\theta z} & 0 & 0 & 0 & \frac{1}{K\theta zz} \end{bmatrix} \quad \textbf{(4.37)}$$

Where:

$$Kxx = \frac{Etw}{a}, Kyy = \frac{Ewt^3}{4a^3} \text{ and } Kzz = \frac{Ew^3t}{4a^3} \quad \textbf{(4.38)}$$

$$Ky\theta z = \frac{Ewt^3}{6a^2}, \; K\theta yz = \frac{Ew^3t}{6a^2}, \; K\theta zy = \frac{Ewt^3}{6a^2} \text{ and } Kz\theta y = \frac{Ew^3t}{6a^2} \quad \textbf{(4.39)}$$

$$K\theta xx = \frac{Gwt^3}{16a}\left[\frac{16}{3} - 3.36\frac{t}{w}\left(1 - \frac{t^4}{12w^4}\right)\right],\ K\theta yy = \frac{Ew^3t}{12a} \text{ and } K\theta zz = \frac{Ew\ t^3}{12a} \tag{4.40}$$

t = thickness of beam

a = length of beam

w = width of beam

E = Young's modulus

G = shear modulus

The stiffness matrix for the beam is given in Equation 4.41 and is obtained by taking the inverse of the compliance matrix given in Equation 4.37.

$$\boldsymbol{K_{beam}} = \boldsymbol{C_{beam}}^{-1} \tag{4.41}$$

Step 1: Transform stiffness to base coordinate system CS_{gf}.

Stiffness of j^{th} beam with respect to base coordinate system is given by Equation 4.42.

$$\boldsymbol{Kj} = \boldsymbol{Tr}(\boldsymbol{Pos}[j]) \cdot \boldsymbol{K_{beam}} \cdot \boldsymbol{Tr}(\boldsymbol{Pos}[j])^{-1} \tag{4.42}$$

$$\boldsymbol{Cj} = \boldsymbol{Kj}^{-1} \tag{4.43}$$

Where, ***Tr*** is a transformation matrix given by Equation 4.44 and defined for each beam j depending on its position with respect to the base coordinate system CS_{gf}. The components of ***Tr*** are defined in the Appendix C.

$$\boldsymbol{Tr}(\boldsymbol{Pos}[j]) = \boldsymbol{Txyz} \cdot \boldsymbol{Rz} \cdot \boldsymbol{Ry} \cdot \boldsymbol{Rx} \tag{4.44}$$

The position of the j^{th} beam is stored in the j^{th} column of the matrix ***Pos***, given by Equation 4.45.

$$\boldsymbol{Pos} = \begin{bmatrix} -D & D & D & D & D & -D & -D & -D \\ -D & -D & -D & D & D & -D & D & -D \\ -w/2 & -w/2 & -w/2 & -w/2 & -w/2 & -w/2 & -w/2 & -w/2 \\ 0 & 0 & 0 & 0 & 0 & 0 & 0 & 0 \\ 0 & 0 & 0 & 0 & 0 & 0 & 0 & 0 \\ 0 & 180° & 90° & 270° & 180° & 0 & 270° & 90° \end{bmatrix} \tag{4.45}$$

Where:

$$D = L/2 + d + t/2$$

Step 2: Express compliance of beam pairs 1-8, 2-3, 4-5 and 6-7 as a sum of individual compliances. Equation 4.46 gives the compliance of these beam pairs.

$$\begin{aligned} C_{18} &= C_1 + C_8, \; K_{18} = C_{18}^{-1} \\ C_{23} &= C_2 + C_3, \; K_{23} = C_{23}^{-1} \\ C_{45} &= C_4 + C_5, \; K_{45} = C_{45}^{-1} \\ C_{67} &= C_6 + C_7, \; K_{67} = C_{67}^{-1} \end{aligned} \tag{4.46}$$

Step 3: Obtain overall stiffness, K_{gf}, of the flexure by adding stiffness of the beam pairs. Equation 4.47 gives the overall stiffness and compliance of the groove flexure, defined in coordinate frame CS_{gf}.

$$\begin{aligned} K_{gf} &= K_{18} + K_{23} + K_{45} + K_{67} \\ C_{gf} &= K_{gf}^{-1} \end{aligned} \tag{4.47}$$

Validation of groove-flexure stiffness model

The stiffness model for the groove-flexure was implemented in MatLab (Appendix C) and was validated using CoMeT, which is a compliant mechanism synthesis tool [24]. Figure 4.12 shows the CoMeT and analytic model for the groove flexure.

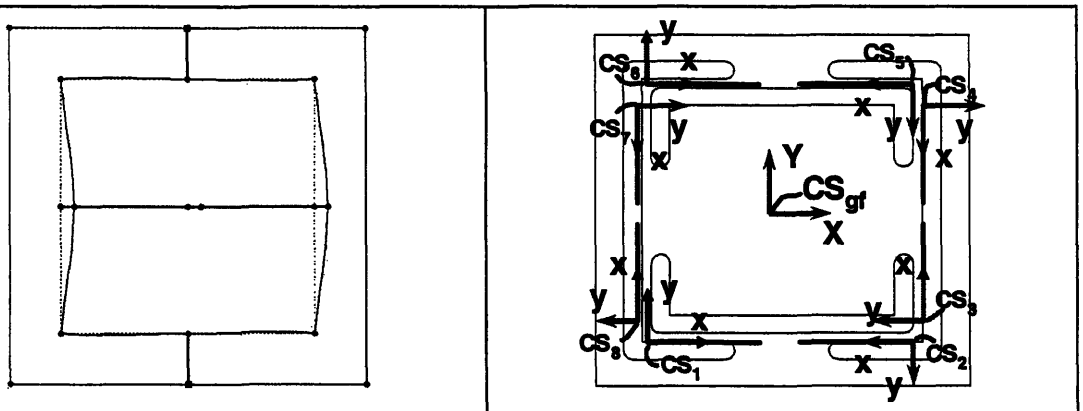

(a) CoMeT model of groove flexure | (b) Model for parametric analysis

Figure 4.12: Groove flexure schematics

Table 4.1 shows a comparison of results from the stiffness model developed above and CoMeT. The comparison is based on the diagonal elements of the [6x6] stiffness matrix.

Table 4.1: Validation of groove-flexure stiffness model

	K_{11} (N/μm)	K_{22} (N/μm)	K_{33} (N/μm)	K_{44} (kNm/rad)	K_{55} (kNm/rad)	K_{66} (kNm/rad)
CoMeT	2.12	2.12	34.25	3.44	3.44	0.40
Stiffness model	2.12	2.12	34.25	3.50	3.44	1.07
% error	0.0	0.0	0.0	1.7	0.0	63.0

The stiffness model and CoMeT agree closely, with less than 2% error, except for K_{66} that corresponds to moment/rotation about Z-axis. The discrepancy between values for K_{66} from the model and CoMeT is important and still under investigation. However, the model is still practical since there are no moment loads about the Z-axis.

4.2.4 Six beam flexure (SBF)

Stiffness of the six-beam flexure is modeled along the lines of the groove flexure. For a motion range, δz, of 50μm and beam thickness, t = 1mm, $\left(\frac{\delta z}{t}\right)^2 = 0.0025 << 1$ hence the effect of beam stiffening is negligible. Therefore, the flexure can be modeled as a set of six beams with guided end condition. Figure 4.13 shows the CoMeT and analytic model for the six-beam flexure.

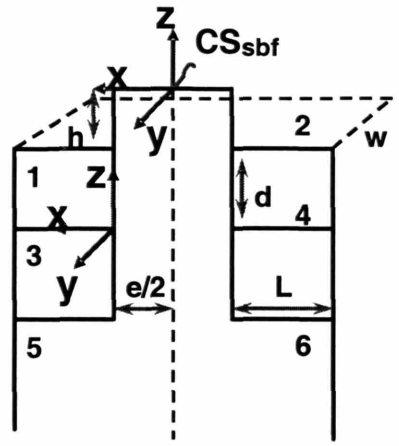

(a) Schematic for parametric analysis

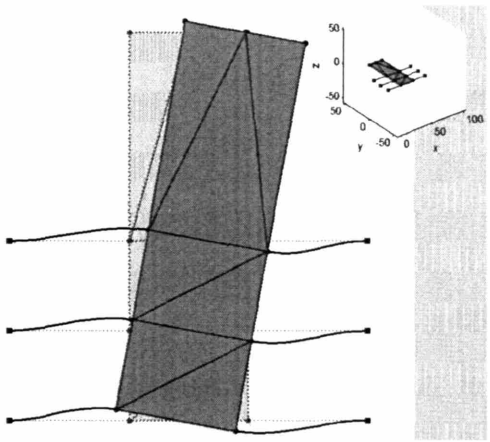

(b) CoMeT model

Figure 4.13: Six-beam flexure schematics

The modeling steps are similar to those used for the groove-flexure. A compliance matrix for a single beam with guided end condition is given by Equation 4.48. Equation 4.49 gives the corresponding stiffness matrix.

$$C_{beam} = \begin{bmatrix} \frac{1}{Kxx} & 0 & 0 & 0 & 0 & 0 \\ 0 & \frac{1}{Kyy} + \frac{L}{G \cdot w \cdot t} & 0 & 0 & 0 & \frac{-1}{K\theta zy} \\ 0 & 0 & \frac{1}{Kzz} + \frac{L}{G \cdot w \cdot t} & 0 & \frac{-1}{K\theta yz} & 0 \\ 0 & 0 & 0 & \frac{1}{K\theta xx} & 0 & 0 \\ 0 & 0 & \frac{-1}{Kz\theta y} & 0 & \frac{1}{K\theta yy} & 0 \\ 0 & \frac{1}{Ky\theta z} & 0 & 0 & 0 & \frac{1}{K\theta zz} \end{bmatrix} \quad \textbf{(4.48)}$$

$$K_{beam} = C_{beam}^{-1} \quad \textbf{(4.49)}$$

Where:

$$Kxx = \frac{Etw}{L}, Kyy = \frac{Etw^3}{L^3} \textbf{ and } Kzz = \frac{Ewt^3}{L^3} \quad \textbf{(4.50)}$$

$$Ky\theta z = \frac{Ewt^3}{6L^2} \quad K\theta yz = \frac{Ew^3t}{6L^2} \quad K\theta zy = \frac{Ewt^3}{6L^2} \textbf{ and } Kz\theta y = \frac{Ew^3t}{6L^2} \quad \textbf{(4.51)}$$

$$K\theta xx = \frac{Gwt^3}{16L}\left[\frac{16}{3} - 3.36\frac{t}{w}\left(1 - \frac{t^4}{12w^4}\right)\right], K\theta yy = \frac{Ewt^3}{12L} \textbf{ and } K\theta zz = \frac{Etw^3}{12L} \quad \textbf{(4.52)}$$

t = thickness of beam

L = length of beam

w = width of beam

E = Young's modulus

G = shear modulus

Step 1: Transforming stiffness to base coordinate system CS_{sbf}.

Stiffness of j^{th} beam with respect to base coordinate system is given by Equation 4.53.

$$Kj = Tr(Pos[j]) \cdot Kbeam \cdot Tr(Pos[j])^{-1} \tag{4.53}$$

$$Cj = Kj^{-1} \tag{4.54}$$

$$Tr(Pos[j]) = Txyz \cdot Rz \cdot Ry \cdot Rx \tag{4.55}$$

$$Pos = \begin{bmatrix} e/2 & -e/2 & e/2 & -e/2 & e/2 & -e/2 \\ 0 & 0 & 0 & 0 & 0 & 0 \\ -h & -h & -(h+d) & -(h+d) & -(h+2d) & -(h+2d) \\ 0 & 0 & 0 & 0 & 0 & 0 \\ 0 & 0 & 0 & 0 & 0 & 0 \\ 0 & 180^\circ & 0 & 180^\circ & 0 & 180^\circ \end{bmatrix} \tag{4.56}$$

Step 2: The six beams act in parallel and their stiffness are added to obtain the overall stiffness of the six-beam flexure K_{sbf}. This is given by Equation 4.57.

$$\begin{aligned} K_{sbf} &= K_1 + K_2 + K_3 + K_4 + K_5 + K_6 \\ C_{sbf} &= K_{sbf}^{-1} \end{aligned} \tag{4.57}$$

Validation of six-beam flexure stiffness model

The stiffness model for the six-beam flexure was validated using CoMeT. Figure 4.13 (a) shows the CoMeT model. Table 4.2 shows a comparison of results from stiffness model developed above and CoMeT. The comparison is based on the diagonal elements of the [6x6] compliance matrix.

Table 4.2: Validation of the six-beam flexure stiffness model						
	K_{11} (N/μm)	K_{22} (N/μm)	K_{33} (N/μm)	K_{44} (kNm/ rad)	K_{55} (kNm/ rad)	K_{66} (kNm/ rad)
CoMeT	18.73	4.4	0.797	11.67	49.5	37.88
Stiffness model	18.76	4.4	0.797	11.67	49.5	14.66
% error	0.16	0	0	0	0	61

The stiffness model and CoMeT agree closely, with less than 0.5% error, expect for K_{66} that corresponds to rotation about Z-axis. The discrepancy between values for K_{66} from the model and CoMeT is important and still under investigation. However, the model is still practical since there are no moment loads about the Z-axis.

4.2.5 Actuator and connection to SBF

The stiffness of the piezoelectric actuators used for the prototype was 20 N/μm. In addition to the actuator, the stiffness of the ball-groove connection between the actuator and the six-beam flexure has to be modeled. Figure 4.14(a) shows the ball-groove connection between the actuator and the SBF. Due to the small radius of the ball (3/16", 316 SS) attached to the actuator and the relatively low modulus of the "V" groove material (Al 6061), the contact stress (4000 MPa) exceeds the failure limit ($1.5\sigma_{yield}$ = 360 MPa for Al 6061). The indentation markings on the groove surfaces, shown in Figure 4.14(b), confirm this.

According to previous work presented in [23], if the initial loading takes the material into plastic region, it is still reasonable to expect the unloading process to be elastic. Consider the relatively hard steel ball of radius R in contact with the flat, relatively soft aluminum surface of the groove. Under load F, the indentation has radius R' slightly greater than R, due to elastic compression of the ball. Upon unloading, some elastic recovery causes the indentation to shallow, such that the permanent radius of curvature is ρ.

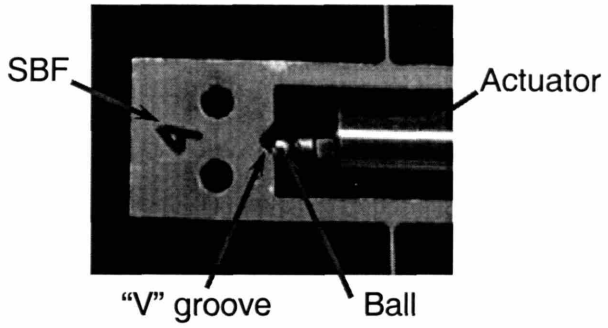

(a) Actuator-SBF connection

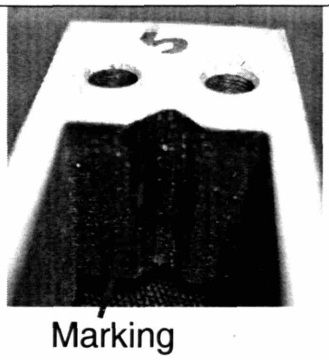

(b) Close up of "V" groove

Figure 4.14: Actuator-SBF connection

If the unloading process is elastic and indentation is not so deep as to invalidate assumptions of Hertz theory, subsequent loading will follow the elastic process in which a ball of radius R is pressed into a concave indentation of radius ρ [23]. This is depicted schematically in Figure 4.15.

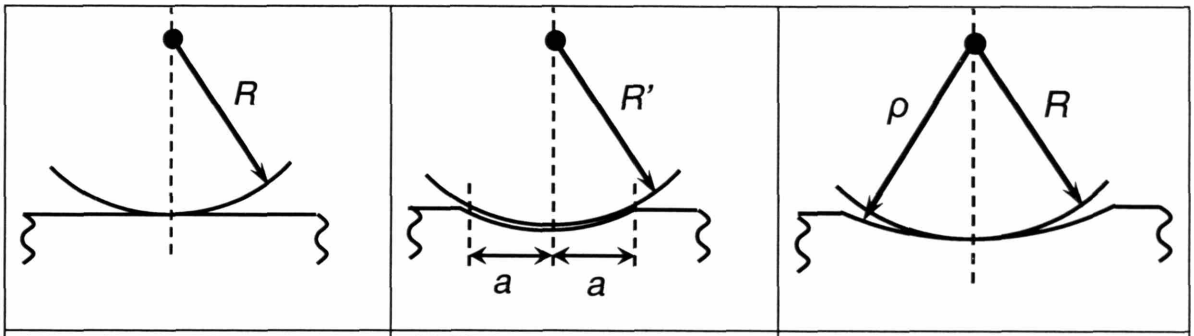

(a) Before loading | (b) Unloading | (c) Post loading

Figure 4.15: Unloading a spherical indenter (figure by K.L. Johnson, Contact Mechanics [25])

The permanent radius of curvature ρ of the indentation may be found using Equation 4.58 [23].

$$4a^3\left(\frac{1}{R}-\frac{1}{\rho}\right)=\frac{3\cdot F_n}{E_e} \qquad \textbf{(4.58)}$$

Where E_e is given by Equation 4.31, F_n is the external load and a, is given by Equation 4.34. In this case, a is the radius of the permanent indentation. The stiffness of the connection may be calculated using Equation 4.59.

$$K_{con} = \frac{F}{\delta_c} = \frac{\sqrt{2} \cdot F_n}{\left(/\sqrt{2}\right)} = \frac{2 \cdot F_n}{\delta_n} = 2 \cdot \sqrt[3]{\frac{16 \cdot F_n \cdot R_e \cdot {E_e}^2}{9}} \tag{4.59}$$

Where:

$$R_e(\text{equivalent radius of curvature}) = \left(\frac{1}{R} - \frac{1}{\rho}\right)^{-1} \tag{4.60}$$

Figure 4.16 shows the forces and deflection at the actuator-SBF connection. In calculating the stiffness of the actuator-SBF connection, the contact radius (a) was measured at 0.56mm. Accurate measurement was difficult due to the small size of indentation and difficulty in accessing the indentation location. The accuracy of the measurement is expected to be ±0.13mm. For a preload range of 45-225N, the radius of curvature of the indentation was calculated to be -2.675mm (negative sign implies the curvature is concave). Based on these values, the stiffness of the connection is 20-35 N/μm. The net stiffness of the piezoelectric actuator and the ball-groove connection, which act in series, is given by Equation 4.61 and is estimated to be 10.1 – 12.7 N/μm for a preload range of 45 – 225N.

$$K_{act-con} = \left(\frac{1}{K_{act}} + \frac{1}{K_{con}}\right)^{-1} \tag{4.61}$$

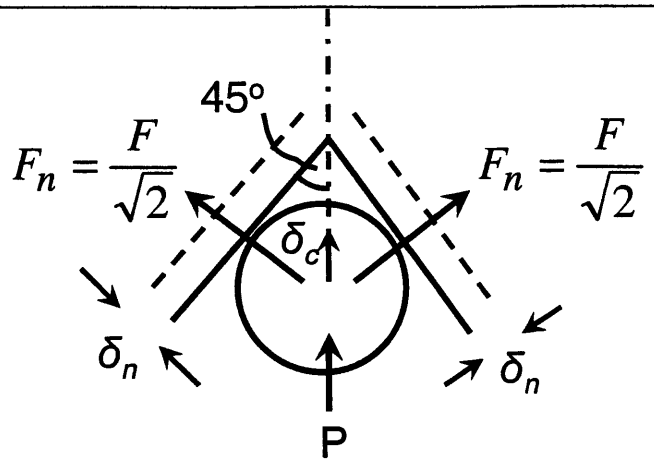

Figure 4.16: Contact forces and deflections for actuator-SBF connection

4.2.6 Overall fixture stiffness

The final steps needed to obtain the stiffness matrix for the complete system involves combining the stiffness of the individual components. The steps are listed below:

Step 1: The actuator and the ball-groove connection combined, act in parallel with the six-beam flexure. Hence, their combined stiffness is given by Equation 4.62.

$$\boldsymbol{K_I} = \boldsymbol{K_{sbf}} + \boldsymbol{K_{act-con}} = \begin{bmatrix} Kxx & & \cdots & & & \cdots \\ & Kyy & & & & \\ & & Kzz + K_{act-con} & & \cdots & \\ & & & K\theta xx & & \\ & & \cdots & & K\theta yy & \\ \cdots & & & & & K\theta zz \end{bmatrix} \quad \textbf{(4.62)}$$

This stiffness $\boldsymbol{K_I}$, is defined in the coordinate frame CS_{sbf}, shown in Figure 4.17.

Step 2: Transform $\boldsymbol{K_I}$ to the groove coordinate system, $\boldsymbol{CS_g}$. The transformation for the actuator-SBF pair is given by Equation 4.63.

$$\boldsymbol{K_I'} = \boldsymbol{Tr(Pos)} \cdot \boldsymbol{K_I} \cdot \boldsymbol{Tr(Pos)}^{-1} \quad \textbf{(4.63)}$$

Where ***Tr*** is defined by Equation 4.44 and the position matrix ***Pos*** is given by Equation 4-64 and based on illustrated in Figure 4.17.

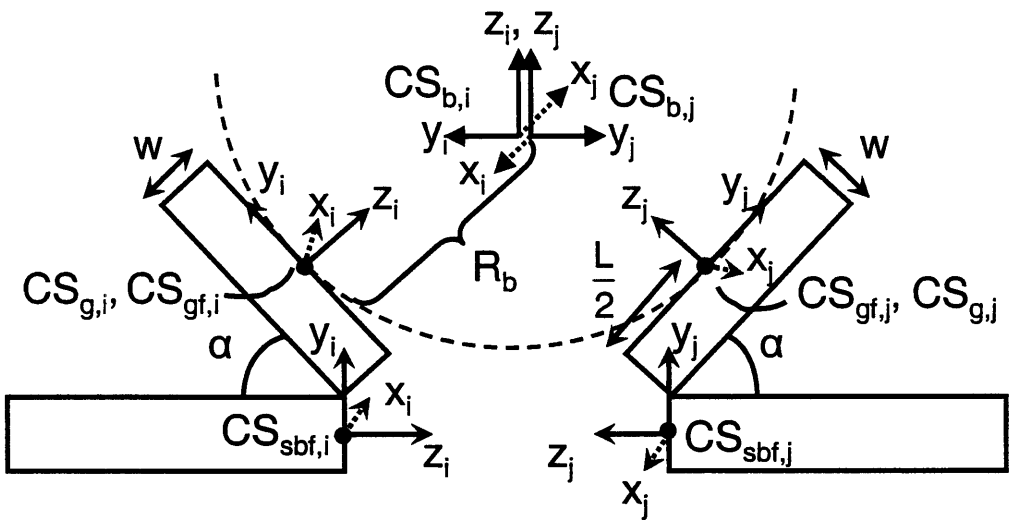

Figure 4.17: Coordinate systems used in transformation sequence

$$\boldsymbol{Pos} = \begin{bmatrix} 0 \\ -L/2 \\ -w \\ -\alpha \\ 0 \\ 0 \end{bmatrix} \tag{4.64}$$

Step 3: Combine transformed stiffness of actuator-SBF pair, stiffness of groove flexure and stiffness of ball-groove contact. Since they act in series, their compliances are added to obtain equivalent compliance of the system, C_{II}.

$$\begin{aligned} C_{II} &= C_I' + C_{gf} + C_{bg}, \text{ where } C_I' = \left(K_I'\right)^{-1} \\ K_{II} &= C_{II}^{-1} \end{aligned} \tag{4.65}$$

Here K_{II} and C_{II} are defined in the coordinate system of the groove flexure, CS_{gf}.

Step 4: Transform stiffness matrix $\boldsymbol{K_{II}}$ to the coordinate frame CS_b attached to the corresponding ball-center. Coordinate frame CS_b is shown in Figure 4.17. The resultant stiffness $\boldsymbol{K'_{II}}$ is given by Equation 4.66.

$$\boldsymbol{K'_{II}} = \boldsymbol{Tr(Pos)} \cdot \boldsymbol{K_{II}} \cdot \boldsymbol{Tr(Pos)}^{-1} \tag{4.66}$$

$$\boldsymbol{Pos} = \begin{bmatrix} 0 \\ R_b \sin\alpha \\ -R_b \sin\alpha \\ \alpha \\ 0 \\ 0 \end{bmatrix} \tag{4.67}$$

Step 5: Transform stiffness $\boldsymbol{K'_{II}}$ to coordinate system CS_{HPF} attached to the centroid of the fixture's balled-component. Coordinate system CS_{HPF} is shown in Figure 4.18. The resulting stiffness $\boldsymbol{K_{IIIj}}$ is given by Equation 4.68. Here the subscript j corresponds to j^{th} set of actuator-SBF pair, groove flexure and ball-groove contact.

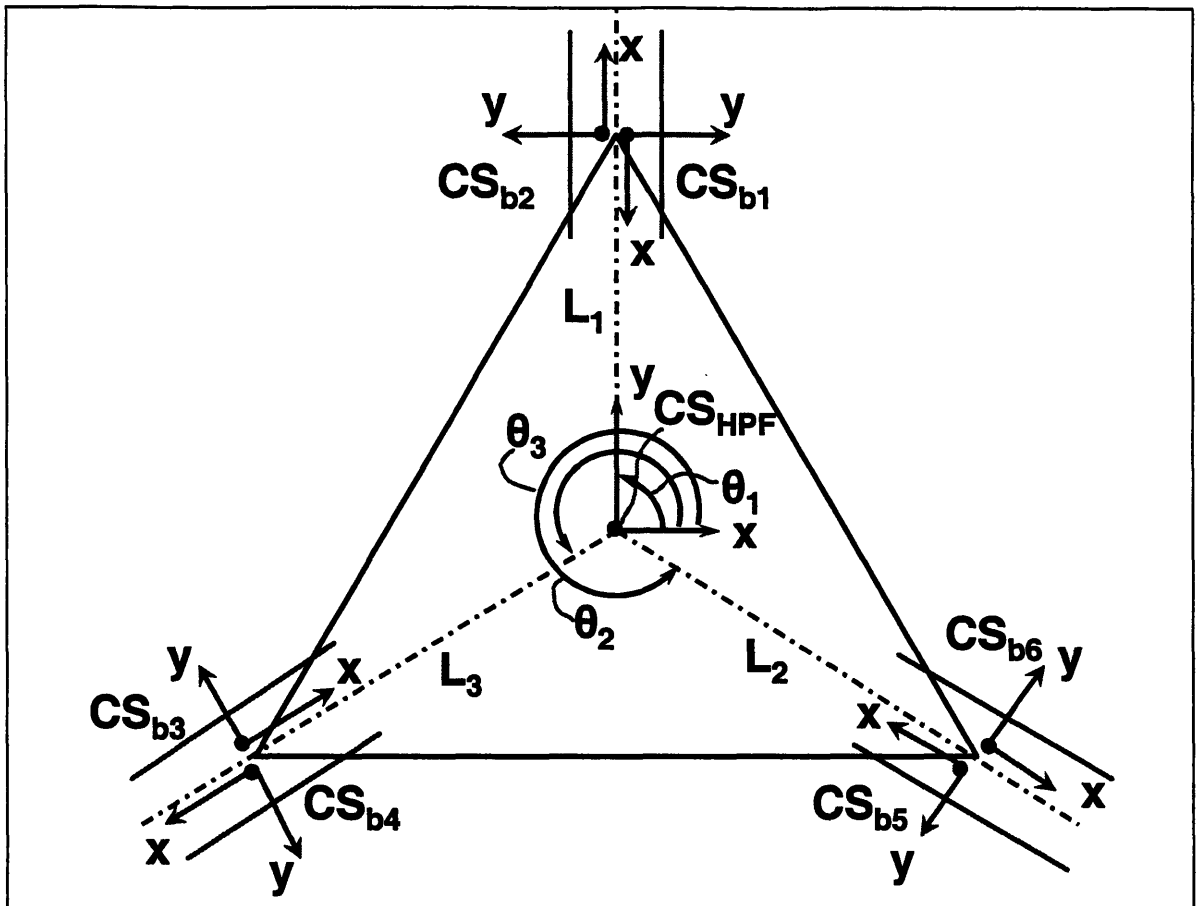

Figure 4.18: Coordinate transformation from ball-center to fixture centroid

$$K_{IIIj} = Tr(Pos[j]) \cdot K'_{II} \cdot Tr(Pos[j])^{-1} \tag{4.68}$$

The position matrix ***Pos*** is given by Equation 4.69.

$$Pos = \begin{bmatrix} L_1\cos(\theta_1) & L_1\cos(\theta_1) & L_2\cos(\theta_2) & L_2\cos(\theta_2) & L_3\cos(\theta_3) & L_3\cos(\theta_3) \\ L_1\sin(\theta_1) & L_1\sin(\theta_1) & L_2\sin(\theta_2) & L_2\sin(\theta_2) & L_3\sin(\theta_3) & L_3\sin(\theta_3) \\ 0 & 0 & 0 & 0 & 0 & 0 \\ 0 & 0 & 0 & 0 & 0 & 0 \\ 0 & 0 & 0 & 0 & 0 & 0 \\ \pi+\theta_1 & \theta_1 & \pi+\theta_2 & \theta_2 & \pi+\theta_3 & \theta_3 \end{bmatrix} \tag{4.69}$$

Step 5: Obtain overall stiffness of fixture, K_{HPF}, by combining the various K_{IIIj}'s which

act in parallel. Equation 4.70 gives the overall stiffness and compliance matrix for the HPF, defined in coordinate system CS_{HPF}.

$$K_{HPF} = \sum_{j=1}^{6} K_{IIIj}$$
$$C_{HPF} = K_{HPF}^{-1} \tag{4.70}$$

Appendix C contains the MATLAB™ code and used to implement the stiffness model. The predicted stiffness of the HPF is given in Table 4.3. Only the diagonal elements of the [6x6] stiffness matrix are listed. The variation in the fixture's stiffness over a preload range of 45 – 450N (% differences with respect to preload = 225N) is also listed.

Table 4.3: HPF stiffness – based on MATLAB™ implementation of model

	Kxx (N/μm)	*Kyy* (N/μm)	*Kzz* (N/μm)	*Kθxx* (kNm/rad)	*Kθyy* (kNm/rad)	*Kθzz* (kNm/rad)
(a) Preload = 450N	21.8	21.8	15.5	50.15	50.15	240.8
(b)Preload = 225N	20.37	20.37	14.63	47.32	47.32	223
(c) Preload = 45N	16.14	16.14	12.1	39.2	39.2	169.8
%Difference (a) and (b)	6.6	6.6	5.6	5.6	5.6	7.4
%Difference (b) and (c)	20.8	20.8	17.3	17.2	17.2	23.8

Chapter 5 - Performance of HPF

This chapter covers the experimental characterization of the prototype HPF. The chapter is organized into five sections. The first section gives an overview of various performance metrics for the HPF and the associated tests. The second section describes the test setup, which consists of a test stand, metrology system and data acquisition system. The third section covers small and large range displacement tests. Results of sustained repeatability tests are presented in section four and the fifth section presents test to characterize the fixture's stiffness.

5.1 Overview

Table 5.1 lists the various metrics and tests used to (a) verify the accuracy of the analytical models discussed in Chapter 4 and (b) to characterize performance of the HPF.

Table 5.1: Performance metrics and associated tests

Performance metrics	Test plan
Open loop positioning ability and accuracy of kinematic model (Section 4.1)	Six-axis displacement tests with command to actuators based on the kinematic model
Closed loop positioning ability	Six-axis displacement tests with adjustments to actuator input based on measured (true) fixture position
Ability of groove flexures to reduce hysteresis / stick-slip at contact interfaces	Small range motion test with the balled and grooved components engaged
Repeatability	Sustained tests to measure variation in position of fixture over repeated engagement and disengagement cycles
Fixture stiffness and accuracy of stiffness model (Section 4.2)	Stiffness tests

5.2 Test setup

The test setup consists of a stand shown in Figure 5.1, into which the fixture is mounted. A pneumatic piston applies a preload to the fixture at the center of the balled component. The preload is transferred from the piston to the fixture through a decoupling flexure that accommodates misalignment between the piston's axis and center of the fixture. The metrology system consists of six-capacitance probes, also mounted into the test stand. Three of the probes are used to measure in-plane motion and the remaining three, are used to measure out-of-plane motion. A dSPACE^{TM} data acquisition system is used to control the motion of the piezoelectric actuators, record the data and cycle the preload applied by the pneumatic piston. The underlying control sequences were prepared in Simulink and linked through dSPACE program to the external ADC and DAC channels.

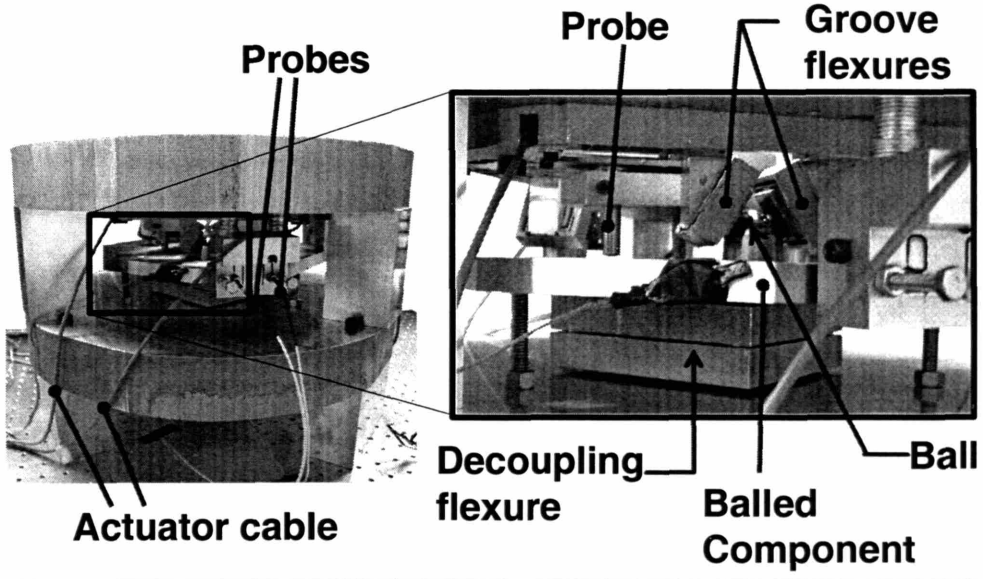

Figure 5.1: HPF assembled into test stand

5.2.1 Actuator control scheme

The hysteresis and creep associated with piezoelectric actuators requires closed loop operation, particularly when the actuator is required to achieve a stable specified position. These effects are depicted in Figure 5.2.

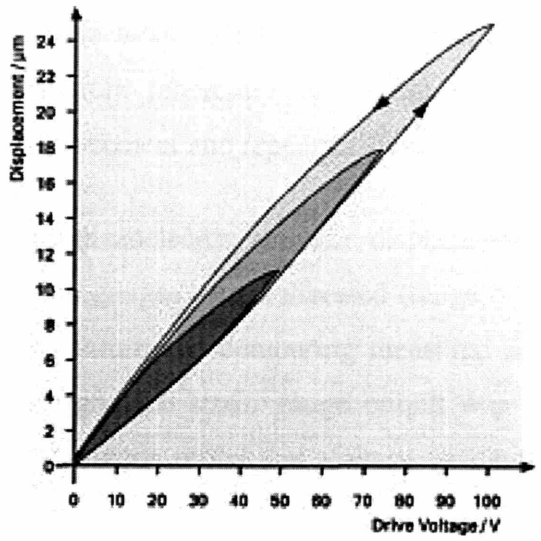

(a) Hysteresis of an open loop piezo-electric for various peak voltages

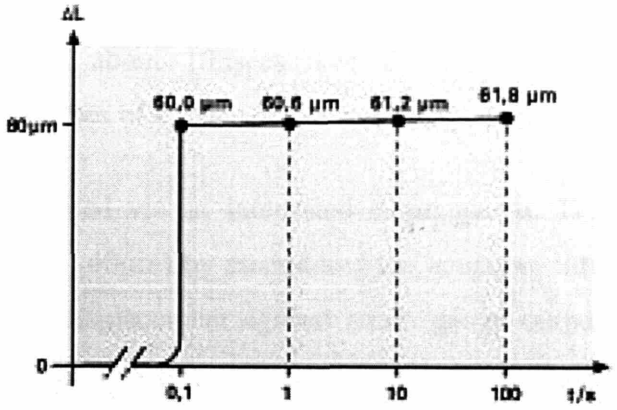

(b) Creep of open-loop PZT motion after a 60μm change in length

Figure 5.2: Hysteresis and creep of stack type piezoelectric actuator (figure from Tutorials: Displacement of Piezo Actuators [26])

Hysteresis refers to the difference in actuator motion as the voltage is increased and as it is decreased. The hysteresis of the piezos is typically about 10-15% of commanded motion. Creep refers to steady drift in actuator position over time; this effect may be described by the Equation 5.1 [26].

$$\Delta L(t) = \Delta L_{t=0.1\text{sec}}\left[1+\gamma.\log_{10}\left(\frac{t}{0.1}\right)\right] \qquad \textbf{(5.1)}$$

Where:

$\Delta L(t)$ = Creep as a function of time

$\Delta L_{t=0.1\text{sec}}$ = Displacement 0.1 secs after voltage change is complete

γ = Creep factor, typically - 0.01 - 0.02 for stack type actuators

A proportional integral controller was implemented to control the piezoelectric actuators. In this work, the time to reach steady state was not of concern, since piezoelectric actuators inherently have response times of about 10μsecs. For the purposes of displacement and repeatability tests, response times of a few seconds are acceptable.

The piezoelectric actuator displacement is sensed via an integrated strain gauge. The strain gauges were calibrated (range of motion - 40μm) by assembling the actuators into the fixture and comparing measured actuator displacement against strain gauge output voltage. The strain gauge output was measured through a Wheatstone bridge and the capacitance probe and voltage readings were recorded. A sample calibration chart is shown in Figure 5.3.

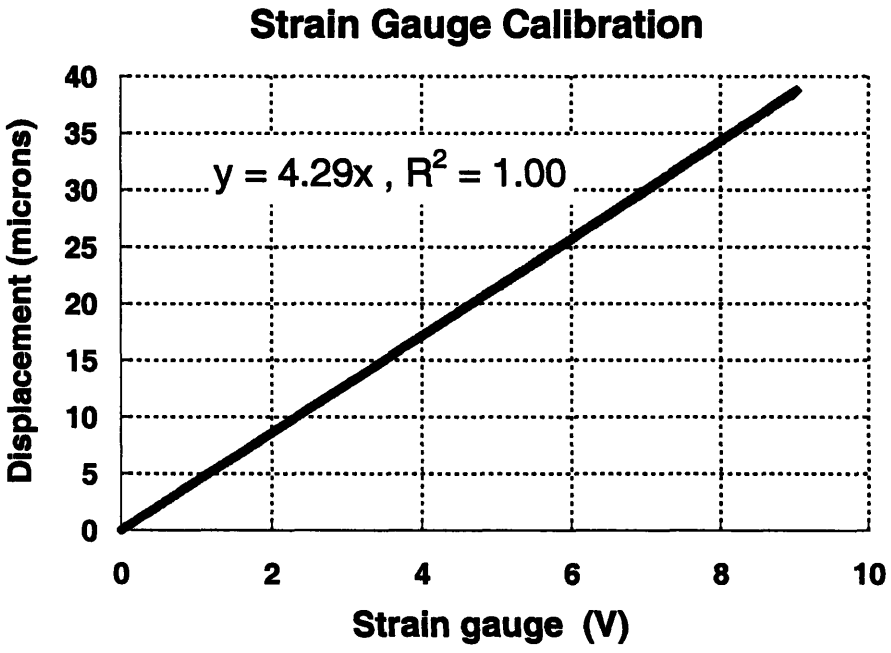

Figure 5.3: Sample strain gauge calibration chart

Table 5.2 lists the strain gauge calibration factors for the piezoelectric actuators used in the prototype.

Table 5.2: Strain gauge calibration factors					
K_{sg1} (μm/V)	K_{sg2} (μm/V)	K_{sg3} (μm/V)	K_{sg4} (μm/V)	K_{sg5} (μm/V)	K_{sg6} (μm/V)
4.399	4.154	4.167	4.299	4.314	4.111

The proportional integral controller was tuned by trial and error (K_p = 4.0, K_I = 6.0) to minimize steady state positioning errors. Electronic noise limited the positioning error (to a step input) to about 30nm. It is expected that through better controller tuning, shielding of electrical cables, amplifiers, and noise filtering, performance of the controller may be further improved. The actuator control scheme is depicted in Figure 5.4. The reference or command is a step input corresponding to desired displacement in microns. The command input is converted to voltage equivalent for the corresponding strain gauge by dividing with the calibration factor. This data is listed in Table 5.2.

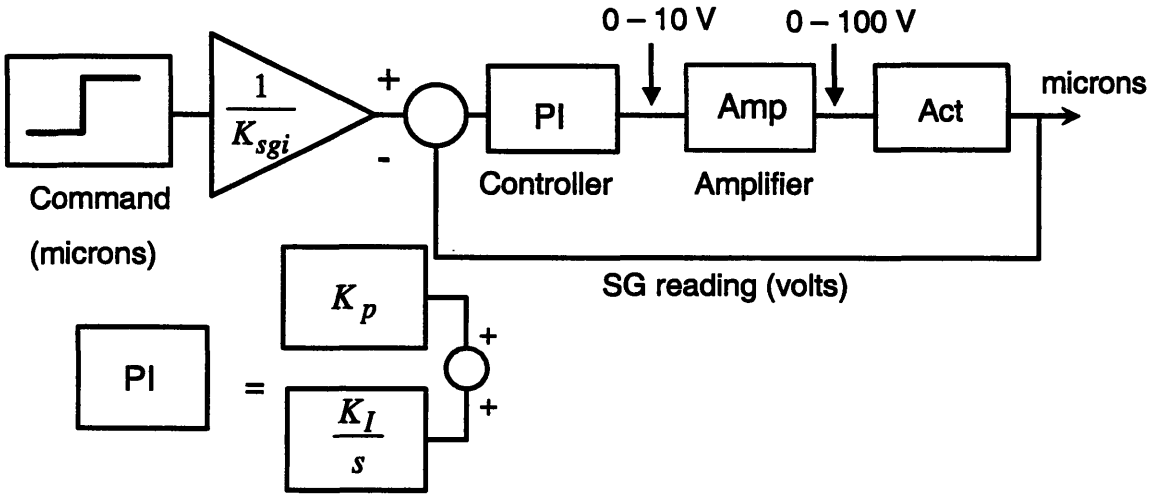

Figure 5.4: Actuator control scheme

The difference between the equivalent voltage and the strain gauge reading is sent to the controller. The controller outputs voltage in the range 0 – 10V which is amplified by a DC amplifier to 0 – 100 V before being supplied to the actuator.

5.3 Displacement tests

5.3.1 Large displacement tests without fixture position feedback

Six-axis tests were conducted to verify the kinematic model developed in Section 4-1. These tests are open loop tests, meaning that the actuators are supplied with a displacement command based on the kinematic model and the expected displacement of the HPF is compared to the measured displacement. There is no subsequent adjustment of the command to the actuators. The actuators themselves operate in a closed loop under the action of the PI controller, which ensures that they attain the commanded position.

The piezoelectric actuators are primarily "push" type actuators and hence may displace only in one (positive) direction. From the kinematic model, we know that the actuators need to move in positive and negative directions to realize motion in six-axis. To achieve this, the actuators are first moved in the positive direction by 20μm. This position is treated as home or zero position and other positions are measured relative to home. The probe settings and the 12-bit ADC channels used for these tests limited the measurement resolution to 60nm. For each axis, four test points, two on either side of the home position, were measured. The command provided to the controller (see Section 5-2) was based on the inverse kinematics model. The testing sequence was as follows:

1. Decouple the balled and grooved components of the HPF and wait for 10 seconds to allow the pneumatic piston to stabilize.
2. Move actuators to desired position. This is done by the controller based on the command inputs.
3. Wait for 50 seconds and disable position feedback to hold constant voltage.
4. Re-engage fixture components.
5. Record probe readings and average over four values.
6. Repeat steps 1-5 for next data point.

Figure 5.5 shows the results for motion in six axes. The complete test data is available in Appendix D.1. The test results agree with the kinematic model to within 5% of the

commanded motion in 80% cases, with the worst deviation being 12.1%. These deviations are systematic and may be calibrated so that the kinematic model has less than 5% error. The potential sources of error are discussed in Section 5.3.2.

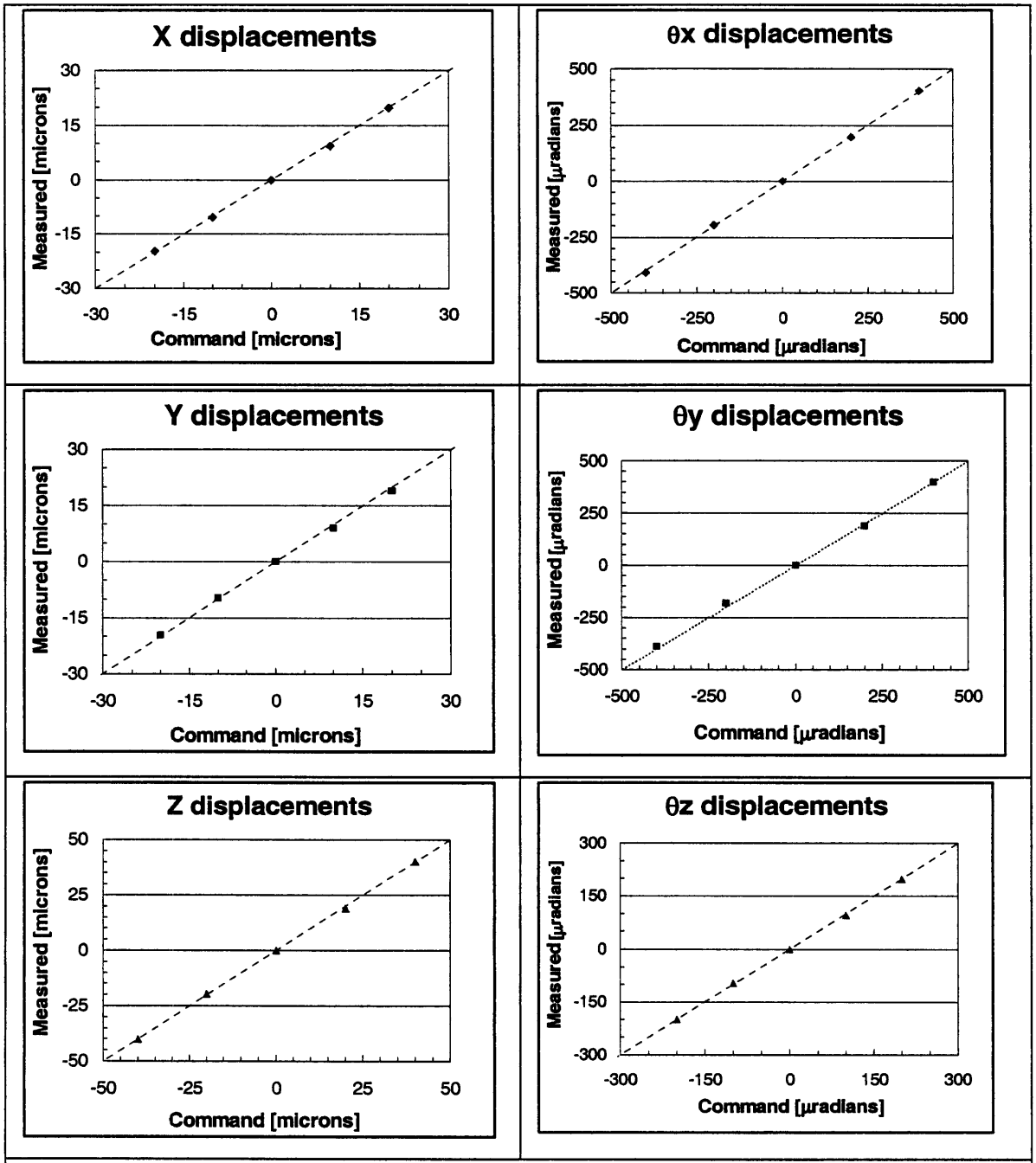

Figure 5.5: Six-axis displacement tests without fixture position feedback

5.3.2 Large displacement tests with fixture position feedback

The goal of this set of tests was to determine the closed loop positioning capability of the prototype fixture. The test procedure was similar to that used in the previous set of tests. However, after the steps 1-4, further adjustments steps (2 to 3) were carried out, based on the measured fixture position, to obtain a better match between desired and measured motions. This method is equivalent to adding a feedback loop based on measured position of the fixture. The experimental results, presented in Figure 5.6, show that positioning with less than 0.5% error (in 88% of the cases) is possible, with worst deviation being about 0.8%. This corresponds to approximately 0.1μm/2μradians for a motion of ±20μm/200μradians. Factors limiting the achieved accuracy are (a) non-repeatability of engagement-disengagement cycle (approximately 0.1μm/2μradians), and (b) resolution of measurement (for given settings approximately 0.06μm). Looking at the factors contributing to the achieved accuracy, the non-repeatability of the engagement-disengagement cycle is a dominant factor. Thus, further improvement in accuracy would entail error correction post-mating of the fixture's components and higher measurement resolution. Section 5.3.3 addresses the feasibility of error correction post-mating of the components.

Figure 5.6 and Figure 5.7 show the results for motion in six-axis and the associated parasitic (unwanted motions). The complete set of measured data is available in Appendix D.2. In addition to accuracy in the desired axis, parasitic motion in other axes should ideally be zero. Looking at the experimental data, the worst observed parasitic errors are up to 5% of the displacement in the corresponding axis. This is large compared to the accuracy in that axis (approximately 0.5%). However, several linear trends are observable in the plots of the parasitic errors. This implies that the parasitic errors are linearly dependent up on the desired motion command. As a result, these errors may be mapped and calibrated out. Even so, it is important to have an understanding of the possible causes of these errors so that they may be minimized through proper design and better fabrication.

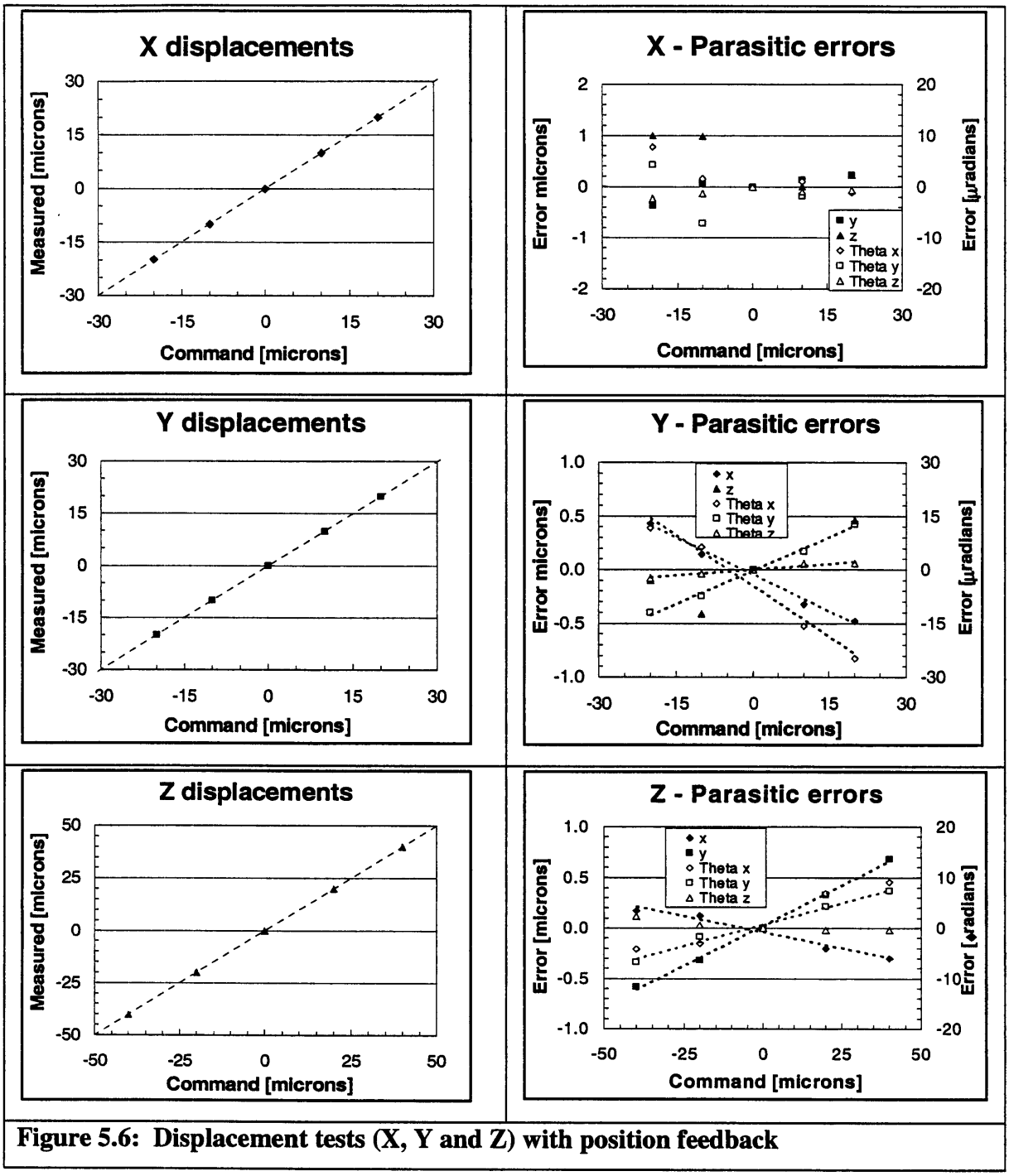

Figure 5.6: Displacement tests (X, Y and Z) with position feedback

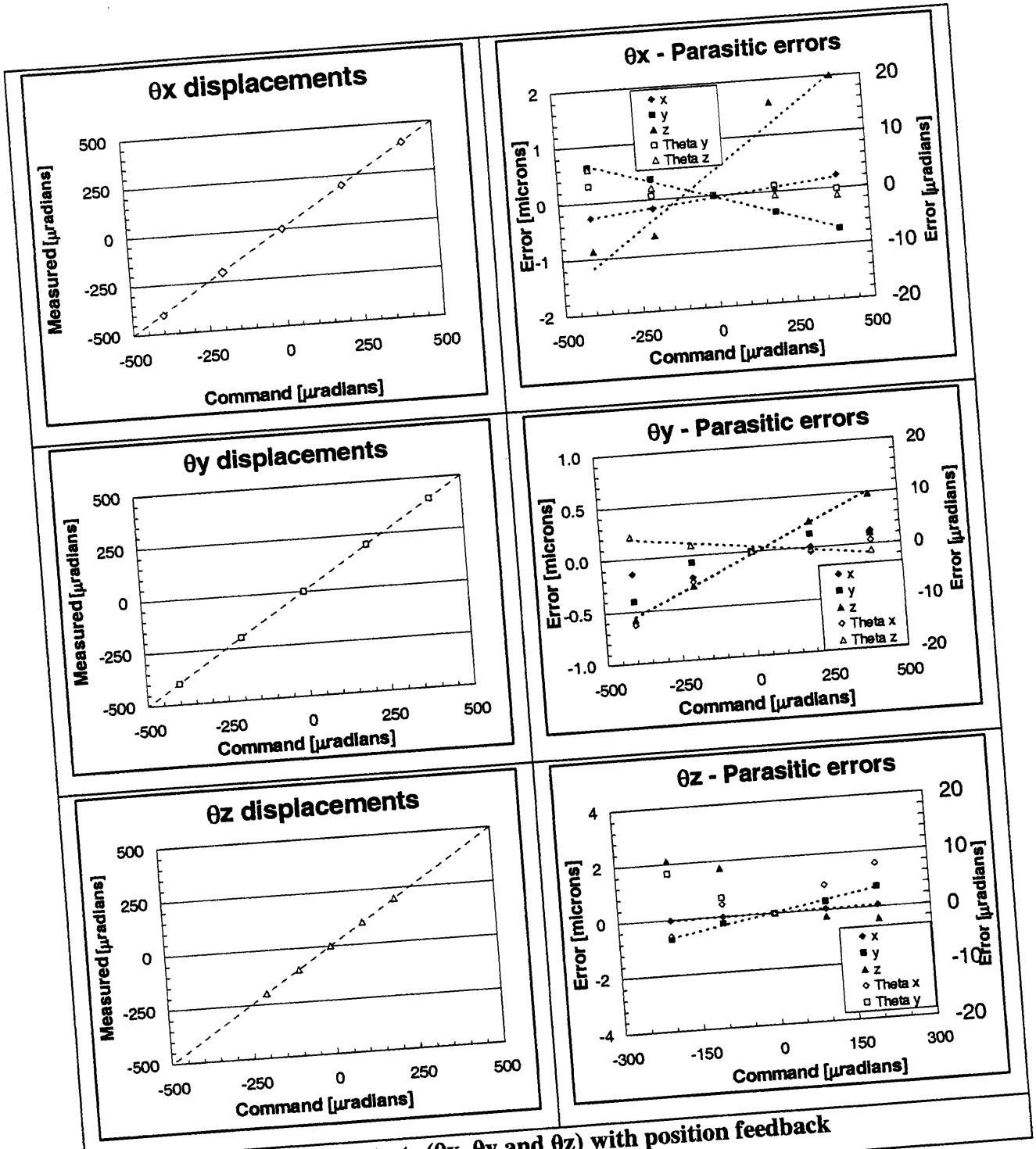

Figure 5.7: Displacement tests (θx, θy and θz) with position feedback

Potential causes of these linear parasitic errors are:

1. **Non-orthogonality of fixture's axes:** This is depicted by the angle α between the ideal Y-axis and actual Y'-axis in Figure 5.8. A motion, δ, along Y'-axis would lead to a proportional sine error ($\delta \cdot \sin\alpha$) in the X-axis measurement and a cosine error ($\delta(1-\cos\alpha)$) in the Y-axis measurement. This could arise from manufacturing and assembly errors [27]. For example, a motion of 20μm with a misalignment of 1° would result in an error of approximately 0.35 μm along the X-axis and 3nm along Y-axis.
2. **Sensor misalignment error:** This refers to a misalignment between the probe and ideal fixture axis (angle ξ). A motion along the ideal axes leads to a cosine error in the Y-axis measurement [27]. For example, a motion of 20μm with a misalignment of 1° would result in an error of approximately 3nm. This is much smaller than the measured parasitic error hence it is not expected to be a major source of error.
3. **Actuator alignment errors:** This refers to misalignment between the ideal direction of motion of the actuator and the actual direction of motion.

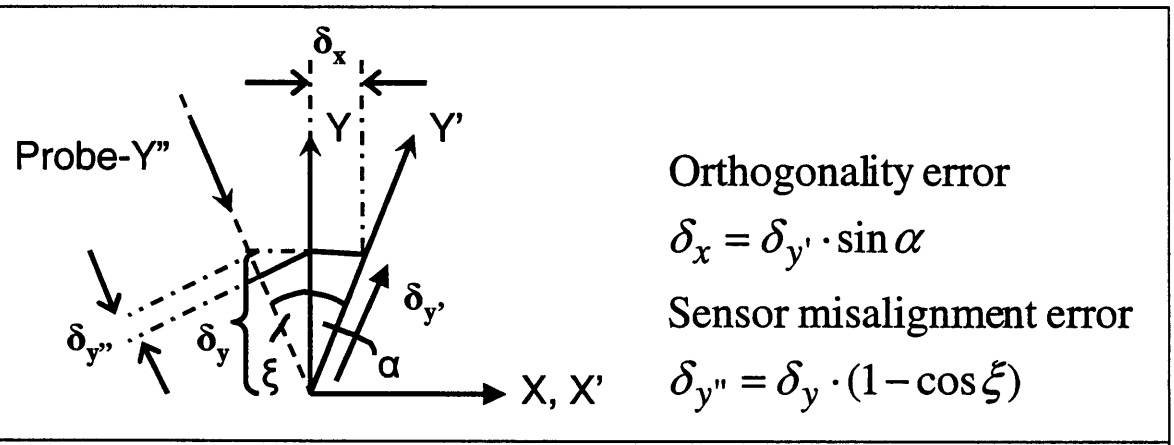

Figure 5.8: Linear parasitic error sources

The linear and repeatable nature of parasitic errors suggests that these are systematic and may potentially be minimized through mapping, careful sensor alignment and better manufacturing and assembly methods. Other error sources include straightness errors

associated with the fixture's axes and non-repeatability associated with fixture's engagement and disengagement cycle (approximately 0.1μm/2μradians).

5.3.3 Small displacement tests

Two other important questions that need to be answered with regard to the fixture's positioning ability are:

1. Does the groove flexure minimize stick slip at the contact interface and if so, is there a direct method to validate this?
2. Can deviation between commanded and achieved fixture position be eliminated post engagement of the fixture components? This would greatly simply the implementation of a closed loop control based on feedback of the fixture's true position.

The answer to both of these questions is in the affirmative if the fixture can execute fine (nanometer-scale) motion over a few microns, without sudden shifts in position due to stick-slip at the contact interfaces.

For a preload of 112.5 – 225 N, the normal load, F, on each contact surface is 38-75 N. This corresponds to a tangential contact stiffness of 17.6-22 N/μm, in the absence of the groove flexure. The maximum tangential force that may be applied before slip occurs is given by μF, where μ is the static friction coefficient. For lubricated steel on steel, μ = 0.16 and the corresponding tangential force is 6 – 12 N. Consequently, in the absence of the groove flexures, the maximum displacement that may be expected before stick slip occurs is approximately 0.3–0.5μm. To address the previously posed questions, a small displacement test was carried out in one axis of motion, the Y-axis. In these tests, capacitance probes were set at high resolution which corresponds to a noise floor of 2nm. In the test, 16-bit ADC channels were used. A displacement range of 3μm was chosen for this test to ensure that any stick slip that might normally occur in the absence of the flexure, would be captured. The test procedure is described below:

1. Engage and preload the balled and grooved components of the HPF and wait for 30 seconds to allow the balls to settle into the grooves.
2. Move actuators with incremental voltage input (0.00125 volt step every sec) until supply voltage reached 0.5 volts. This is set as the start or home position.
3. Utilize the actuation scheme to cause motion of the fixture along the Y-axis.
4. Record probe readings every 250msecs and average (four readings for each step).
5. Stop the test when the voltage supplied to the actuators reaches 1 volt.

The test results plotted in Figure 5.9 (a) and (b) show that the supplied voltage increments result in 3μm of motion along the Y-axis with displacement increments of 4nm. The results do not show sudden jumps (0.3-0.5μm) that would indicate stick-slip associated with relative motion at the contact interfaces.

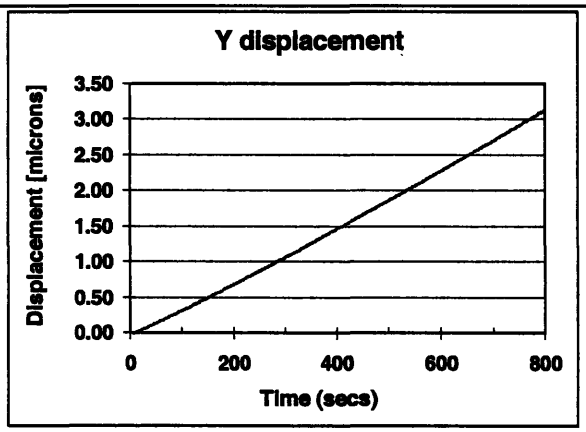

(a) Small range motion along Y axis

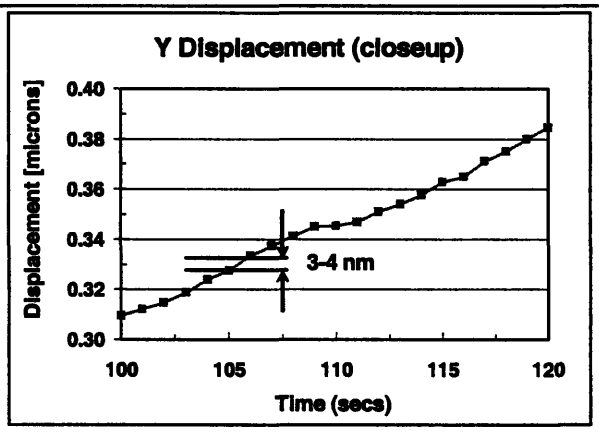

(b) Close-up of motion along Y axis

Figure 5.9: Small displacement motion along Y axis and associated in-plane parasitics

5.4 Sustained repeatability tests

Over 1000 cycles of engagement and disengagement were performed to characterize the fixture's repeatability. The air-piston, described in Section 5.2, was used to perform the engagement/disengagement process. The piston was controlled via a solenoid valve. In the engaged state, the piston provided a 225N preload force. The test required 14 hours to

complete and throughout the duration of the test, the actuators were supplied with a constant 2 volts. This ensured that the actuator-SBF connections were properly preloaded. The test procedure is described below:

1. Supply all actuators with a constant voltage of 2volts.
2. Engage the balled and grooved components of the HPF
3. Wait for 30 seconds
4. Record probe readings (10 readings over 10 seconds)
5. Disengage the coupling components
6. Wait for 5 seconds
7. Repeat steps 1 - 6

In characterizing the fixture's repeatability, we are particularly interested in what may be said about the data when the ball-groove surfaces are potentially:

1. Not yet affected by wear: Readings 1- 100
2. Stabilized / worn in: Readings 700-1000

Looking at Table 5.3, the fresh (1 – 100 cycles) and settled 1 σ data (700 - 1000) show less than 0.09μm/1.2μradian of difference, strongly indicating that there is no substantial wear process. This also suggests that there is very little relative motion between groove and ball surfaces and the flexural elements incorporated in the "V" grooves are effective in reducing frictional hysteresis. Thus, sustained nanometer-level repeatability is provided by the fixture.

Table 5.3 Standard deviation of fixture position (repeatability test)

Data Range	X [μm]	Y [μm]	Z [μm]	θx [μradian]	θy [μradian]	θz [μradian]
001-100	0.04	0.05	0.07	0.64	0.57	2.02
700-1000	0.03	0.03	0.16	0.89	0.59	0.82
001-1000	0.06	0.09	0.29	1.45	1.03	2.26

Figure 5.10 presents the repeatability test data. Looking at Figure 5.10, we see that the Z-axis motion shows a steady drift in position. This may partly be explained by the creep of piezoelectric actuators. From kinematics, explained in previous section, we know that if all actuators move in one direction, a pure motion in Z-axis is expected. This may add up to about 0.5 microns over the duration of the test. The creep is expected to follow a logarithmically relation, implying that over time, the creep should tend towards a steady value. This is not observed in the test data. Particularly beyond 600 cycles, the drift seems to be increasing. Another reason for the drift could be temperature variation in the room over the duration of the testing (14 hours). The only asymmetry in both the HPF and the test stand is about the horizontal plane. Therefore, a temperature variation is expected to produce a displacement predominantly in the Z direction. The amount of thermal variation is consistent with magnitude of thermal variations that have been previously measured in this test setup.

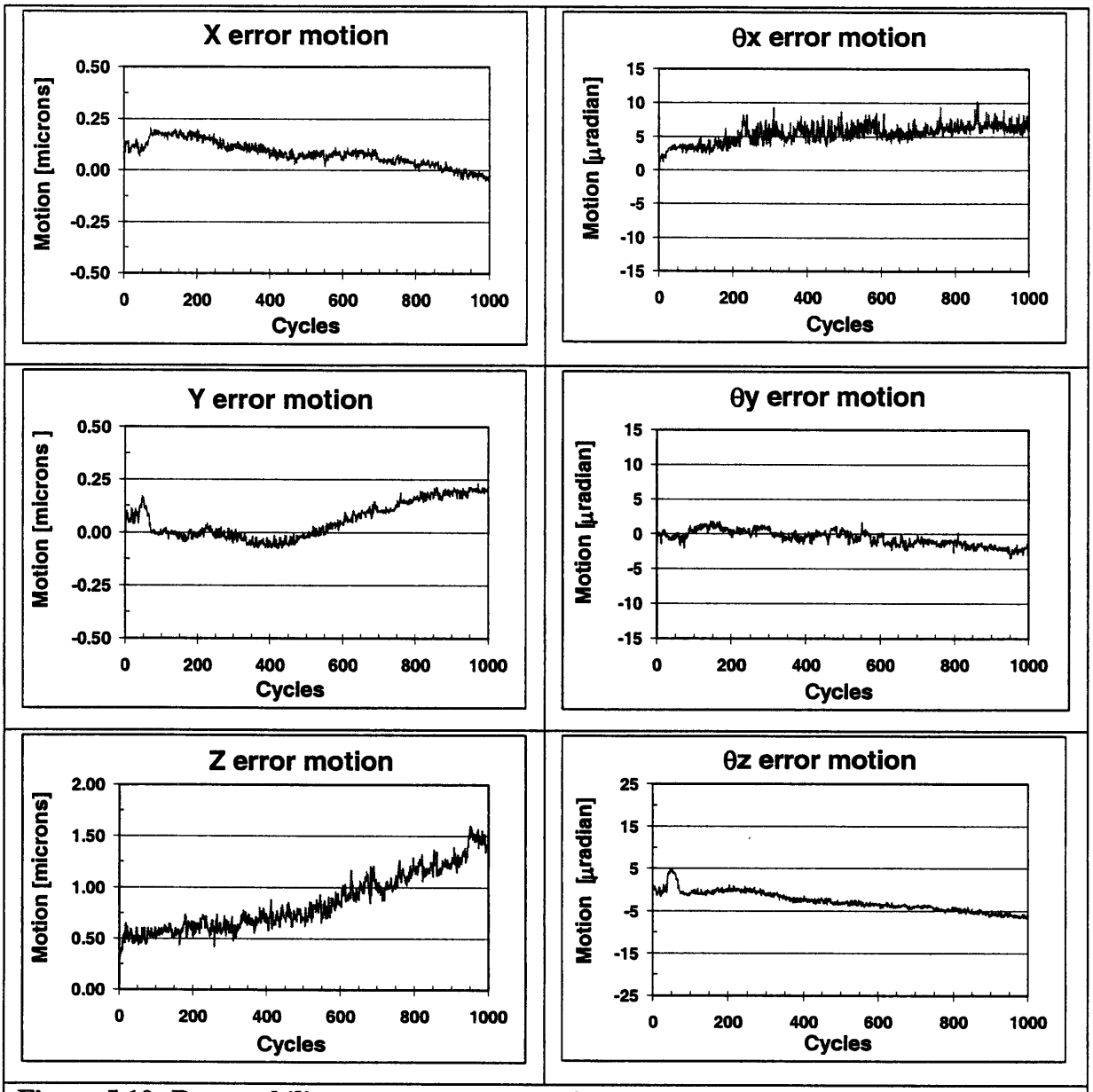

Figure 5.10: Repeatability tests at constant voltage

5.5 Stiffness tests

These set of tests are aimed at characterizing the stiffness of the fixture and evaluating the accuracy of the analytical model. Initial stiffness measurements showed a difference of up to 65% between measured and predicted stiffness. Upon further investigation, it

was found that the original model for the SBF did not account for some of the compliance associated with the structure of the HPF. The original CoMeT model of the SBF was extended to incorporate these additional compliances. The original and extended CoMeT models are shown in Figure 5.11. The additional compliance is due to the beam elements shown in Figure 5.11(a). The extended CoMeT model was used to form a modified stiffness matrix for the SBF and the analytical model was again used to estimate the fixture stiffness. A comparison between the results from the experiment and the modified analytical model is presented in Table 5.4.

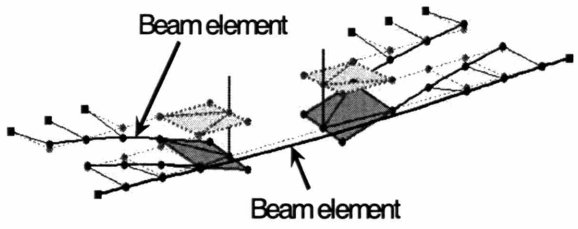

(a) Extended CoMeT model of SBF, note inclusion of beam elements to more accurately model fixture stiffness

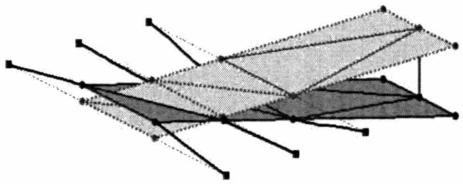

(b) Original CoMeT model of SBF

Figure 5.11: CoMeT models of SBF

It is important to note that the original fixture design may be modified easily to minimize these additional compliances, in which case the original model would be applicable.

Table 5.4: HPF stiffness – experimental vs. analytical results

	Kx (N/μm)	*Ky* (N/μm)	*Kz* (N/μm)
Experimental	10.03	10.03	10.13
Analytical model	7.05	7.1	7.30
% Error	29.7	29.2	27.9

Chapter 6 - Thin coatings

One of the ways of improving repeatability of precision fixtures and reducing contact wear is to use hard surface coatings. Design of coated interfaces requires the knowledge of stresses in the coating, interface and substrate. This chapter discusses the non-linear finite element analysis of thin coatings and guidelines to designing good quality coated interfaces.

6.1 Introduction

Two principal factors affecting performance of precision kinematic fixtures (kinematic couplings) are friction at the interface and wear of contacting entities. As discussed in Chapter 1, the high stiffness, wear resistance and low friction coefficient of the ceramic materials makes them especially suited for use in designing the ball-groove elements of the fixture. However, custom coupling components made from ceramic materials are difficult and expensive to manufacture. Due to these considerations, hard-coated ball-groove surfaces were explored as a cost effective alternatives to high cost ceramic components [11].

Several applications in addition to precision couplings use thin, hard metallic and non-metallic coatings to improve tribological characteristics such as friction and wear of surfaces; examples include bearings and bearing races, precision gears, automotive parts medical devices, cutting tools, aerospace components and the like [28]. One of the critical factors in the design of these coatings is the stress distribution within the coating and substrate, under the action of an external load. This knowledge is essential to understanding factors affecting the failure of the coating and designing quality interface.

6.2 Previous work

Surface coatings have been extensively analyzed both experimentally and through simulated (finite element) indentation tests. The observed behavior has been explained in terms of stress distributions [29,30,31,32]. Finite element studies relating these stresses to coating parameters (thickness to contact radii ratio, coating to substrate modulus ratio) have been carried out by Djabella and Arnell [14,15]. These studies, however, do not cover coatings with thickness to contact radius ratio $\left(\frac{t_c}{a}\right) < 0.1$, which constitute typical surface coating configurations. Additionally, owing in part to complexity of observed behavior; concrete usable guidelines for designing coated interfaces have not been available.

6.3 Motivation

The behavior of stresses in thin coatings $\left(\frac{t_c}{a} < 0.1\right)$, as will be shown subsequently, cannot be extrapolated from results for thicker coatings $\left(\frac{t_c}{a} \geq 0.1\right)$. This has erroneously been assumed by Djabella and Arnell in [14,15]. The typical coating thickness employed in most applications is on the order of a few microns. For example, TiN coating thickness ranges from 0.25-12μm with typical values ranging from 1-5μm [33]. In applications such as kinematic coupling interfaces and bearing surfaces, the contact radius (a) may easily be a few hundred microns. For example consider a steel ball (Young's modulus, E = 210 GPa) of radius 0.25" in contact with a flat steel surface under a load of 200N. Based on Hertz theory, the contact radius $a = 208\,\mu\text{m}$. Thus, coatings with thickness < 20 microns correspond to the class $\frac{t_c}{a} < 0.1$. In heavily loaded contacts, the contact radius may be several hundred microns. Thus, typical hard surface coating configurations would

correspond to $\frac{t_c}{a} < 0.1$, hence the need for the present study.

6.4 Goals of the study

The present work analyzes stress distributions in coated interfaces with thickness ratios $\left(\frac{t_c}{a}\right) = 0.0125 - 1.0$ and modulus ratios $\left(\frac{E_c}{Es}\right) = 1.0 - 4.0$. Further, the effectiveness of hard and soft interlayer (used between coating and substrate), in reducing stresses, is analyzed. Focus is maintained on thin coatings $\left(\frac{t_c}{a} < 0.1\right)$ and design guidelines, along with analytical expressions are provided, relating observed behavior to design parameters.

6.5 Finite element model

6.5.1 Model description

In creating the FEA model, effects of friction on the contact stresses were neglected and only normal loads were considered. The assumption is reasonable particularly for ceramic materials that have low friction coefficients (approximately 0.2). The configuration studied consists of a steel "V" groove (substrate) with a single coating layer (monolayer), brought in gradual contact with an uncoated steel ball. Figure 6.1 shows a schematic of the finite element model used in the investigation.

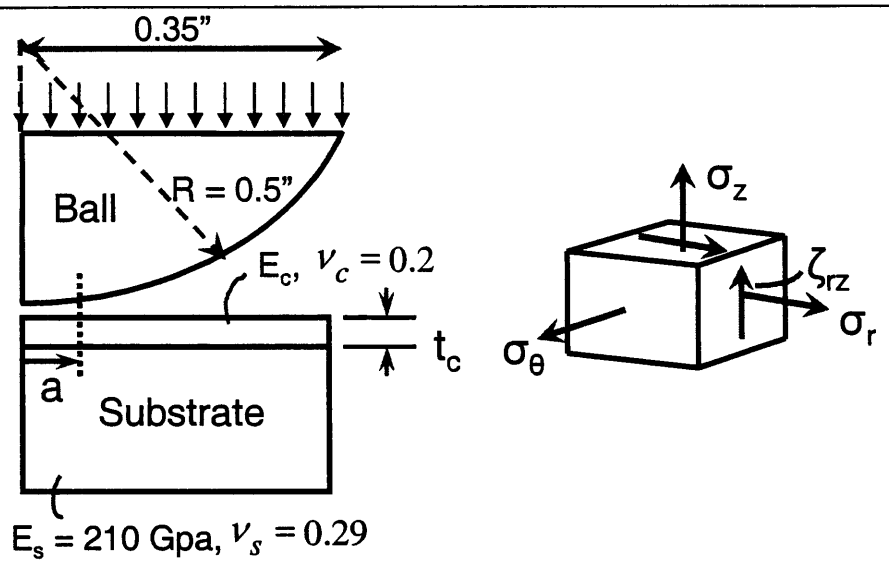

Figure 6.1: Finite element model - schematic

The final meshed model contained approximately 70,000 elements. In line with recommendations found in literature [14,15], the model size was kept $> 30a$ to accurately capture Hertzian stress distributions. Results from the FEA without coating were compared to Hertz theory to validate the model. Results are shown in Table 6.1. The contact conditions resulting from applied load were; contact radius a = 152 μm and maximum contact pressure p_o = 860 MPa.

Table 6.1: Comparison of FEA model and Hertz theory

	$\frac{\sigma_r}{p_0} = \frac{\sigma_\theta}{p_0}$ (center of contact)	$\frac{\sigma_r}{p_0} = -\frac{\sigma_\theta}{p_0}$ (edge of contact)	$\frac{(\tau_{princ})_{max}}{p_0}$ (max shear stress)	Location of max shear stress
Hertz theory	$\left(\frac{1+2\nu}{2}\right) = 0.79$	$\left(\frac{1-2\nu}{3}\right) = 0.14$	0.31	$0.48a$
FEA	0.778	0.138	0.3059	$0.473a$
% Deviation	1.52 %	1.43 %	1.32 %	1.46 %

Location and magnitude of stresses in all subsequent simulations were normalized with respect to these values $\left(\frac{r}{a}, \frac{\sigma}{p_0}, \frac{t_c}{a}\right)$. It was observed, that variations in Poisson ratio from 0.2 – 0.3, which covers most metallic and ceramic coatings, has little effect on the stress distribution. Table 6.2 and Figure 6.2 depict the small difference in stresses for Poisson ratios (ν) 0.2 and 0.25. Subsequent analyses were carried out for Poisson ratios (ν) = 0.2.

Table 6.2: Stresses at the coating-substrate interface for ν = 0.2 and 0.25

	σ_r (r = a) (edge of contact)	σ_z (r = 0) (center of contact)	$\tau_{max\ (Principal)}$
% Difference	3 %	1 %	3 %

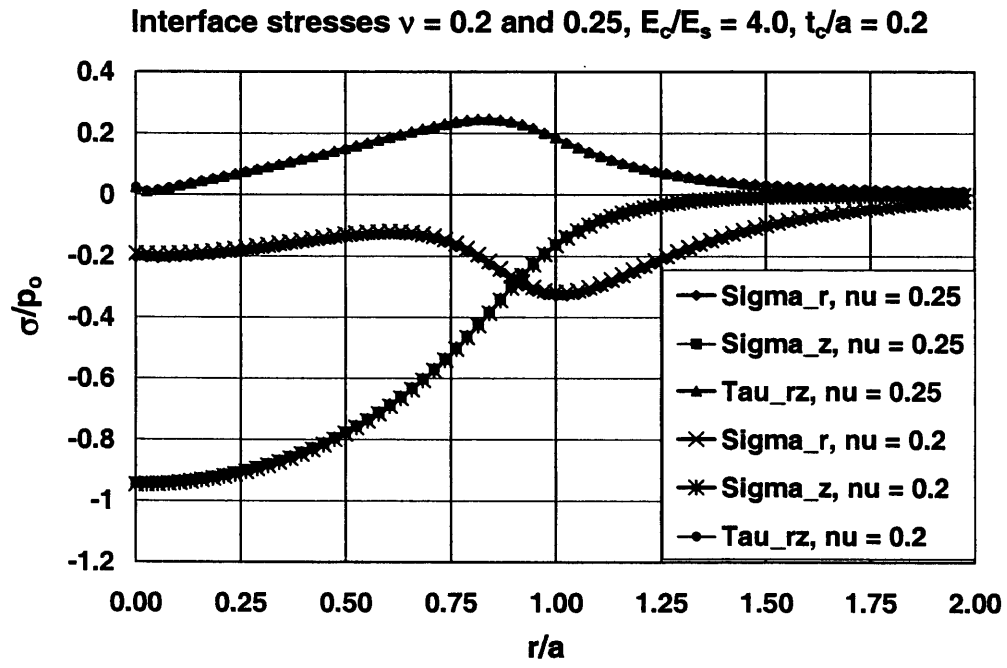

Figure 6.2: Interface stresses for Poisson ratios *ν* = 0.2 and 0.25

6.5.2 Stresses and locations of interest

In the present study, we are interested in understanding behavior of specific stresses at specific locations, which are important with respect to failure of the coating. These are listed below:

- Coating surface – tensile stresses σ_r, at the edge of contact leading to surface cracks.
- Interface – tensile stress σ_r and shear stress τ_{rz}, leading to cracks and delamination.
- In-plane (parallel to interface) compressive stresses σ_r and σ_θ, may lead to buckling of the coating. Buckling of coating is more likely towards the edge of the contact where normal stress σ_z, is small compared to in-plane stresses. This is illustrated in Figure 6.3.

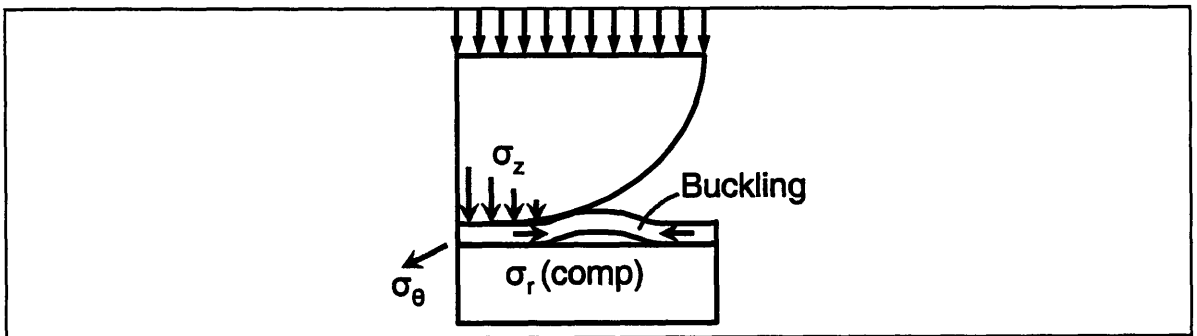

Figure 6.3: Thin film buckling due to in-plane compressive stresses σ_r and σ_θ

6.6 Stresses in monolayer configuration (single coating layer)

6.6.1 Surface stresses

Figure 6.4 shows the radial tensile stress σ_r, at contact edge ($r = a$) on the coating surface.

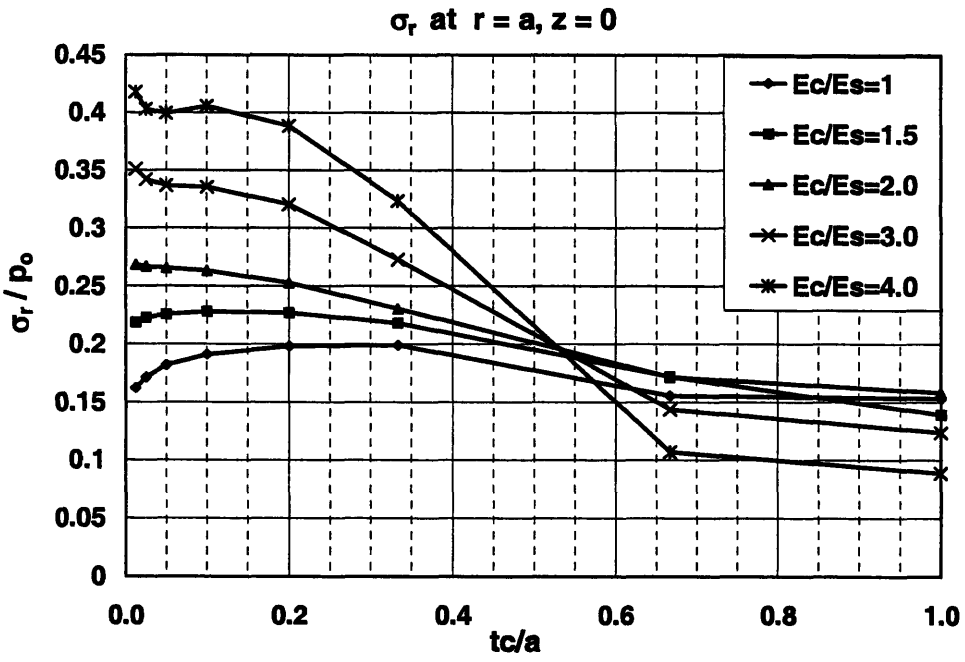

Figure 6.4: Radial tensile stress σ_r at edge ($r = a$) of coating surface ($z = 0$)

For thin coatings, these stresses may lead to formation of surface cracks that could extend through the coating thickness and may thereafter continue into the substrate or along the interface depending on relative fracture strengths [34]. As the coating thickness $t_c \rightarrow 0$, the in-plane radial stresses, σ_r, on the coating surface do not tend towards stresses corresponding to no-coating configuration. This behavior for thickness ratios less than 0.1 is substantially different from that suggested in [14]. The reason for this behavior is that in-plane stress, σ_r, is not continuous across the interface and can have substantially different values from the no coating configuration where the stresses correspond to stresses in the substrate.

Figure 6.5 shows in-plane stresses, σ_r and σ_θ, at the center of the contact on the coating surface. For $\frac{t_c}{a} < 0.1$, these become more compressive with decreasing thickness particularly for high modulus ratios, e.g. larger than 2. This is not captured by previous analysis in [14] with the difference in results being up to 40%. The behavior of stresses for $\frac{t_c}{a} > 0.1$, in the present analysis, match to within 1-6% the results found in [14].

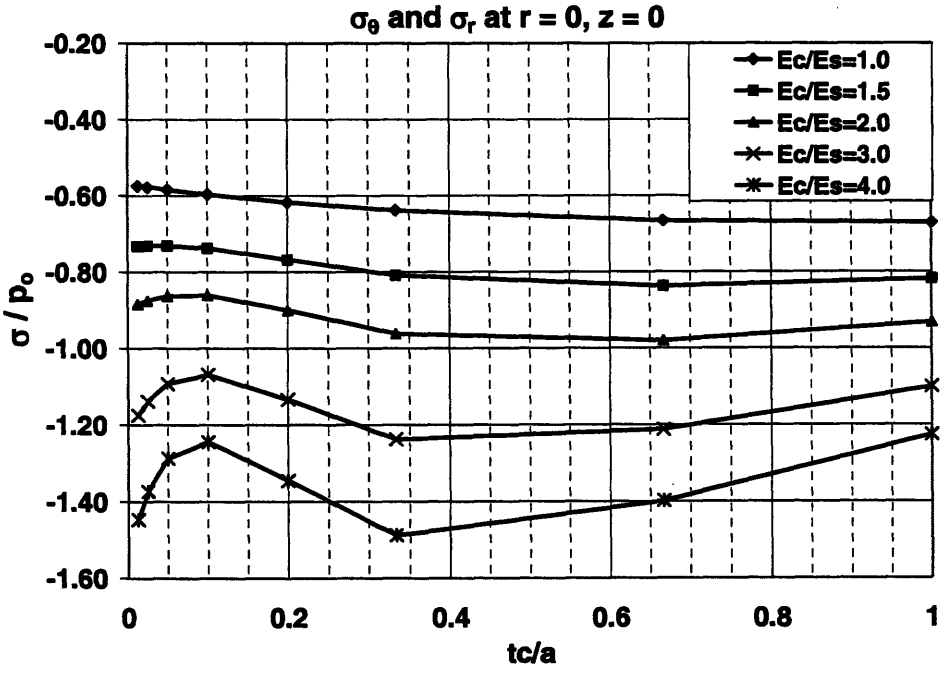

Figure 6.5: In-plane stresses at the coating surface and near center of contact

Figure 6.6 shows the normal contact stress σ_z, at the coating surface. The contact pressure, σ_z, at the coating surface has to be continuous and as expected approaches value corresponding to no-coating configuration, as the layer is made thinner.

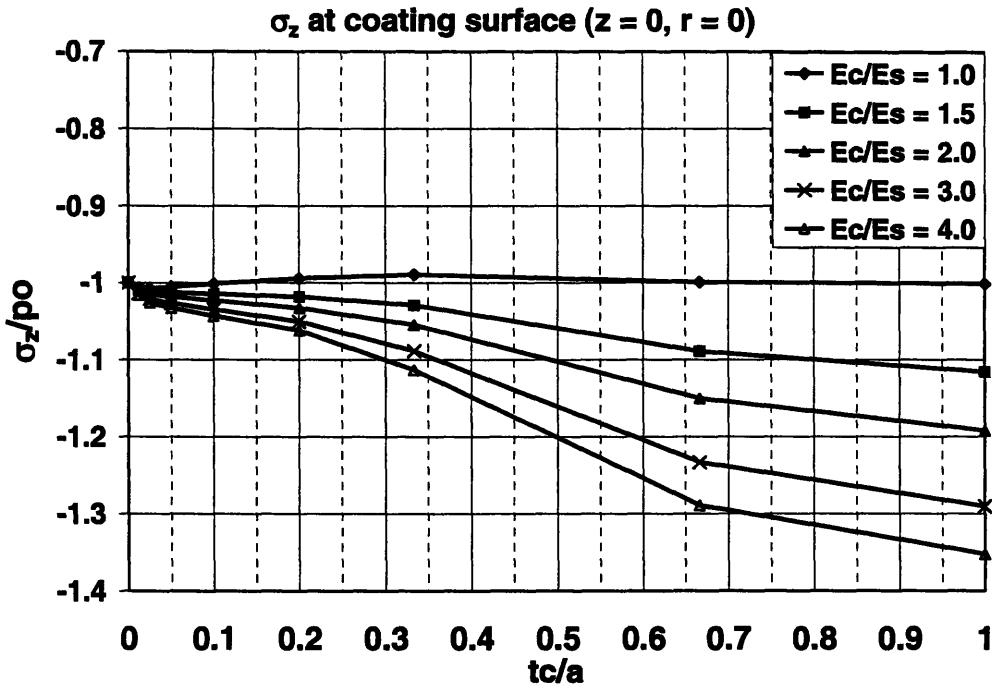

Figure 6.6: Normal stress (σ_z) at center of contact ($r = 0$) on the coating surface

6.6.2 Coating-substrate interface stresses

Figure 6.7 shows the in-plane stresses, σ_r and σ_θ, at the center of the contact, $r = 0$, in the coating and at the interface. For thin coatings, $\frac{t_c}{a} < 0.1$, these stresses become rapidly compressive with decreasing thickness and increasing modulus ratios. For larger thicknesses $\left(\frac{t_c}{a} > 0.3\right)$, the in-plane stresses become tensile which may lead to initiation and growth of interface cracks.

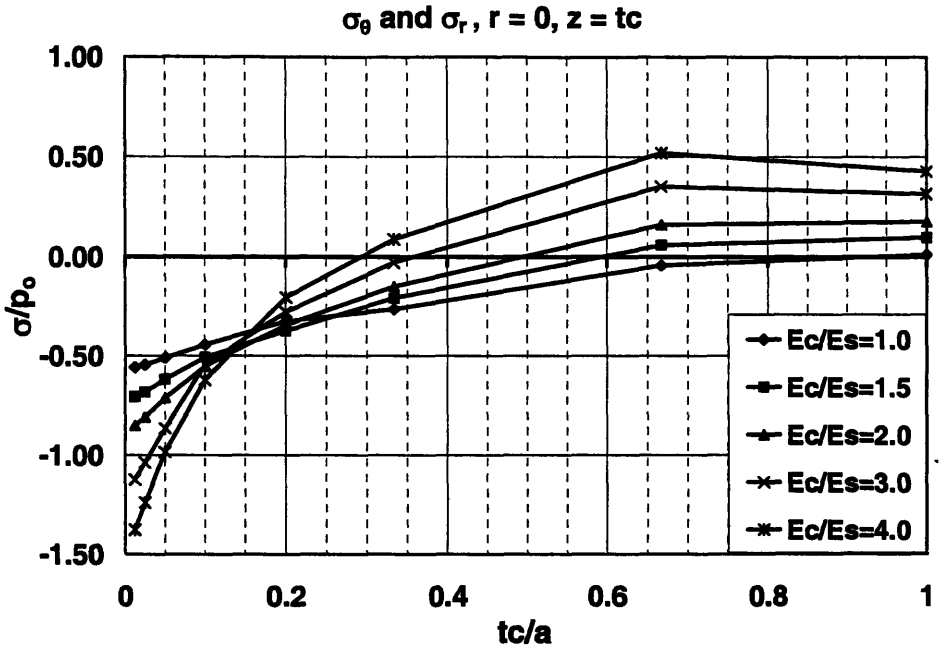

Figure 6.7: In-plane stresses σ_r and σ_θ at the interface, in the coating

Figure 6.8 shows in-plane stresses, σ_r and σ_θ, at the interface and at center of the contact, r = 0, in the substrate.

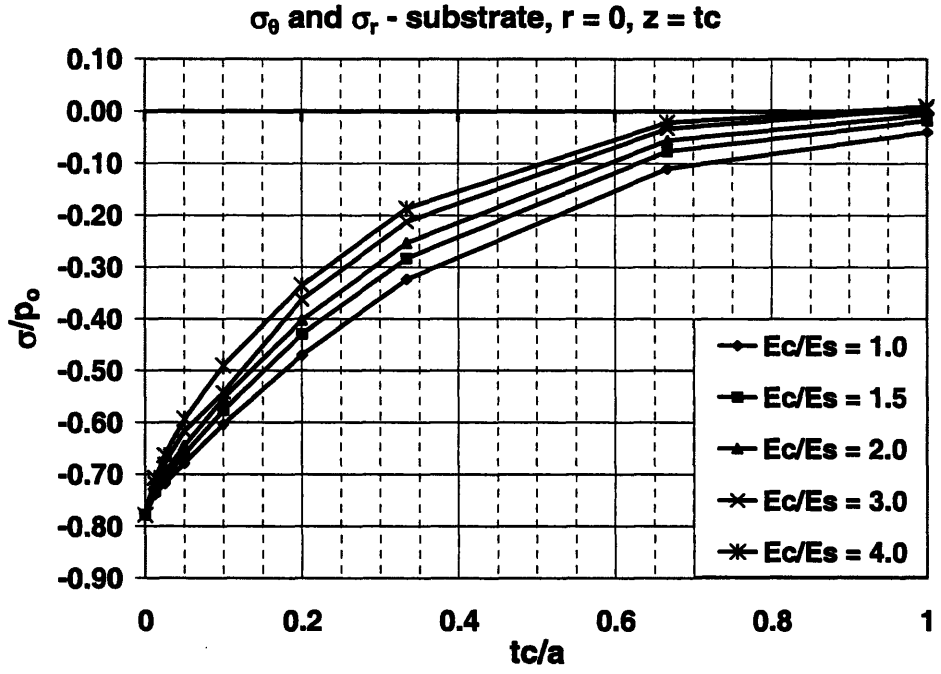

Figure 6.8: In-plane stresses σ_r and σ_θ at the interface, in the substrate

These in-plane stresses remain compressive and as the coating thickness $t_c \rightarrow 0$, the stresses tend towards values corresponding to no-coating configuration (σ_r, $\sigma_\theta = 0.78\ p_o$ for no-coating and σ_r, $\sigma_\theta = 0.73\ p_o$ for $\frac{t_c}{a} = 0.0125$). This trend is in agreement with that in [13] and is expected since the effect of coating on the substrate diminishes, as the coating layer is made thinner. In-plane stresses within the coating itself are influenced by the substrate and need not be continuous across the interface. Therefore, the behavior of in-plane stresses in the coating can be substantially different from those in the substrate.

Figure 6.9 shows the maximum tensile stress along the coating-substrate interface. For coatings with thickness ratios < 0.2 the maximum stresses occur towards the edge of the contact. For thicker coatings $\left(\frac{t_c}{a} > 0.2\right)$, this occurs at the center of contact, implying a large portion of the interface is under tensile stresses, which may facilitate interfacial crack growth.

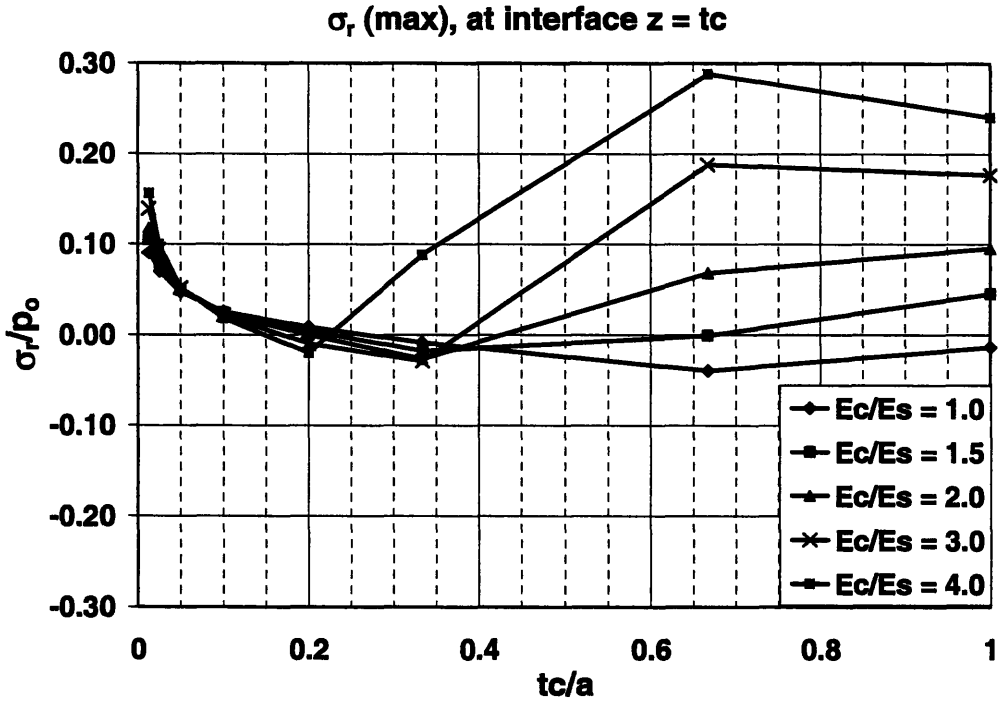

Figure 6.9: Maximum tensile stress along interface ($z = tc$)

Figure 6.10 compares shear stress along interface for coatings with thickness ratios = 0.1 and 1.0.

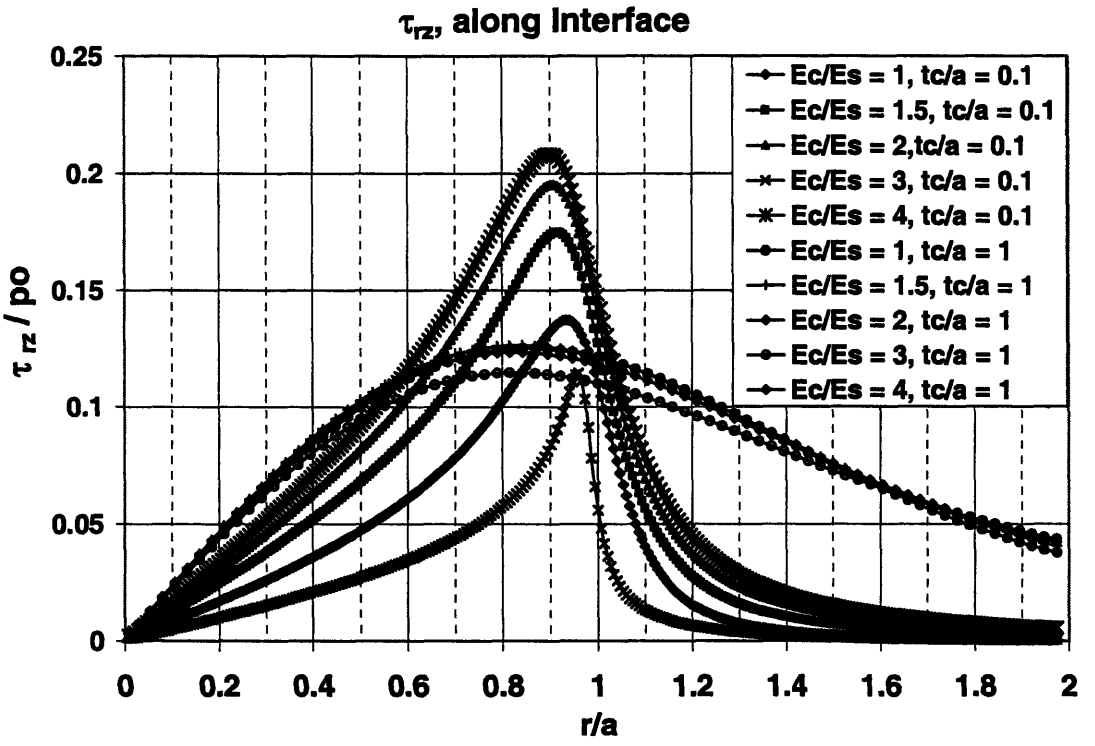

Figure 6.10: Shear stress along the interface for *tc/a* = 0.1 and 1.0

Figure 6.11 compares shear stresses along interface for coatings with thickness ratios 0.025 and 1.0. As may be seen from the plots shown in Figure 6.10 and Figure 6.11, the shear stress attains a maximum near the edge of contact, $r = a$.

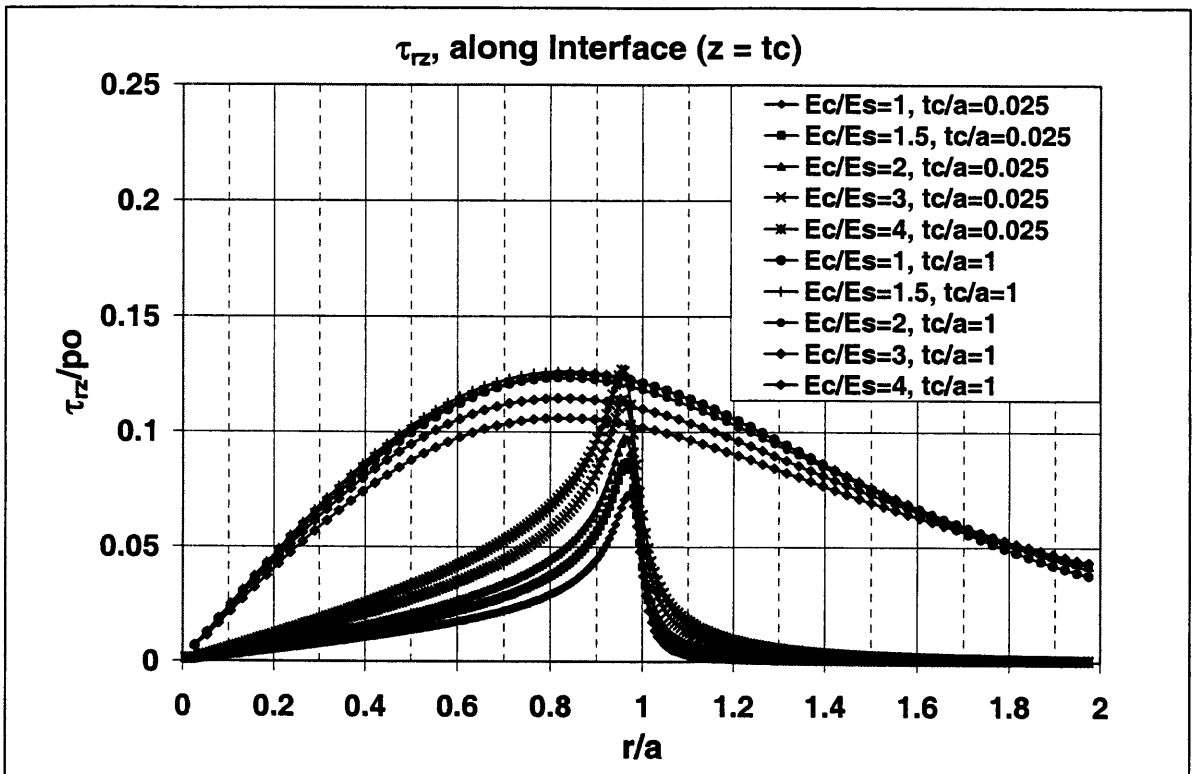

Figure 6.11: Shear stress (τ_{rz}) along interface for *tc/a* = 0.025 and 1.0

Figure 6.12 shows maximum shear stress, τ_{rz}, along the interface for different thickness and modulus ratios. The maximum stresses occur around $\frac{t_c}{a} = 0.2 - 0.3$. For lower $\frac{t_c}{a}$, shear stress decreases with decreasing thickness and in the limiting case goes towards zero. This is expected since shear stress has to be continuous across the interface and has zero value at the free surface.

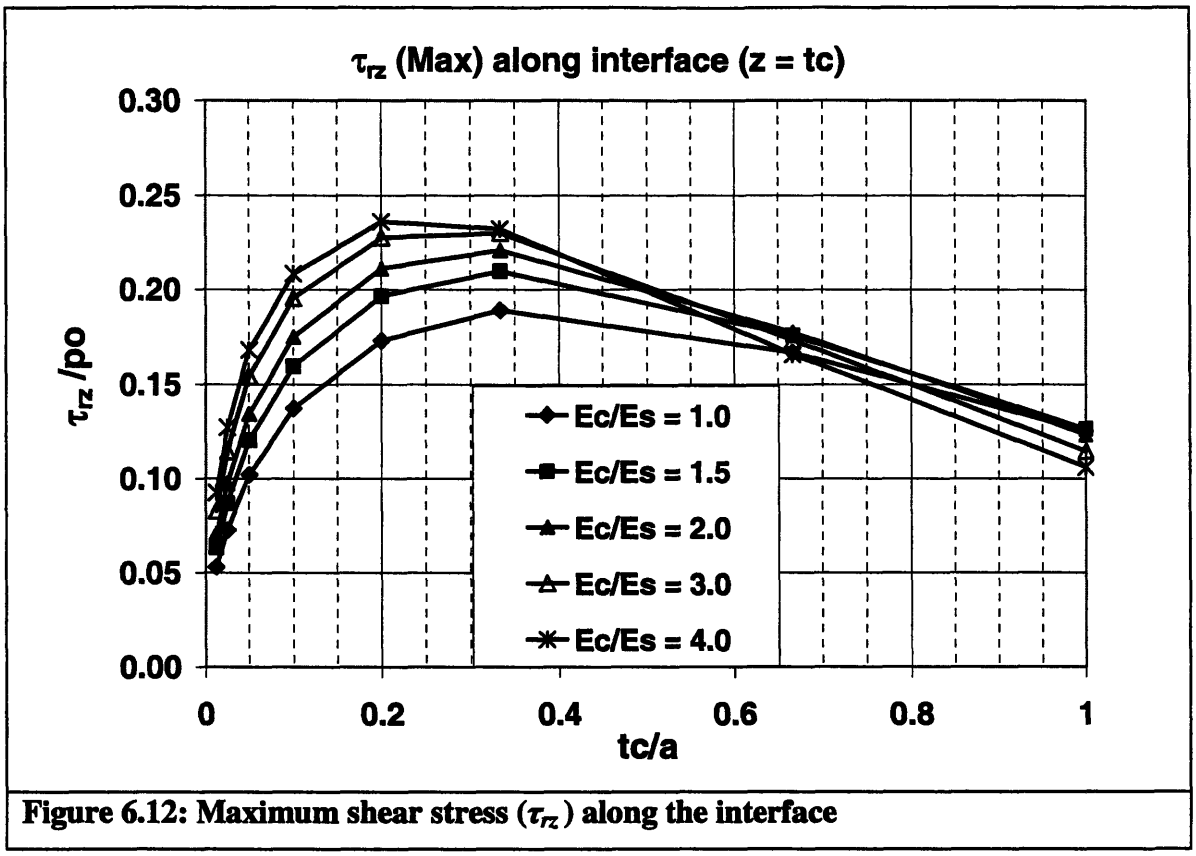

Figure 6.12: Maximum shear stress (τ_{rz}) along the interface

6.6.3 Design guide

The stresses within the coating and along the coating-substrate interface are complex functions of thickness and modulus ratios and hence the difficulty in determining an optimal choice of parameters that would minimize the probability of coating failure. However, the choice is much simpler for a limited set of coatings. In the applications that have been chosen for this study, these are thin coatings with thickness ratios < 0.1. Previous work [14] dealing with parametric study of stresses in coatings did not cover this group which is important for several applications including kinematic couplings.

Based on the observed variation in stresses in the coating and at the coating-substrate interface, guidelines are provided for the selection of coating parameters (thickness and modulus ratio) to minimize tensile, shear stresses and in-plane compressive stresses within the coating and at the interface.

Figure 6.13 shows the tensile stresses, σ_r, on coating surface for $\frac{t_c}{a} \leq 0.1$. These stresses are nearly independent of coating thickness for thickness ratios less than 0.1, with less than 4.5% variation. However, stresses increase with increasing modulus ratio.

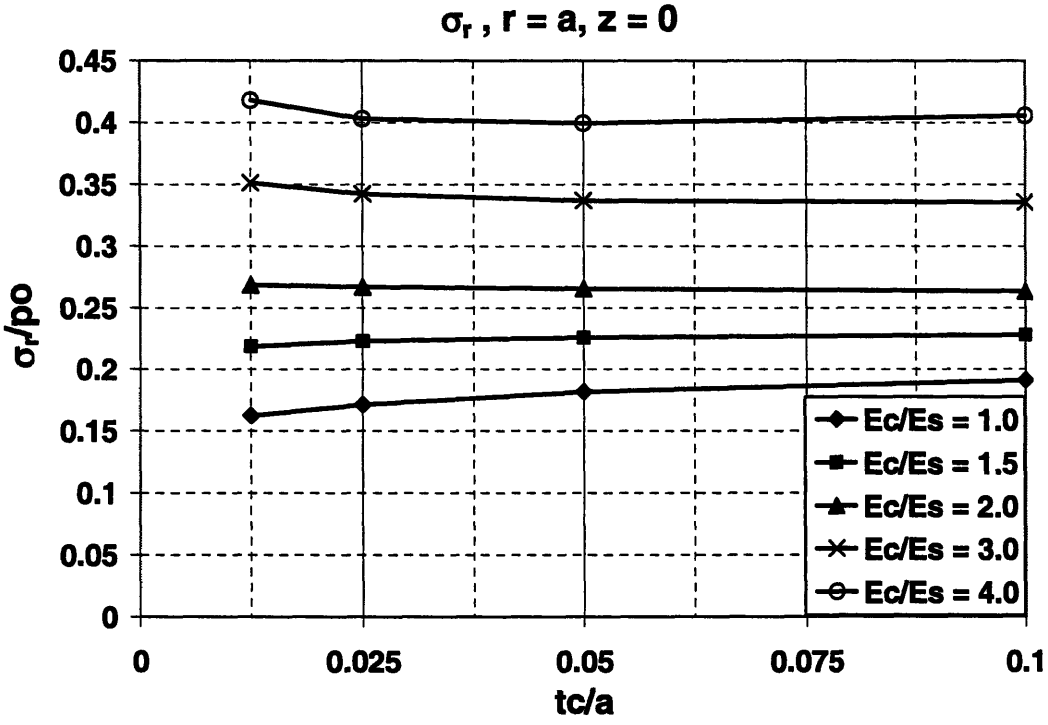

Figure 6.13: Tensile stress, σ_r, on coating surface (z =0) at the edge of contact ($r = a$)

Figure 6.14 shows maximum tensile stress, σ_r, at the coating-substrate interface, in the coating. For thickness ratios ranging from 0.05 – 0.1, tensile stresses at the interface are nearly independent of modulus ratio with less than 9% variation. In addition, variation and the magnitude of the stresses are small in this region. For thickness ratios less than 0.05, stresses increase rapidly with decreasing thickness and increasing modulus ratio.

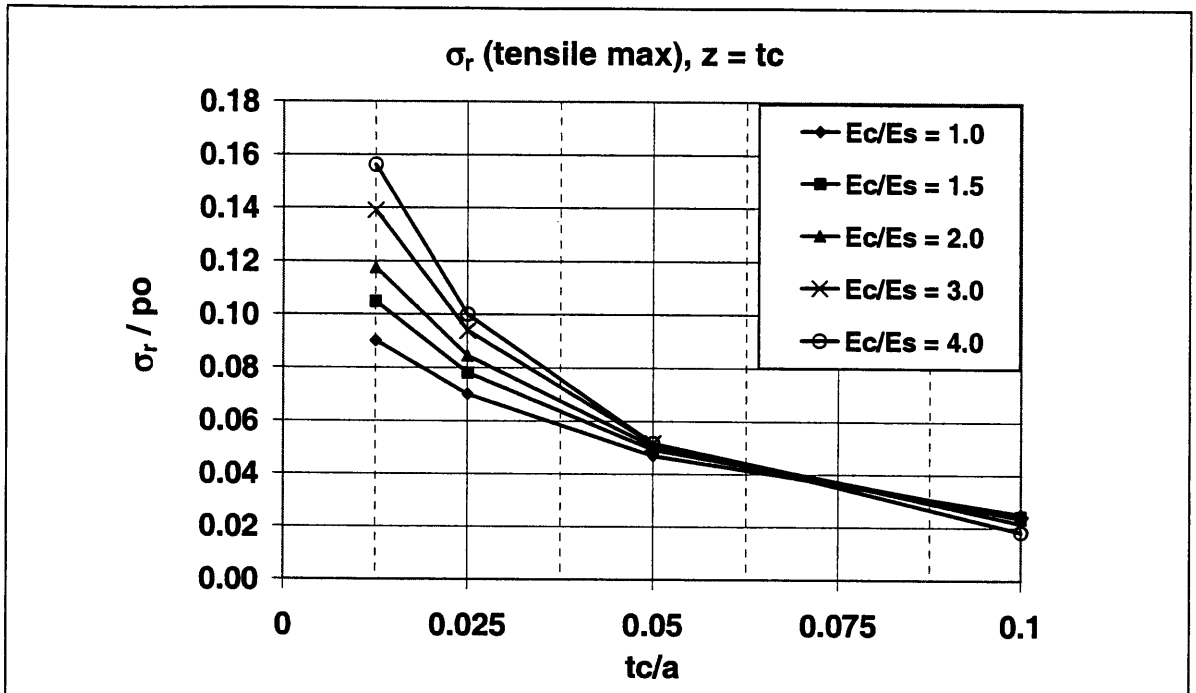

Figure 6.14: Maximum tensile stress, σ_r, along the coating-substrate interface

Figure 6.15 shows the maximum shear stress along the coating-substrate interface.

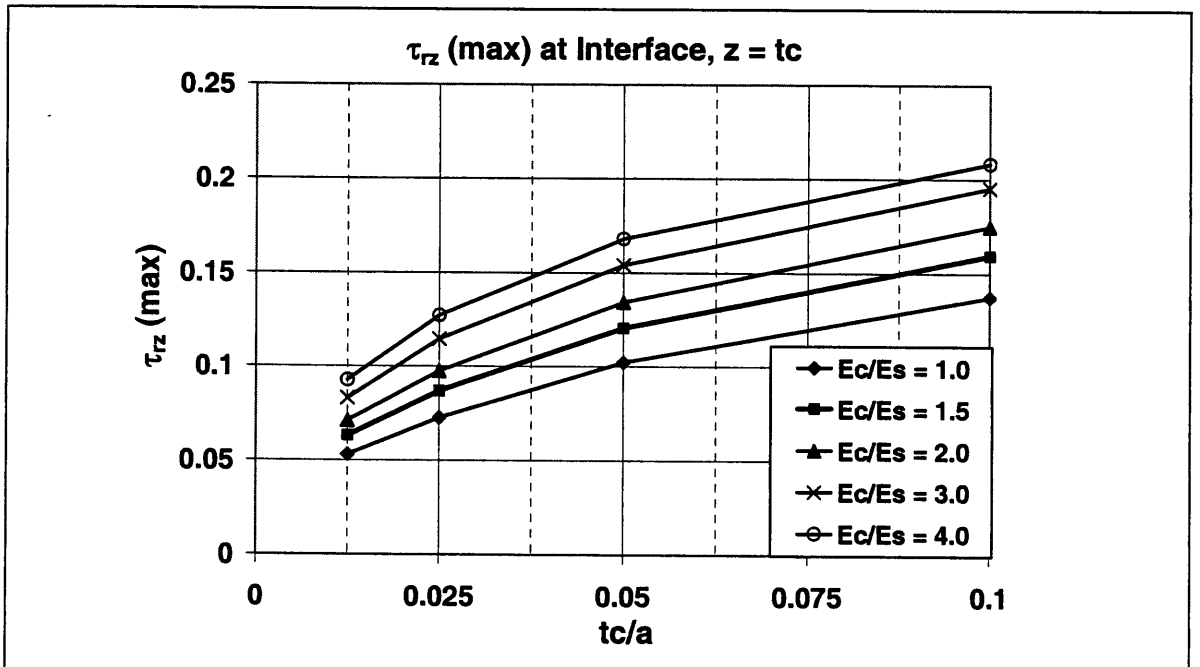

Figure 6.15: Maximum shear stress, τ_{rz}, at the interface

The maximum shear stress shows a gradual decrease with decreasing thickness and has a higher magnitude for larger modulus ratios. These stresses arise due to a combination of

1. Bending stresses resulting from difference in modulus of the coating and substrate
2. Relative flow of material due to difference in Poisson's ratio of coating and substrate

With decreasing coating thickness, the effect of coating material on substrate decreases and the shear stresses, being continuous across interface, tend towards value corresponding to stresses at the surface. In this case, zero.

Figure 6.16 shows the in-plane compressive stresses at the center (r = 0) of the coating-substrate interface, in the coating. These stresses could lead to buckling of the coating especially towards the edge of the contact where the normal stress, σ_z, is small.

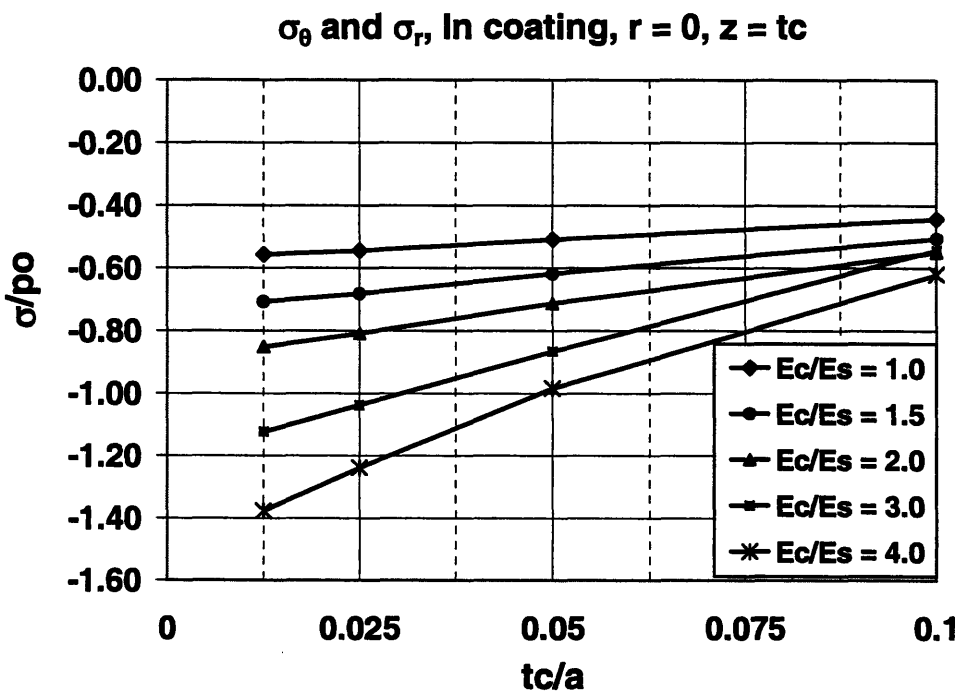

Figure 6.16: In-plane compressive stress σ_r and σ_θ in the coating at $r = 0$

Thus in summary, to minimize

1. Tensile stresses at the surface – keep modulus ratio small $\frac{Ec}{Es} \downarrow$.
2. Tensile stresses at the interface – keep modulus ratio small $\frac{Ec}{Es} \downarrow$ and thickness ratio high $\frac{t}{a} \uparrow$.
3. Shear stresses at the interface – keep modulus ratio $\frac{Ec}{Es} \downarrow$ and thickness ratio $\frac{t}{a} \downarrow$ small.
4. In-plane compressive stresses – keep modulus ratio $\frac{Ec}{Es} \downarrow$small and thickness ratio $\frac{t}{a} \uparrow$ large.

Looking at the above factors, we find that reduction of shear stress requires smaller thickness ratio whereas reduction of in-plane compressive and tensile interfacial stresses entails larger thickness ratios. As a result, there is a degree of conflict. However if the designer knows the upper limit on the interface shear strength, then the optimal configuration is automatically determined.

To develop an analytical framework from the observations, a relationship of the form of Equation 6.1 is determined.

$$\sigma = K_1\left(\frac{t}{a}\right)^p\left(\frac{E_c}{E_s}\right)^q + K_2\left(\frac{t}{a}\right)^r\left(\frac{E_c}{E_s}\right)^s \qquad \textbf{(6.1)}$$

This form was fitted to the FEA simulations using least square method. More complex functions may be chosen, but for the purposes of characterizing dependence of stresses on coating parameters, Equation 6.1 suffices. The error between the least square fit and the simulation data is less than 6%. Table 6.3 lists the coefficients and exponents corresponding to Equation 6.1, for different stresses. Knowing the failure strengths of the

coating and the interface, the designer may use the analytical expression given by Equation 6.1 to select an appropriate set of coating parameters.

Table 6.3: Analytic expression for stress in monolayer configuration

	K_1	p	q	K_2	r	s	Standard Deviation (% error)	Error (%)
σ_r (max) Surface	0.1365	-0.040	0.671	0.220	0.735	-0.473	1.760	-5.83 to1.86
σ_r (max) Interface	0.128	-0.178	0.563	-0.146	-0.056	0.640	5.0	-5.9 to 5.54
τ_{rz} (max) Interface	0.451	-0.175	0.486	0.438	1.275	1.372	0.756	-1.69 to 1.24
σ_r and σ_θ Interface	-1.996	0.168	0.797	2.343	0.397	0.949	3.033	-2.10 to 5.87

6.7 Hard Interlayer

From the simulation results in previous section, we observe that increasing modulus ratio corresponds to increased stresses in the coating. One possible way to reduce stresses is to use an interlayer between coating and substrate to minimize the modulus gradient. Analysis on interlayer models has been done by Djabella and Arnell [15]. Their analysis is again limited to coatings with $\frac{t_c}{a} > 0.1$. In the present analysis, the interlayer was assigned a modulus ratio equal to average of ratios for substrate and coating

$\left(E_{\text{int}} = \frac{E_s + E_c}{2}\right)$ and the interlayer thickness was kept equal to that of the coating. Subsequent plots correspond to $t_c = \left(\frac{t_{coat} + t_{\text{int}}}{a}\right)$, and they are compared with stresses in a monolayer for coating thickness $t_c = \frac{t_{coat}}{a}$. As in the study of monolayer configuration, the parameters varied were thickness and modulus ratios. Figure 6.17 shows a schematic of the finite element model.

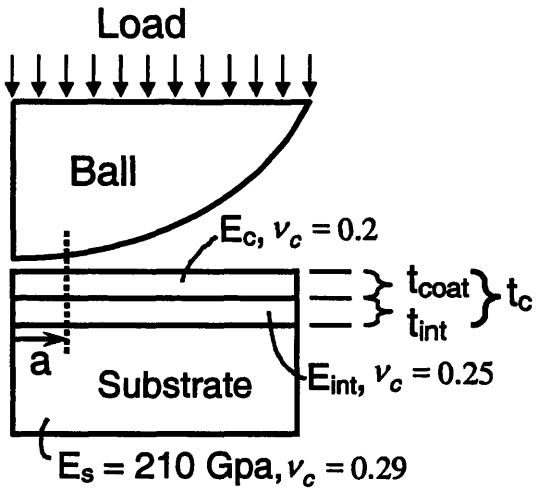

Figure 6.17: Schematic of finite element model for interlayer analysis

Figure 6.18 compares tensile radial stresses, σ_r, on the coating surface for configuration with the interlayer and with monolayer coating.

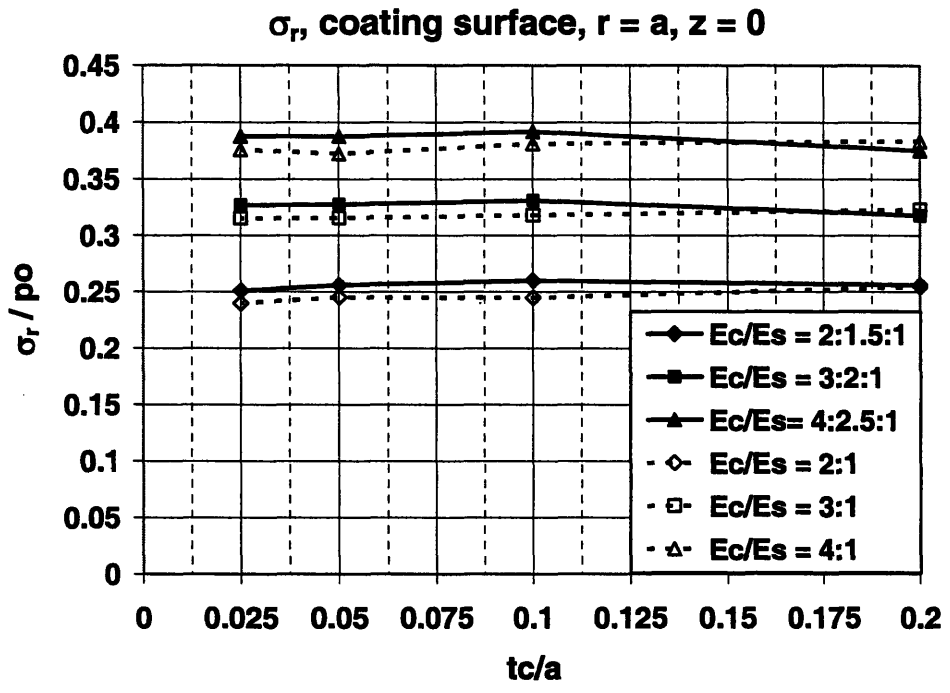

Figure 6.18: Radial stress σ_r on the coating surface at the edge of contact ($r = a$)

Use of interlayer does not reduce the surface tensile stresses for thin coatings $\left(\frac{t_c}{a} < 0.1\right)$.

In fact, the interlayer configuration has 2-4% higher stresses.

Figure 6.19 shows a comparison between radial tensile stresses at the coating-interlayer and monolayer-substrate interfaces. In these tests, the tensile stresses at the coating-interlayer are approximately 20% higher than stresses at the coating-substrate interface of a monolayer.

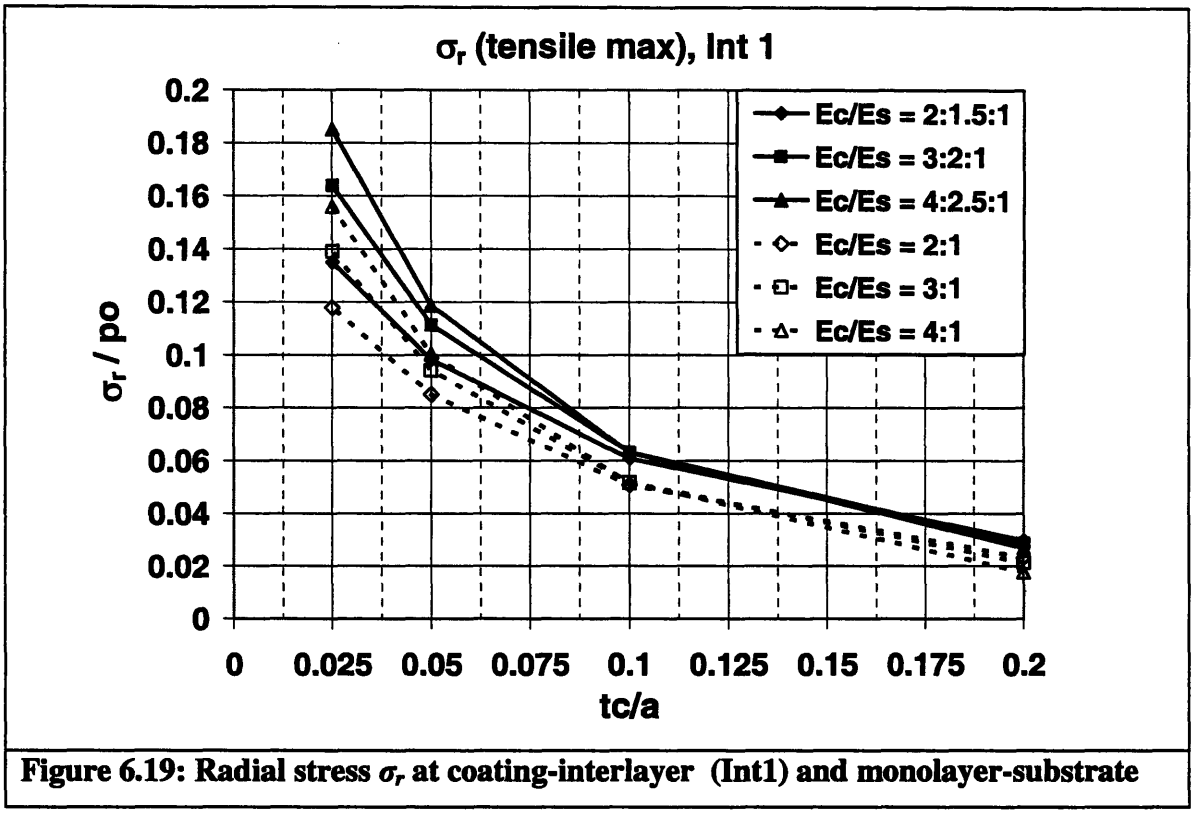

Figure 6.19: Radial stress σ_r at coating-interlayer (Int1) and monolayer-substrate

Figure 6.20 shows a comparison between radial tensile stresses at the interlayer-substrate and monolayer-substrate interfaces. The tensile stresses at the interlayer-substrate interface are 50 - 60 % lower than stresses at the monolayer-substrate interface.

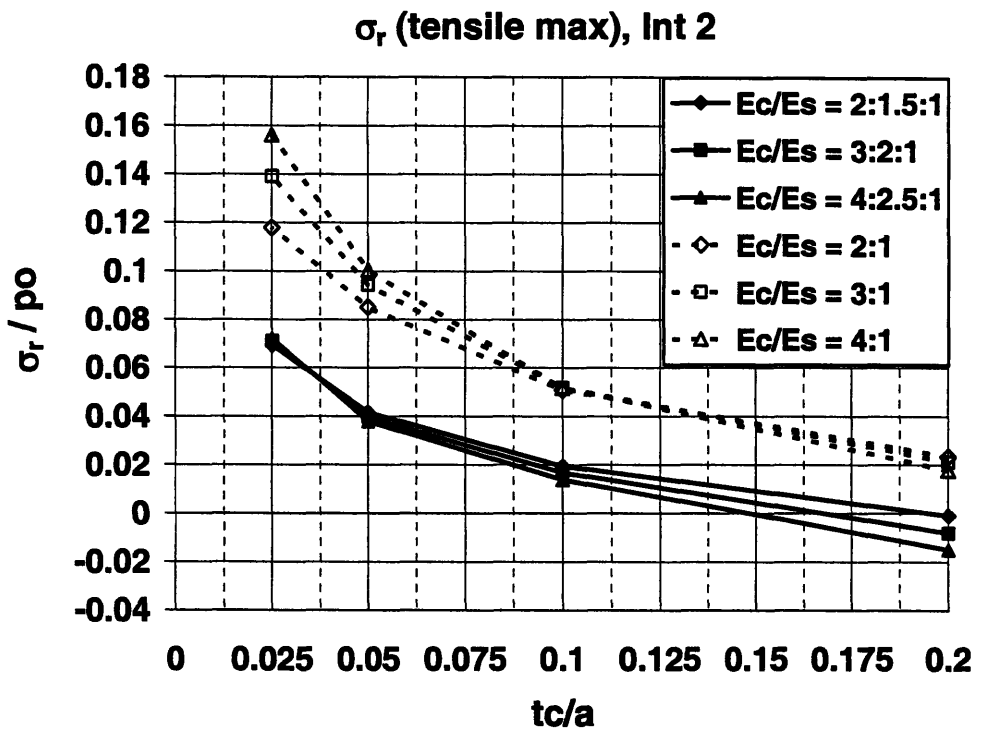

Figure 6.20: Radial stress σ_r at interlayer-substrate (Int2) and monolayer-substrate

Figure 6.21 shows the shear stresses at the coating-interlayer and monolayer-substrate interfaces.

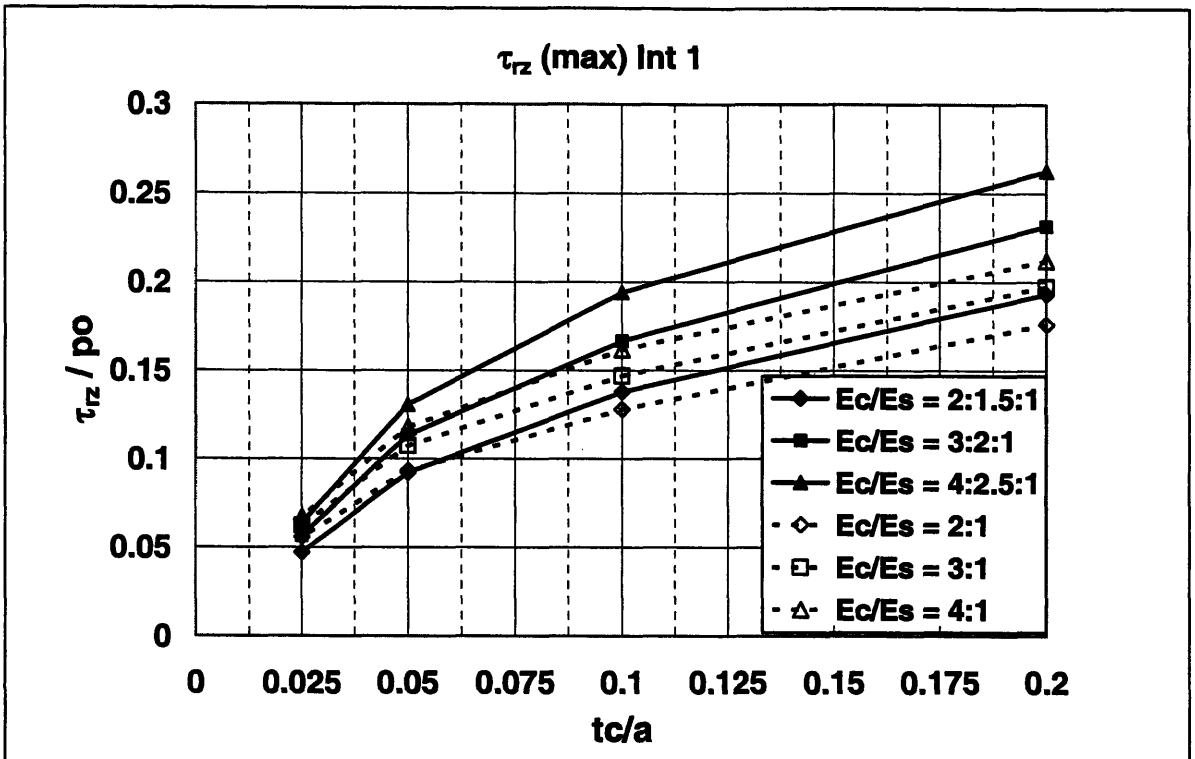

Figure 6.21: τ_{rz} along coating-interlayer (Int1) and monolayer-substrate interface

Figure 6.22 show the shear stresses at the coating-interlayer and interlayer-substrate interfaces. Shear stresses at coating-interlayer and interlayer-substrate interfaces are approximately 20-30% higher than stresses at a monolayer-substrate interface.

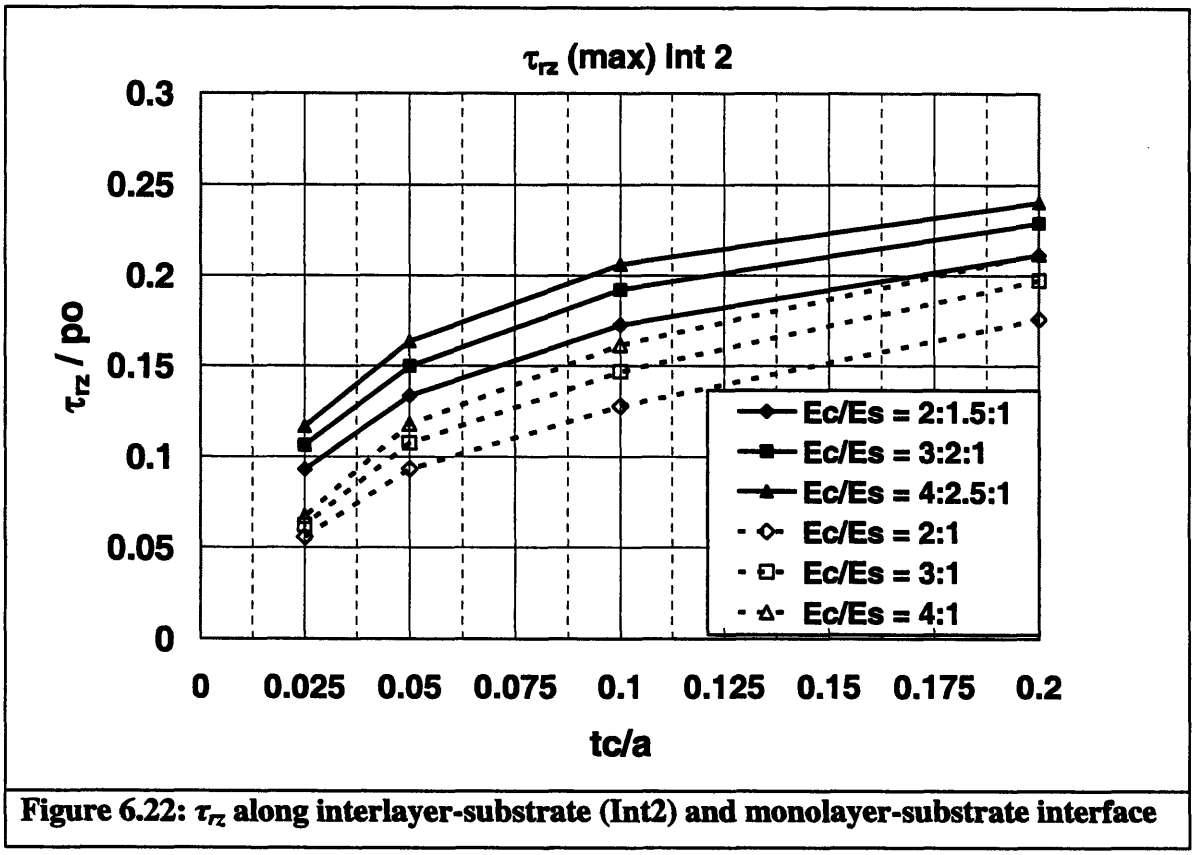

Figure 6.22: τ_{rz} along interlayer-substrate (Int2) and monolayer-substrate interface

Figure 6.23 shows the in-plane compressive stresses, σ_r and σ_θ, at the coating-interlayer and the monolayer-substrate interfaces. The stresses in the coating are only affected by approximately 3-5% due to the presence of the interlayer.

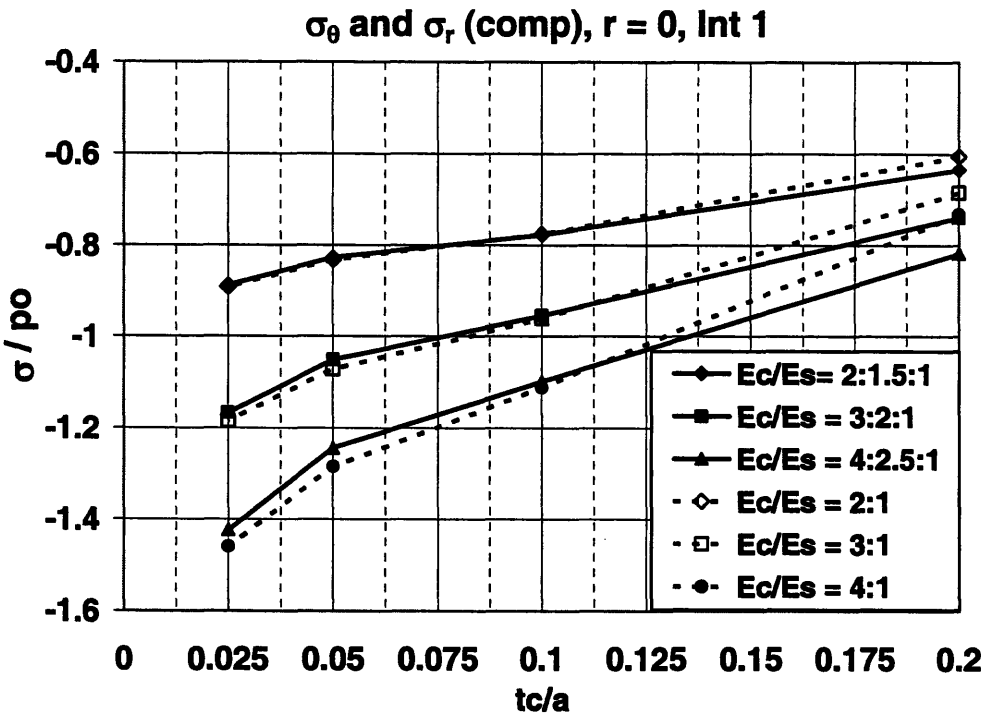

Figure 6.23: σ_r and σ_θ in coating-interlayer (Int1) and monolayer-substrate interface

Figure 6.24 shows the in-plane compressive stresses, σ_r and σ_θ, at the interlayer-substrate and the monolayer-substrate interfaces. In-plane compressive stresses within the interlayer are approximately 40-50 % smaller than those in the monolayer.

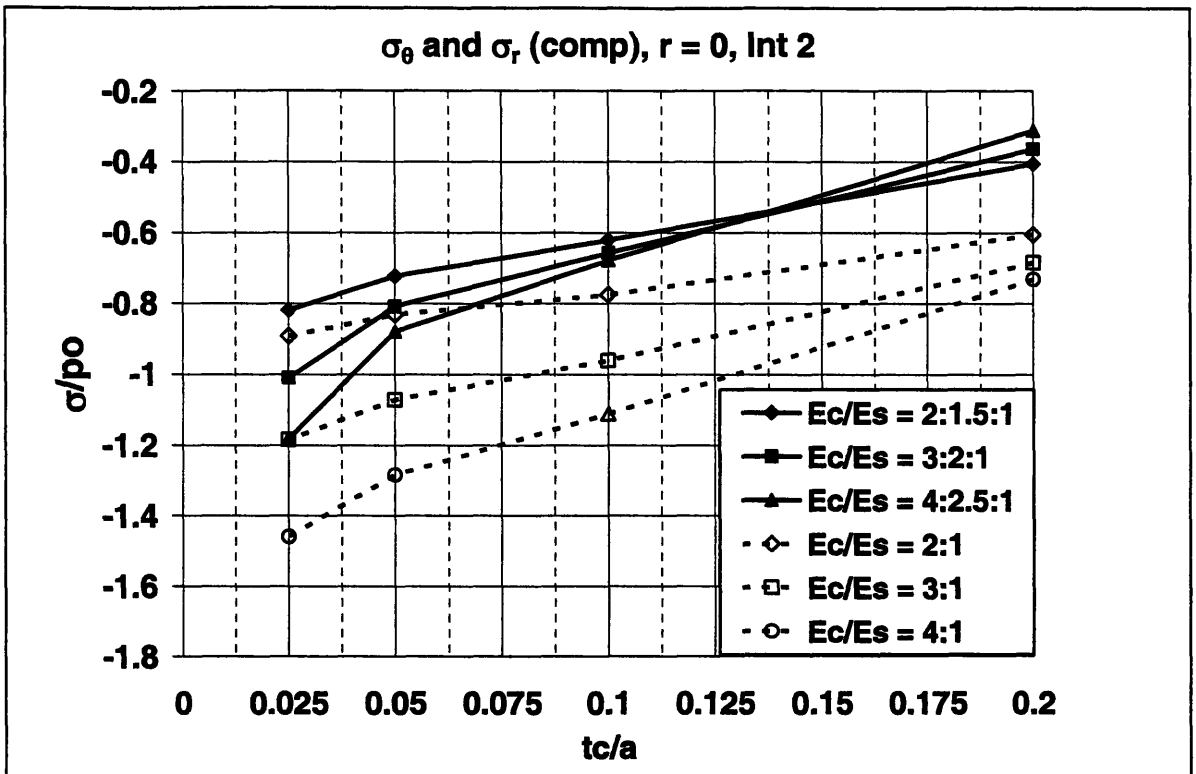

Figure 6.24: σ_r and σ_θ in interlayer-substrate (Int2) & monolayer-substrate interface

Table 6.4 summarizes the effects of using a hard interlayer between the coating and the substrate.

Table 6.4: Hard interlayer stresses compared to monolayer stresses

	σ_r (coating surface)	σ_r (coating-interlayer)	σ_r (interlayer-substrate)	τ_{rz} (coating-interlayer, interlayer-substrate)	σ_r and σ_θ (In-plane compressive stresses-coating)	σ_r and σ_θ (In-plane compressive stresses-interlayer)
% Difference	2-4% higher	20% higher	50-60% lower	20-30% higher	3-5% deviation	40-50% lower

Overall, the results suggest that use of a hard interlayer for thin coatings $\left(\frac{t_c}{a} < 0.1\right)$ does

not provide significant advantages. However, use of hard interlayer would be desirable if the coating-interlayer and interlayer-substrate pairs have better adhesion than just a monolayer of the coating material. Assessing the improvement for such a case is beyond the scope of this work.

Table 6.5 lists the coefficients and exponents corresponding to Equation 6.1 used to characterize the stresses. Since interlayer modulus is kept equal to average of coating and substrate modulus, it does not appear explicitly in the expression.

Table 6.5: Analytic expression for stress in hard interlayer configuration

	K_1	p	q	K_2	r	s	Standard Deviation (% error)	Error Range (%)
σ_r(max) Surface	0.193	0.015	0.819	-0.573	3.331	2.424	0.793	-1.59 to 1.34
σ_r (max) Int1	-0.142	-0.119	1.020	0.140	-0.230	0.898	4.431	-6.43 to 3.41
σ_r (max) Int2	0.0054	-0.689	0.082	-0.065	1.095	1.187	2.359	-3.41 to 4.46
τ_{rz} (max) Int1	0.450	0.125	0.607	-0.199	-0.061	0.595	1.562	-3.09 to 2.08
τ_{rz} (max) Int2	0.500	0.0098	0.163	-0.242	-0.142	0.083	0.779	-0.98 to 1.33
σ_r, σ_θ Int1	-0.495	-0.068	0.923	0.287	0.875	2.081	1.60	-2.42 to 3.02
σ_r, σ_θ Int1	-1.039	0.0183	0.951	0.985	0.281	1.323	3.787	-5.79 to 5.94

6.8 Soft Interlayer

In this section, possible benefits of using a soft interlayer between the coating and the substrate $\left(E_{\text{int}} = \frac{E_s}{2}\right)$ are explored. The interlayer thickness was held to be equal to thickness of coating. In Figure 6.25, tensile stresses σ_r, on the surface of a monolayer is compared to a configuration with a soft interlayer. Use of soft interlayer does not help in terms of reducing the surface tensile stresses for thin coatings $\left(\frac{t_c}{a} < 0.1\right)$. These stresses are approximately 10-15% higher than in the monolayer and hard interlayer configurations.

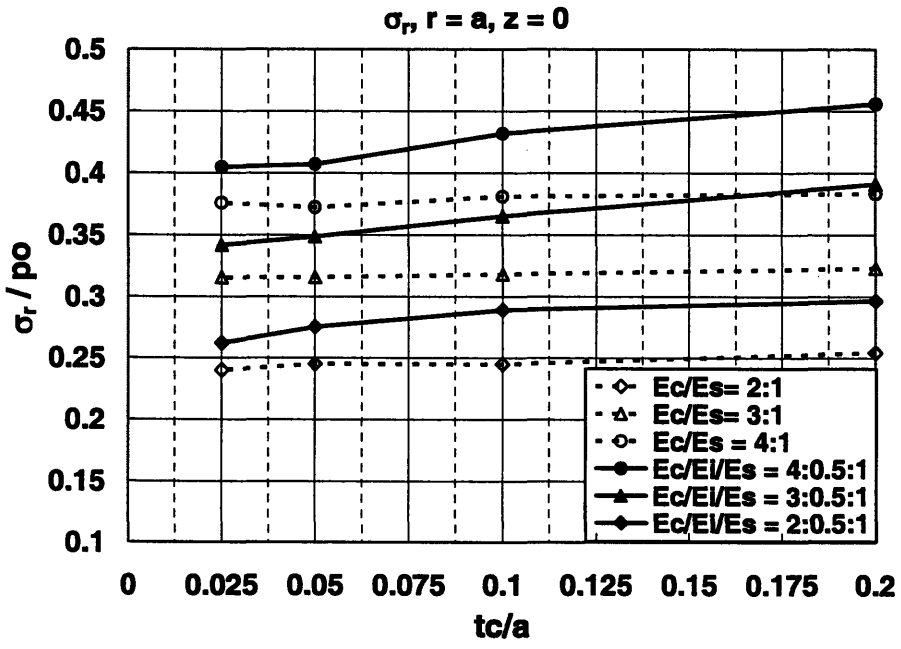

Figure 6.25: Tensile stress, σ_r, on the coating surface at the edge of contact ($r = a$)

Figure 6.26 shows the radial tensile stress, σ_r, at the coating-interlayer and the monolayer-substrate interfaces. The tensile stresses at the coating-interlayer interface are approximately 5% lower than at monolayer-substrate interface.

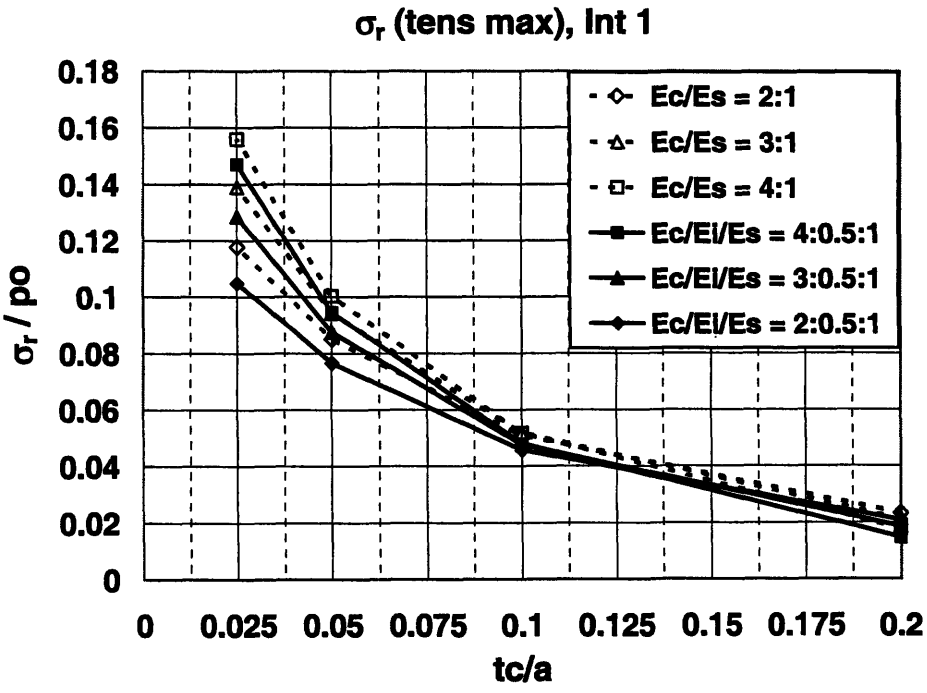

Figure 6.26: Tensile stress, σ_r, at coating-interlayer and monolayer-substrate interface

Figure 6.27 shows the radial tensile stress, σ_r, at the interlayer-substrate and the monolayer-substrate interfaces. The tensile stresses at the interlayer-substrate interface are approximately 80% lower than at interface of a monolayer.

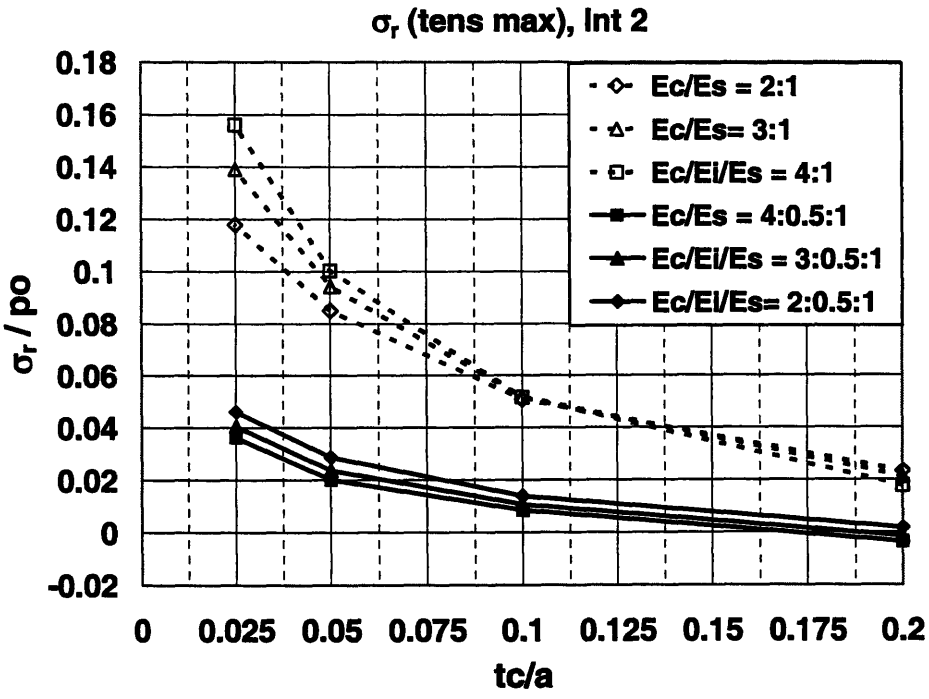

Figure 6.27: Tensile stress, σ_r, at interlayer-substrate & monolayer-substrate interface

Figure 6.28 shows the maximum shear stress at the coating-interlayer and monolayer-substrate interfaces.

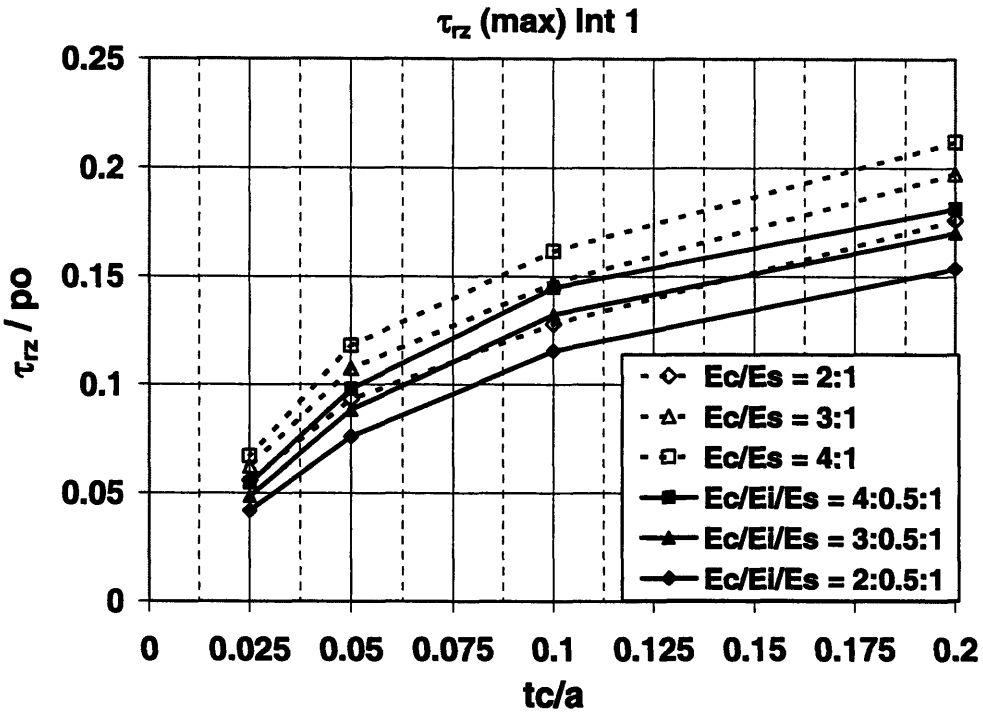

Figure 6.28: Shear stress τ_{rz} along the coating-interlayer & monolayer-substrate

Figure 6.29 shows the maximum shear stress at the interlayer-substrate and monolayer-substrate interfaces. Shear stresses at coating-interlayer interface are approximately 15% lower and interlayer-substrate interface are approximately 5-15% higher, than stresses at interface of a monolayer.

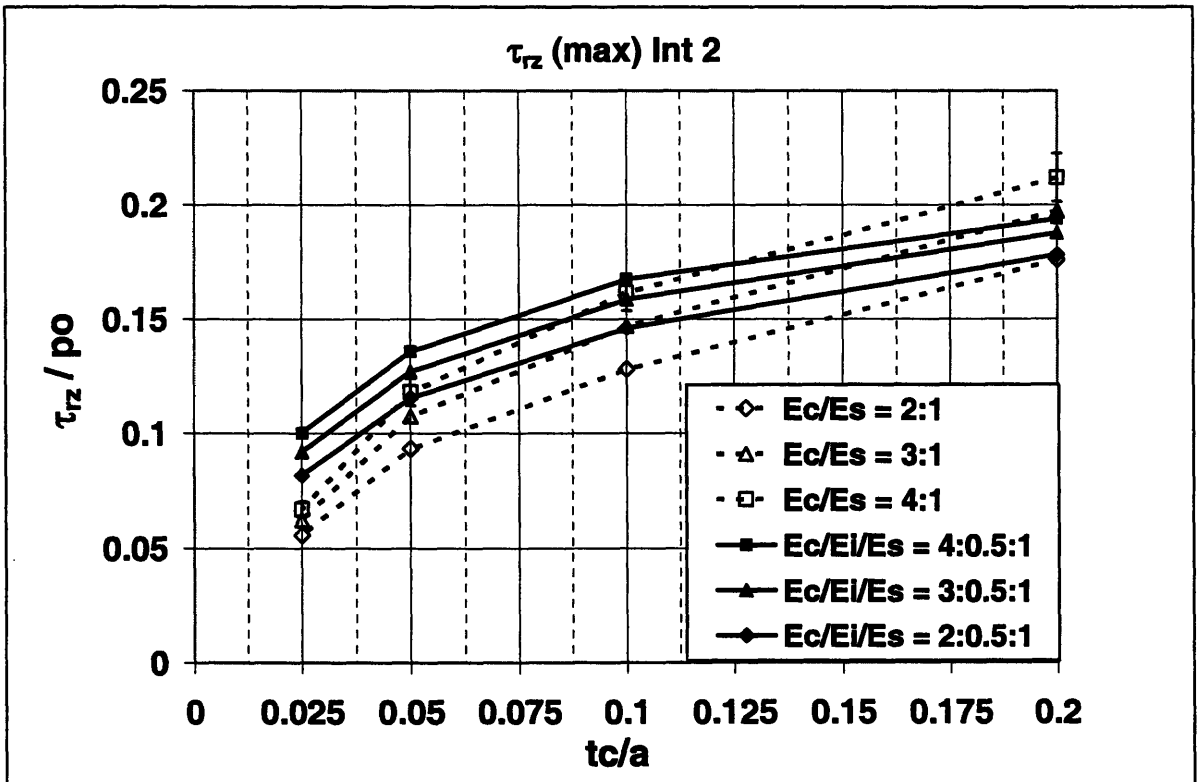

Figure 6.29: Shear stress τ_{rz} along the interlayer-substrate & monolayer-substrate

Figure 6.30 shows the in-plane compressive stresses within the coating at the coating-interlayer and monolayer-substrate interfaces.

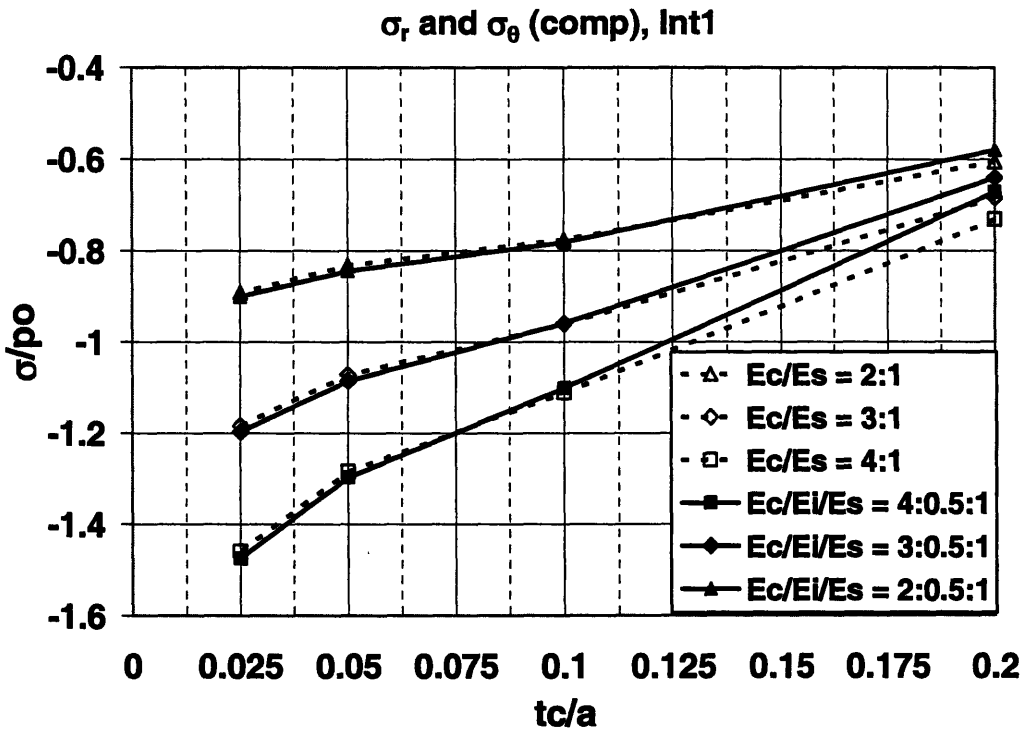

Figure 6.30: σ_r and σ_θ in coating-interlayer and monolayer-substrate interface

Figure 6.31 shows the in-plane compressive stresses within the coating at the interlayer-substrate and monolayer-substrate interfaces. In-plane compressive stresses within the coating at the coating-interlayer differ by approximately 1-5% from those at the monolayer-substrate interface. However, at the interlayer-substrate interface, they are approximately 60% lower.

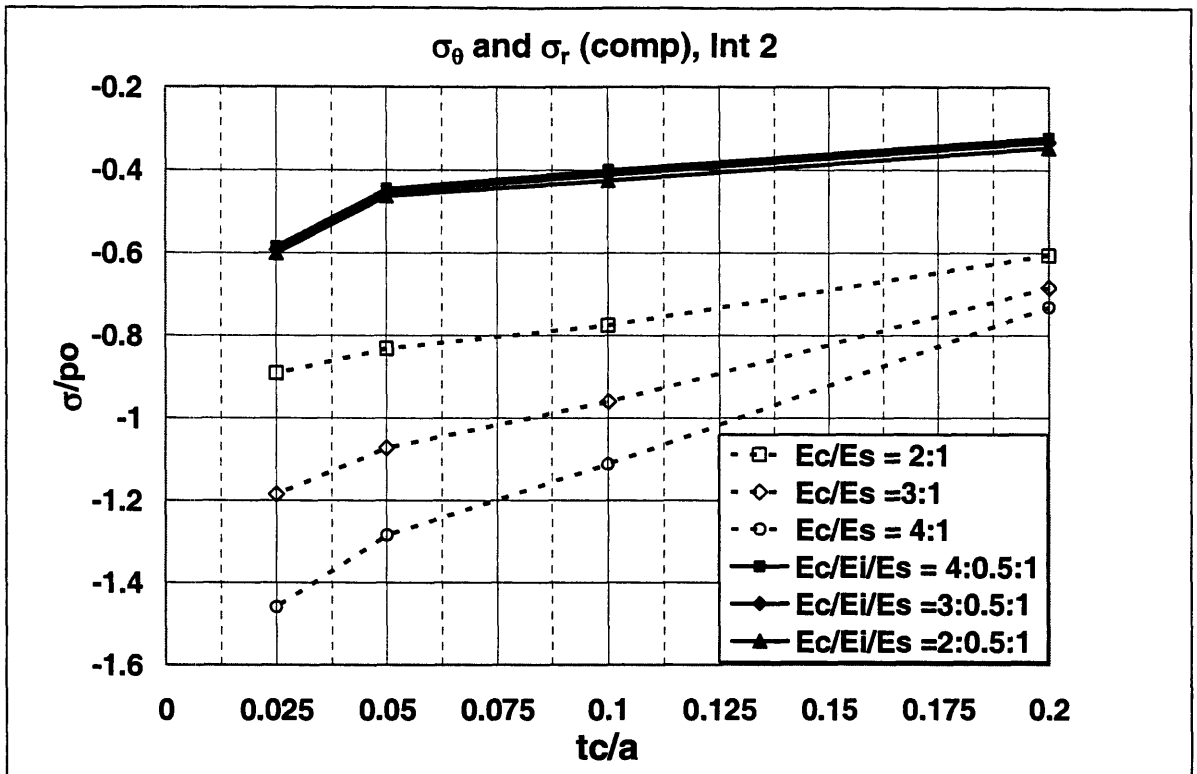

Figure 6.31: σ_r and σ_θ in interlayer-substrate and monolayer-substrate interface

Table 6.6 summarizes the effects of using a soft interlayer.

Table 6.6: Soft interlayer stresses compared to monolayer stresses

	σ_r (coating surface)	σ_r (coating-interlayer)	σ_r (interlayer-substrate)	τ_{rz} (coating-interlayer and interlayer-substrate)	σ_r, σ_θ (In-plane compressive stresses-coating)	σ_r, σ_θ (In-plane compressive stresses-interlayer)
% difference	10-15% higher	5% lower	80% lower	15% lower	1-5% deviation	60% lower

Table 6.7 lists the coefficients and exponents corresponding to Equation of form 6.1, used to characterize the stresses. Since interlayer modulus is kept constant at 0.5, it does not appear separately in the expression.

Table 6.7: Analytic expression for stress in soft interlayer configuration								
	K_1	p	q	K_2	r	s	Standard Deviation (% error)	Error Range(%)
σ_r(max) Surface	0.240	0.064	0.534	-0.160	0.134	-2.995	1.192	-1.98 to 1.89
σ_r (max) Int1	-0.08	-0.036	0.802	0.075	-0.216	0.673	4.413	-4.70 to 3.80
σ_r (max) Int2	0.0087	-0.536	-0.297	-0.033	0.565	0.189	2.40	-3.42 to 5.54
τ_{rz} (max) Int1	0.436	0.050	0.210	-0.237	-0.093	0.181	1.981	-3.25 to 4.55
τ_{rz} (max) Int2	0.448	0.0042	0.0393	-0.230	-0.137	-0.029	0.668	-1.20 to 1.08
σ_r, σ_θ Int1	-0.401	-0.097	0.684	0.550	1.490	1.728	1.958	-1.57 to 1.44
σ_r, σ_θ Int1	-0.651	-0.241	0.182	0.425	-0.229	0.285	3.808	-6.23 to 3.90

Overall, it seems that use of soft interlayer for thin coatings $\left(\frac{t_c}{a} < 0.1\right)$ provides some advantages over hard interlayer in terms of reduction of stresses, particularly tensile stresses at the interlayer-substrate interface. Tensile stresses at the interlayer-substrate interface are especially important because they may initiate interfacial cracks that act as potential sites for delamination.

6.9 Conclusion

These analyses show that stresses in thin coatings $\left(\frac{t_c}{a} < 0.1\right)$ are substantially different from those in thicker coatings. A design guideline is provided along with analytical model for selecting the appropriate coating thickness and modulus for monolayer coating configurations. The effect of hard and soft interlayer is studied and an analytic expression characterizing their effects is provided. Based on the results of these simulations, one may conclude that a soft interlayer would be more beneficial than a hard interlayer for the thickness and modulus ratios considered. The results of the present study are applicable to a given design scenario if

$$\frac{t_c}{a} = \left(\frac{2E_e t_c^3}{3FR_e}\right)^{1/3} < 0.1 \qquad \textbf{(6.2)}$$

Where:

$$E_e \text{ (equivalent modulus)} = \left(\frac{1-\nu_{ball}}{E_{ball}} + \frac{1-\nu_{groove}}{E_{groove}}\right)^{-1} = \left(\frac{1-\nu_{ball}}{E_{ball}} + \frac{1-\nu_{substrate}}{E_{substrate}}\right)^{-1}$$

$$R_e \text{ (equivalent radius of curvature)} = \left(\frac{1}{R_{ball}} + \frac{1}{R_{groove}}\right)^{-1}$$

F = External load

Equation 6.2 coupled with analytical models for coating stresses may be used to:

1. Determine an optimal coating configuration (t_c, E_c) for given contact conditions (R_e, E_e, E_s).

2. Determine contact conditions (R_e, E_e, E_s) to obtain optimal configuration for given coating parameters (t_c, E_c)

Knowledge of stress distribution is critical to determining probability of coating failure. In this regard, the results of the present study are very important. However, uncertainties associated with the coating process may result in large deviation in failure prediction based on stress distribution and those observed in practice. These uncertainties could relate to distribution of cracks at coating-substrate, coating-interlayer and interlayer-substrate interfaces or within the coating, interlayer and substrate. For the same stress distribution, the manner and occurrence of failure may be quite different depending on nature of these faults. The non-homogeneous nature of mechanical properties Young's modulus E and Poisson ratio, ν may also contribute to deviations. However if the coating process is consistent in terms of quality of adherence, distribution of cracks and mechanical properties, the simulation based results and analysis of the present study, may be used effectively to design quality coated interfaces for kinematic couplings.

Chapter 7 - Summary

This chapter summarizes the fundamental contributions, future work, and impact of the present research.

7.1 Fundamental contributions

This research marks the development of the first six-axis, active fixture capable of nanometer-level accuracy and repeatability. The key contributions of the present work are discussed below.

1. The development and testing of the HPF has shown that high-resolution actuators and hysteresis free compliant mechanisms may be integrated within traditionally passive fixtures to achieve nanometer-level accuracies. This marks an order of magnitude improvement over prior state-of-the art discussed in chapter 2, that have micron-level accuracies.
2. Kinematic couplings have long been used in instrumentation and other applications to provide alignment with repeatability of up to a few hundred nanometers. Recent research highlighted the potential of using flexures at contact interfaces of these couplings to reduce hysteresis, however its effect on repeatability was not studied. In the present work, flexures were specially designed and integrated into the HPF for improving repeatability and tests proved that sustained repeatability of a few tens of nanometers might be obtained.
3. Parametric models for the fixture's kinematics and stiffness were developed and validated through experiments and simulations. These models may be utilized to design and optimize fixtures based on the HPF.
4. Surface coatings may be utilized to enhance stability and longevity of the fixture's contact interfaces. Design of quality surface requires knowledge of stresses within coating and substrate. Much work has been done in understanding the behavior of

coatings stresses, however, knowledge regarding coatings with thickness to contact ratio less than 0.1 has not been available. This class of coatings $\left(\frac{t_c}{a} < 0.1\right)$ corresponds to most typical coating configurations in practical fixturing applications and hence its importance. To address this crucial knowledge gap, stresses in thin coatings with and without interlayer were analyzed and useable design guidelines were formulated. This knowledge may be utilized to design quality coated interfaces such as those for kinematic couplings.

7.2 Design improvements for HPF

Several potential design modifications may be made to the HPF to improve characteristics such as stiffness and load capacity.

1. The ball and grooves may be replaced with those made of harder materials (for example ceramics such as SiN) and/or specially shaped canoe balls [9] may be utilized to lower the contact stresses and to increase stiffness and load capacity of the HPF.
2. Ceramic balls and inserts may be used for the actuator-SBF ball-groove connection to reduce the contact stresses and prevent or limit plastic deformation. This would serve to increase the stiffness of the connection and thereby overall stiffness of the fixture.
3. Design of the grooved component's base may be modified to minimize the compliance of the beam elements mentioned in Section 5.5. This will serve to increase the overall stiffness of the fixture.
4. The size/area of the triangular mounts (used to mount the groove flexure) may be increased to enhance the strength of the bonding between the mount and the groove flexure.

7.3 Future research work

Several areas of future research that build up on the work presented in this thesis, are discussed below.

1. The stiffness model may be refined to better reflect structural compliances and compliance of bolted joints. This is expected to explain the existing 25% difference between results of the analytical stiffness model and the stiffness tests, thereby affirming the applicability of the model. The model may further be used to optimize the overall stiffness of the HPF.
2. Through the large and small displacement tests, the potential for nanometer-level accuracy of the HPF has been shown. Implementation of computer controller, closed loop operation of the HPF would serve to, (1) establish the nanometer-level performance of the HPF (2) lend a better understanding of factors affecting the same and (3) enable integration of HPF into practical applications.
3. Parasitic (unwanted) motions make it difficult if not impossible, to position the fixture independently in 3D space. To address this problem, sources of parasitic motions need to be analyzed in depth. This would entail measurement and quantification of various sources of the parasitics including those discussed in Section 5.2. This study would establish the steps to be undertaken to minimize the parasitics. These steps might include; tighter manufacturing and assembly tolerances for components, better manufacturing methods such as wire EDM for the flexures (SBF and groove flexures), error mapping and better sensor mounting and alignment.
4. Several applications of the HPF in ultra precision and nano-manufacturing fields have been suggested. The HPF must be studied in an industrial setting as a case study, to understand the factors affecting its performance. This would enable transfer of the HPF technology from research and development stage to practical applications.
5. The guidelines for designing thin coatings are based on finite element analysis. The utility of these guidelines needs to be evaluated through experiments on a variety of

coating configurations and comparison of experimental results with those from the FEA.

7.4 Impact

Many current and emerging applications such as photonics packaging, semiconductor test equipment, mask to wafer alignment and the like, require positioning in six axes with nanometer-level and micro-radian accuracy. In such applications, several parts might need to be positioned at many different machines, for instance in a manufacturing line. In these situations, it is desirable that the fixturing system used to align and affix the part provide rapid, repeatable and accurate means to place and remove the parts. Existing systems such as nanomanipulators require calibration each time a part is attached to the manipulator stage and are hence suited only for low rate applications. Additionally commercial nanomanipulators have limited load capacities (20-50N) that cannot accommodate forces from weight of parts and from manufacturing and assembly operations. Thus, these systems are limited to low force applications. These limitations are overcome by the Hybrid Positioning Fixture (HPF). The nanometer-level accuracy, repeatability and high load capacity of the HPF, make it suitable for the previously discussed applications. The HPF is particularly suited for integration into automated assembly and transfer lines, making nanometer-level precision possible in large scale production such as automotive industry and intergated circuits. The integration of HPF into palletized manufacturing process is discussed in Section 1.4. This makes nanometer-level precision possible without time and cost intensive calibration procedures. Additionally, the "drop and forget" capability of the HPF, discussed in Section 2.2, reduces costs associated with expensive machine vision systems used to align parts to the assembly/transfer line pallets. Thus the Hybrid Positioning Fixture sets the stage for large scale ultra-precision and nano-manufacturing. In addition to high-rate industrial applications, the HPF is also suited for use as a general purpose, high load capacity nanopositioning stage for research and low-rate industrial applications. The work done in

this thesis will (1) enable researchers to carry out further studies on hybrid fixtures, such as the HPF, that combine fixturing and positioning needs and (2) enable engineers to design and optimize such systems for specific applications.

References

[1] Culpepper, M.L. "Design and Application of Compliant Quasi-Kinematic Couplings." Ph.D. Thesis, Massachusetts Institute of Technology; February 2000.

[2] Slocum, A.H. "Design of Three-Groove Kinematic Couplings." Precision Engineering 1992; 14(2):67-76.

[3] Hale, L.C and Slocum, A.H. "Optimal Design Techniques for Kinematic Couplings." Precision Engineering 2001; 25;114-27.

[4] Hale, L.C. "Principles and techniques for designing precision machines." Ph.D. Thesis, Massachusetts Institute of Technology; February 1999.

[5] Slocum, A. "Kinematic couplings for precision fixturing – Part 1: Formulation of design parameters." Precision Engineering 1988, April; 10 (2): 85-91.

[6] Muller-Held, B. "Development of a repeatable tool-holder based on a statically deterministic coupling." M.S.Thesis, Massachusetts Institute of Technology; February 1998.

[7] Vallance, R.R., Morgan, C. and Slocum, A.H. "Precisely positioning pallets in multi-station assembly systems." Precision Engineering 2004;28; 218-231.

[8] Taylor, J.B. and Tu, J.F. "Precision X-Y micro-stage with maneuverable kinematic coupling mechanism." Precision Engineering 1996; 18:85-94.

[9] Hart, A.J. "Design and Analysis of Kinematic Couplings for Modular Machine and Instrumentation Structures." S.M. Thesis, Massachusetts Institute of Technology; Oct 2001.

[10] Slocum, A. and Donmez, A. "Kinematic couplings for precision fixturing – Part 2: Experimental determination of repeatability and stiffness." Precision Eng 1988; 10 (3): 115-122.

[11] Culpepper, M.L. "Design of detachable precision fixtures, which utilize hard and lubricant coatings to mitigate wear and reduce friction hysteresis." Proceedings of ASPE 18th Annual Meeting.

[12] Schouten, C.H., Rosielle, P.C.J.N. and Schellekens, P.H.J. "Design of a kinematic

coupling for precision applications." Precision Engineering 1997; 20:46-52.

[13] Culpepper M.L., Varadarajan, M.K. and DiBiasio, C. "Design of integrated mechanisms and exact constraint fixtures for micron-level repeatability and accuracy." Precision Engineering 2005; 29:65-80.

[14] Djabella, H. and Arnell, R.D. "Finite element analysis of the contact stresses in an elastic coating on an elastic substrate." Thin Solid Films 1992; 213: 205-219.

[15] Djabella, H. and Arnell R.D. "Finite element analysis of the contact stresses in elastic double-layer systems under normal load." Thin Solid Films 1993; 223: 98-108.

[16] Araque, C.A. "A kinematic-coupling based adaptive fixture for high precision positioning applications in flexible manufacturing systems." S.M. Thesis, Massachusetts Institute of Technology; February 2002.

[17] PI Datasheets: P-587 Long-Travel, 6-Axis, Single-Module Piezo Flexure NanoPositioner and Scanner, http://www.physikinstrumente.de/products.

[18] TECHNOTE: State-of-the Art NanoPositioning System http://www.physikinstrumente.de/pdf/State-of-the-Art-NanoPositioningSystemsPI.pdf.

[19] PI Datasheets: P-762 Family of Piezo Flexure NanoPositioners and Scanners, Technical Data, http://www.physikinstrumente.de/products/prdetail.php?secid=2-38.

[20] Slocum, A.H. "Precision machine design." Society of Manufacturing Engineers; 1992.

[21] Blanding, D.L. Exact Constraint: Machine Design Using Kinematic Principles. ASME Press, New York; 1999.

[22] Hale, L.C. "Friction-based design of kinematic coupling for precision applications." Proceedings of the American Society for Precision Engineering Annual Conference; 1998. p.45-8.

[23] Piezosystem jena - nanopositioning and Microsystems, http://www.piezojena.com/index1.php4?pre_cat_open=1&id=2&sort=sort&subid=102&subsort=sort&subsubid=210&prod_detail=119&prod_detail_more=119.

[24] Compliant Mechanism Tool: CoMeT, http://www.psdam.com/research.html.

[25] Johnson K.L. *Contact mechanics.* Cambridge , UK: Cambridge University Press; 1985.

[26] Tutorials: Displacement of Piezo Actuators (stack and contraction type), http://www.physikinstrumente.de/products/prdetail.php?secid=4-19.

[27] Awtar, S. "Synthesis and Analysis of Parallel Kinematic XY Flexure Mechanisms." Ph.D. Thesis, Massachusetts Institute of Technology; February 2004.

[28] Rointan, F.B. Handbook of hard coatings: Deposition Technologies, Properties and applications. Noyes Publications, New York; 2001.

[29] Bhowmick, S., Kale, A.N., Jayaram, V. and Biswas, S.K. "Contact damage in TiN coatings on steel." Thin Solid Films 2003; 436: 250-258.

[30] Michler, J. and Blank, E. "Analysis of coating fracture and substrate plasticity induced by spherical indenters: diamond and diamond-like carbon layers on steel substrates." Thin Solid Films 2001; 381: 119-134.

[31] Souza, R.M., Mustoe, G.G.W. and Moore, J.J. "Finite Element modeling of the stresses, fracture and delamination during indentation of hard elastic films on elastic-plastic soft substrates." Thin Solid Films 2001; 392:65-74.

[32] Abdul-baqi, A. and Giessen, E.V. "Indentation-induced interface delamination of a strong film on a ductile substrate." Thin Solid Films 2001; 381: 143-154.

[33] BryCoat Titanium Nitride coatings, http://www.brycoat.com/tin/physprop.html.

[34] Mencik, J. Mechanics of Components with Treated or Coated Surfaces. Kluwer Academic Publishers; 1996.

Appendix A - Part Drawings

This appendix contains the part drawings of the prototype Hybrid Positioning Fixture (HPF) and an exploded view of the test stand described in Section 5.2. Figure A.1 shows an exploded view of the HPF.

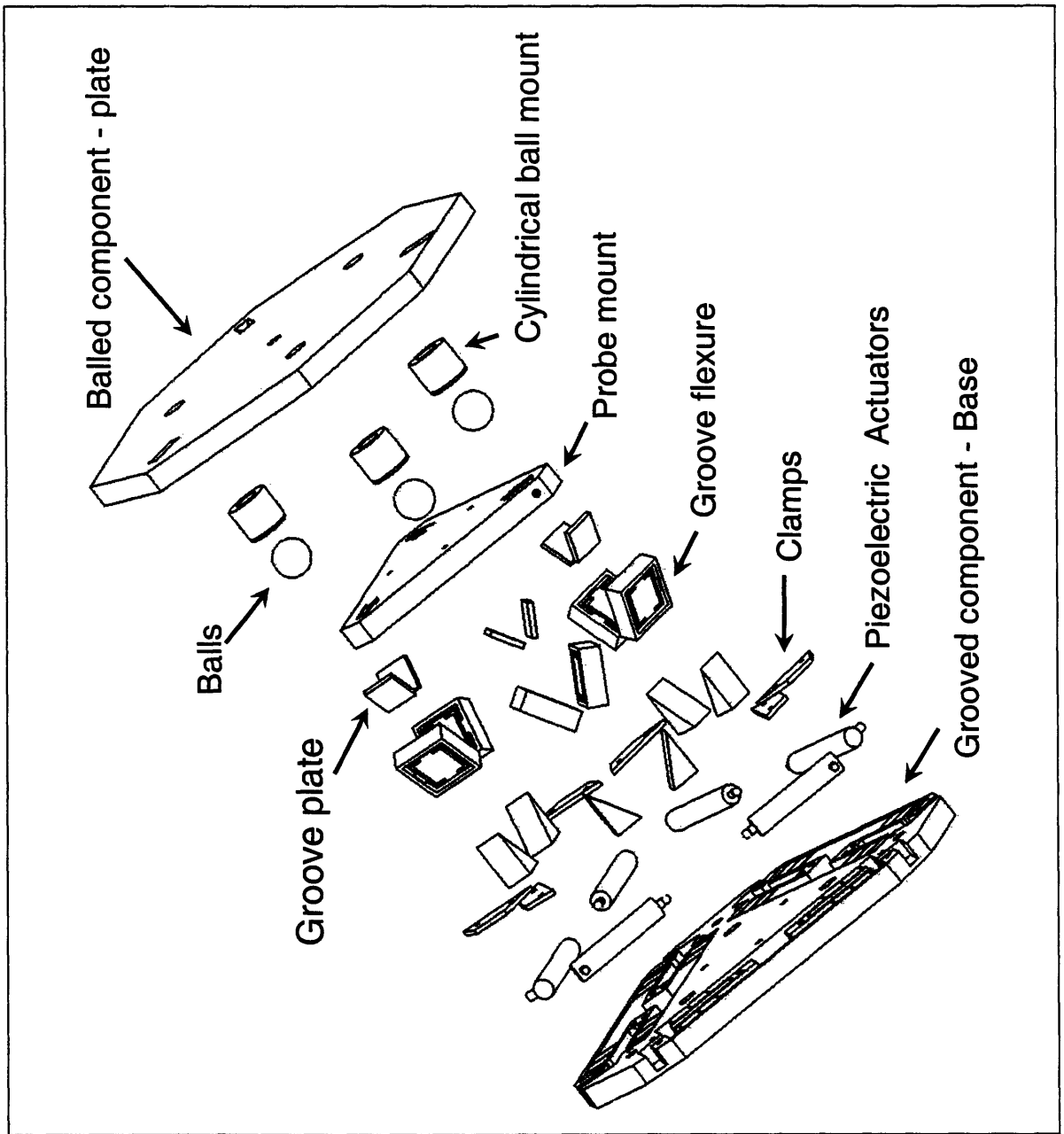

Figure A.1: Exploded view of Hybrid Positioning Fixture

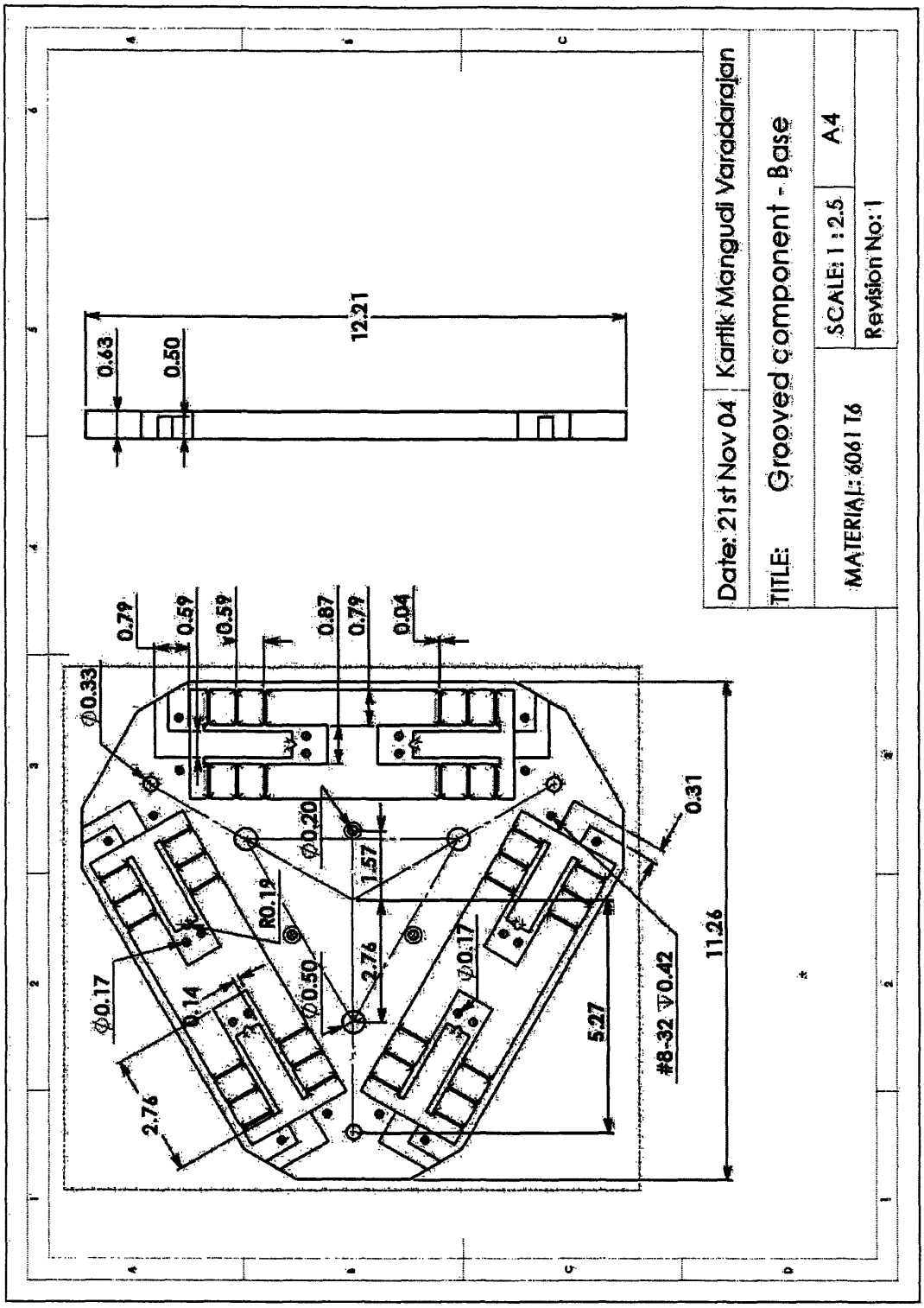

Figure A.2: HPF - grooved component-base

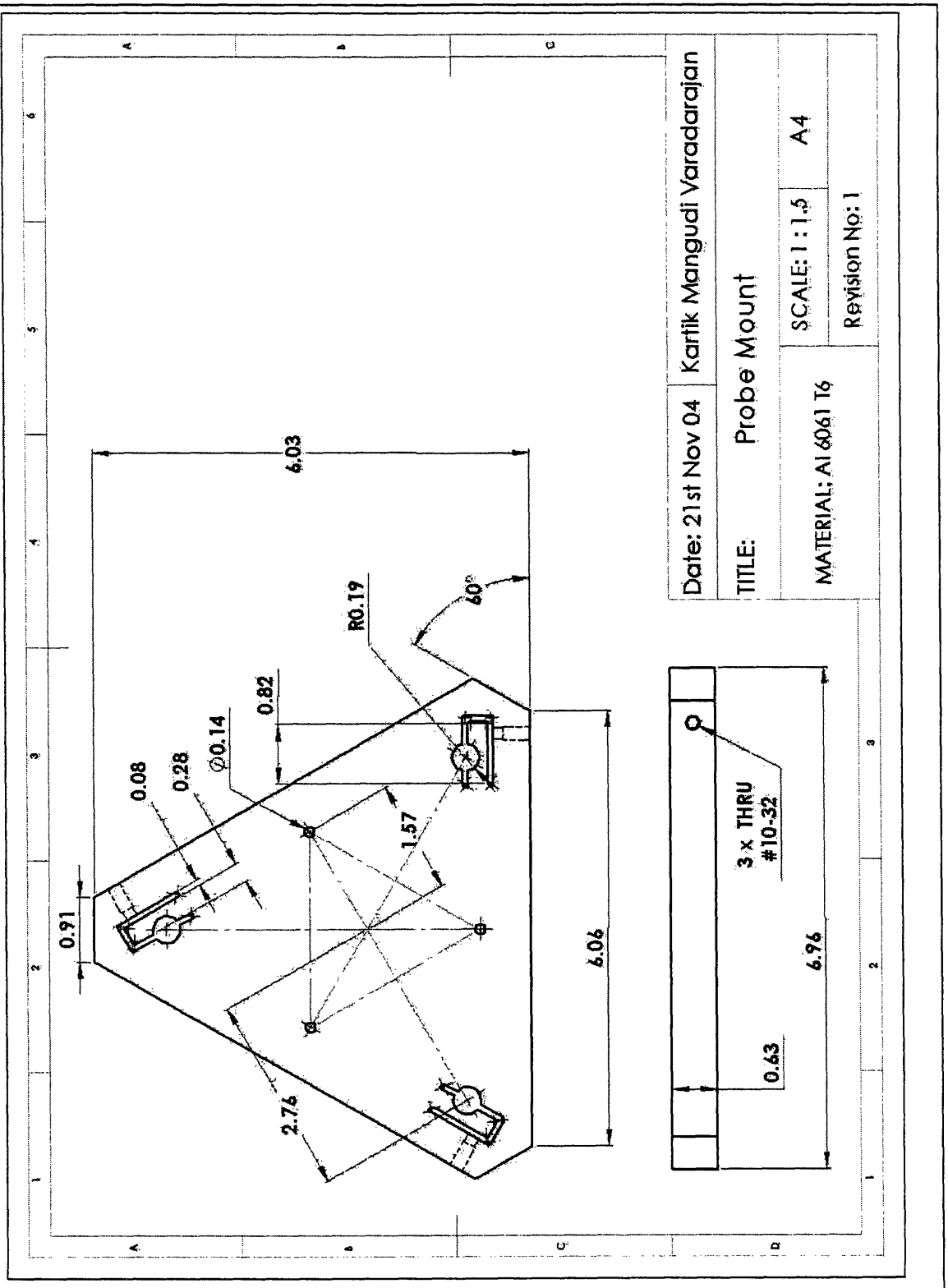

Figure A.3: HPF – probe mount

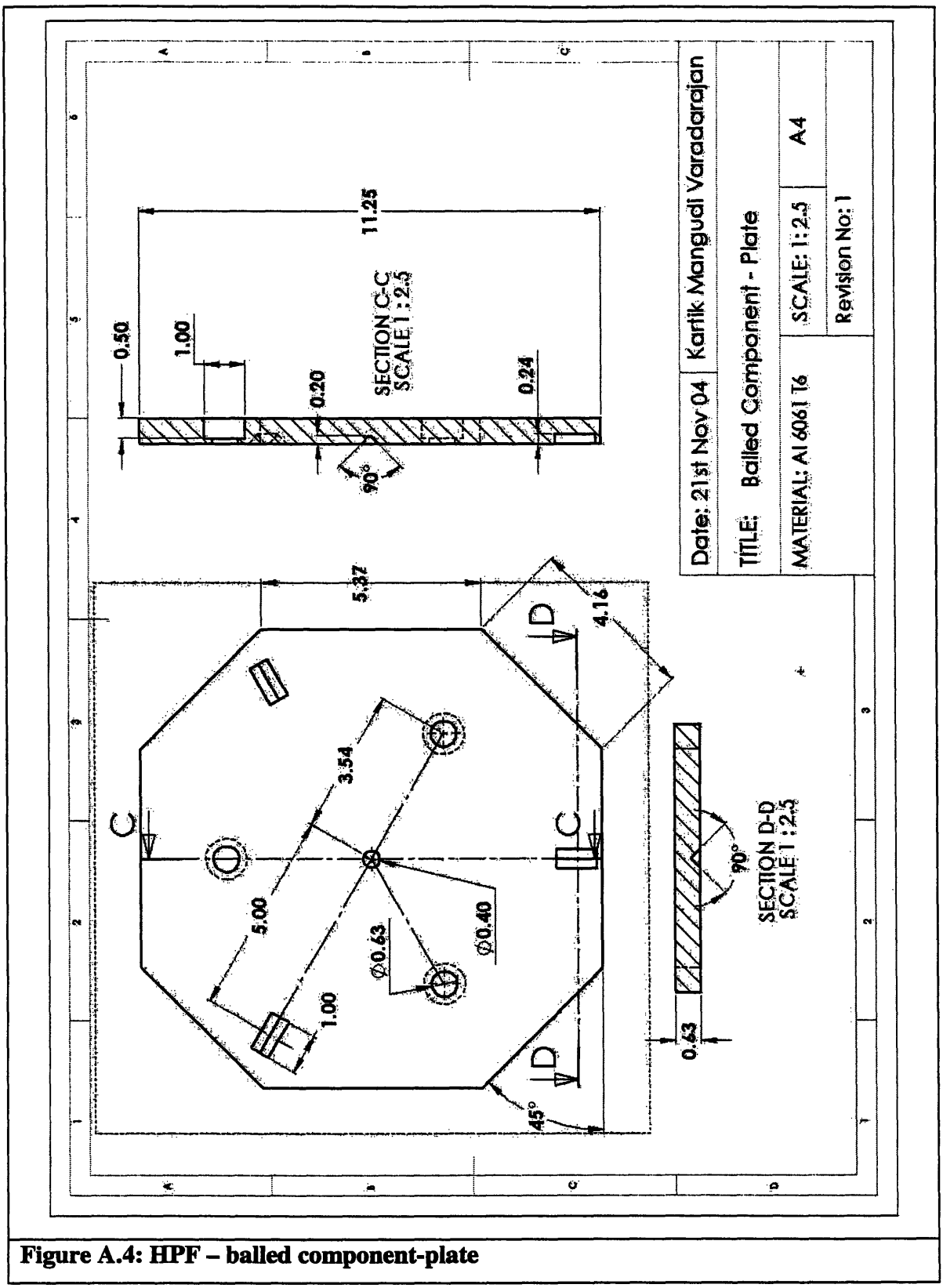

Figure A.4: HPF – balled component-plate

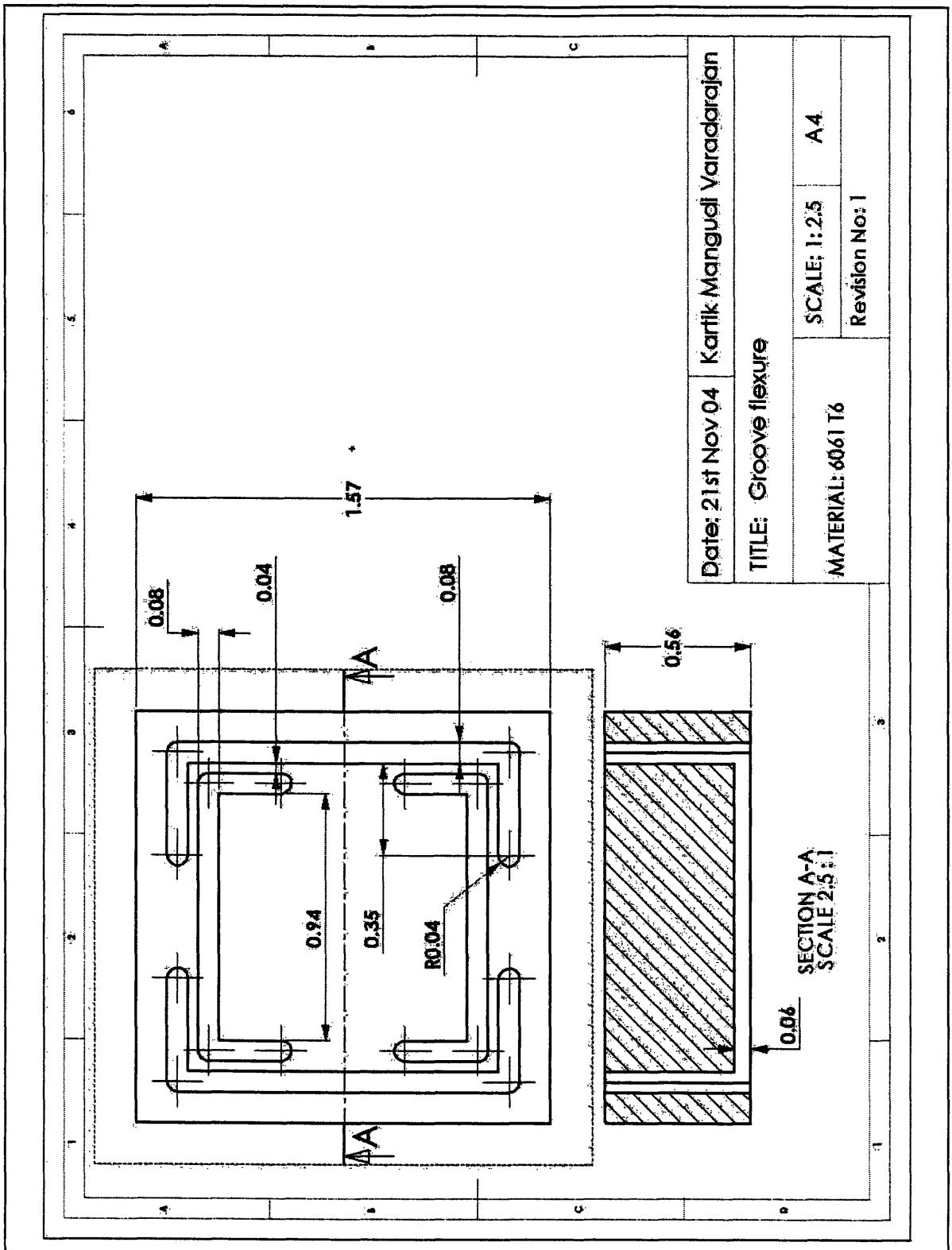

Figure A.5: HPF – groove flexure

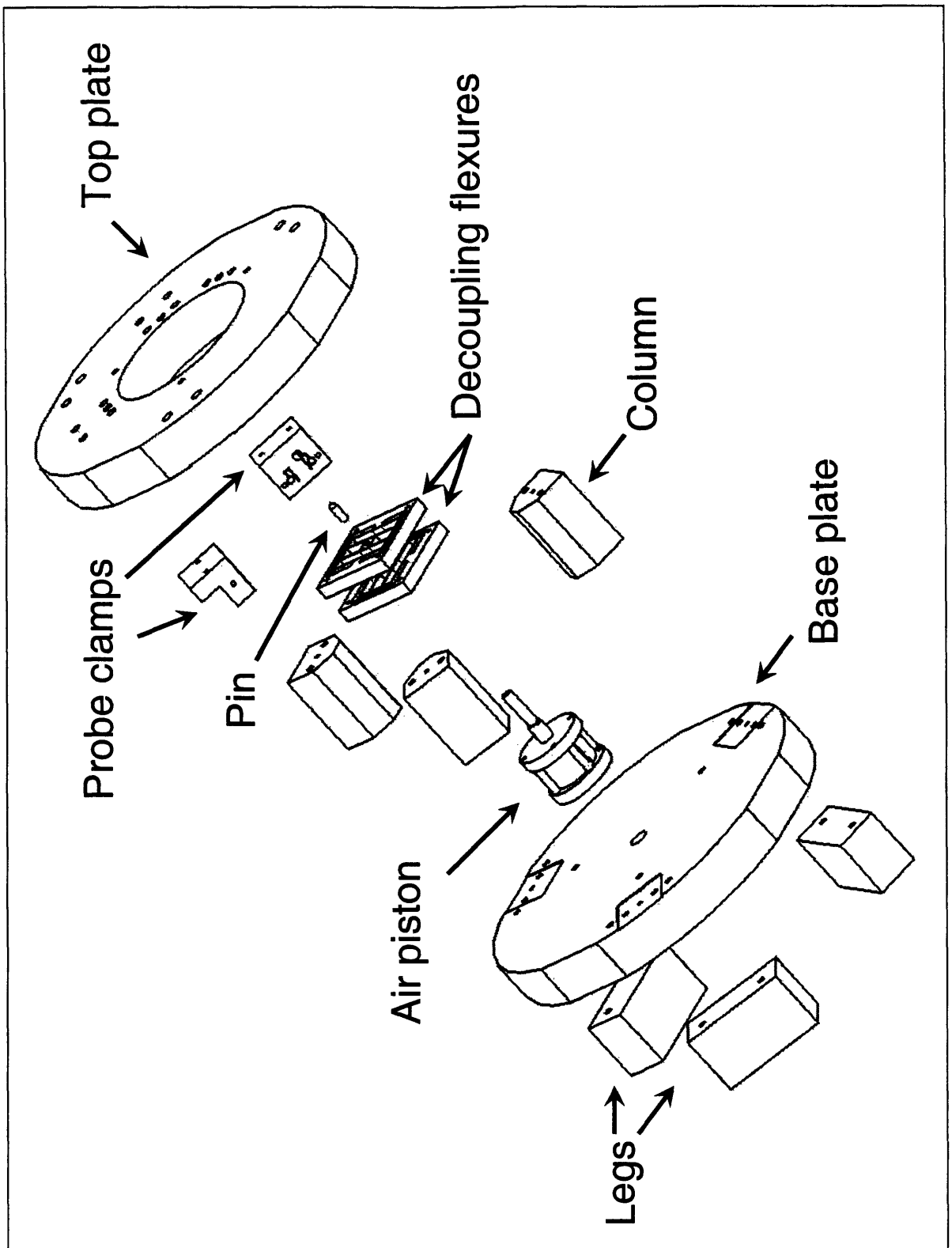

Figure A.6: Exploded view of test Stand

Appendix B - HPF kinematics

B.1 In-plane motion

In deriving the in-plane kinematics, the first step is to define the vector loops as shown in Figure B.1.

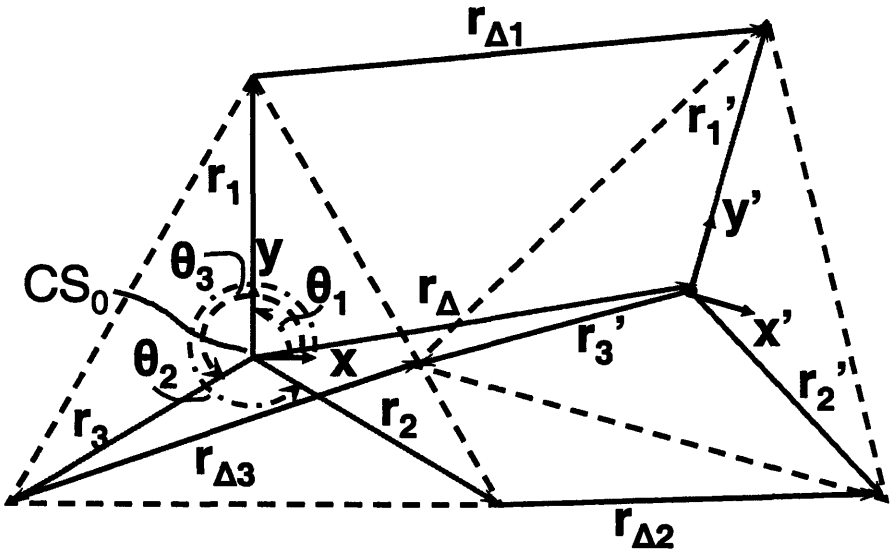

Figure B.1: Vector based model for in-plane motion

$$\text{Vector loops} \quad \begin{aligned} r_1 + r_{\Delta 1} - r_1' &= r_\Delta \\ r_2 + r_{\Delta 2} - r_2' &= r_\Delta \\ r_3 + r_{\Delta 3} - r_3' &= r_\Delta \end{aligned} \qquad \textbf{(B.1)}$$

Where $r_\Delta = X_c\hat{i} + Y_c\hat{j}$ is translation ($\hat{i}$, $\hat{j}$ are unit vectors in x, y direction) and θ_{zc} is the rotation of the balled component. Equation B.1 may be expanded to give Equation B.2.

$$\begin{bmatrix} x_1+\Delta x_1 & x_2+\Delta x_2 & x_3+\Delta x_3 \\ y_1+\Delta y_1 & y_2+\Delta y_2 & y_3+\Delta y_3 \\ z_1+\Delta z_1 & z_2+\Delta z_2 & z_3+\Delta z_3 \\ 1 & 1 & 1 \end{bmatrix} = \begin{bmatrix} 1 & -\theta_{zc} & 0 & X_c \\ \theta_{zc} & 1 & 0 & Y_c \\ 0 & 0 & 1 & 0 \\ 0 & 0 & 0 & 1 \end{bmatrix} \begin{bmatrix} L_1.c[\theta_1] & L_2.c[\theta_2] & L_3.c[\theta_3] \\ L_1.s[\theta_1] & L_2.s[\theta_2] & L_3.s[\theta_3] \\ 0 & 0 & 0 \\ 1 & 1 & 1 \end{bmatrix} \quad \textbf{(B.2)}$$

Further simplification of Equation B.2 gives Equation B.3. Using Equation B.3, the relation between motion of the fixture's centroid and displacement of the ball centers may be found.

$$\begin{aligned} x_i &= L_1 \cdot c[\theta_i] & \Delta x_i &= X_c - L_1 \cdot s[\theta_i] \cdot \theta_{zc} \\ y_i &= L_1 \cdot s[\theta_i] \text{ and} & \Delta y_i &= Y_c + L_1 \cdot c[\theta_i] \cdot \theta_{zc} \\ z_i &= 0 & \Delta z_i &= 0 \end{aligned} \quad \textbf{(B.3)}$$

$$X_c = \Delta x_1 + \left(\frac{L_1.s[\theta_1].(\Delta y_2 - \Delta y1)}{L_2.c[\theta_2] - L_1.c[\theta_1]} \right) \quad \textbf{(B.4)}$$

$$Y_c = \Delta y_2 - \left(\frac{L_2.c[\theta_2].(\Delta y_2 - \Delta y1)}{L_2.c[\theta_2] - L_1.c[\theta_1]} \right) \quad \textbf{(B.5)}$$

$$\theta_{zc} = \frac{\Delta y_2 - \Delta y_1}{L_2.c[\theta_2] - L_1.c[\theta_1]} \quad \textbf{(B.6)}$$

B.2 Out-of-plane motion

Figure B.2 shows the homed and displaced out-of-plane position of the fixture.

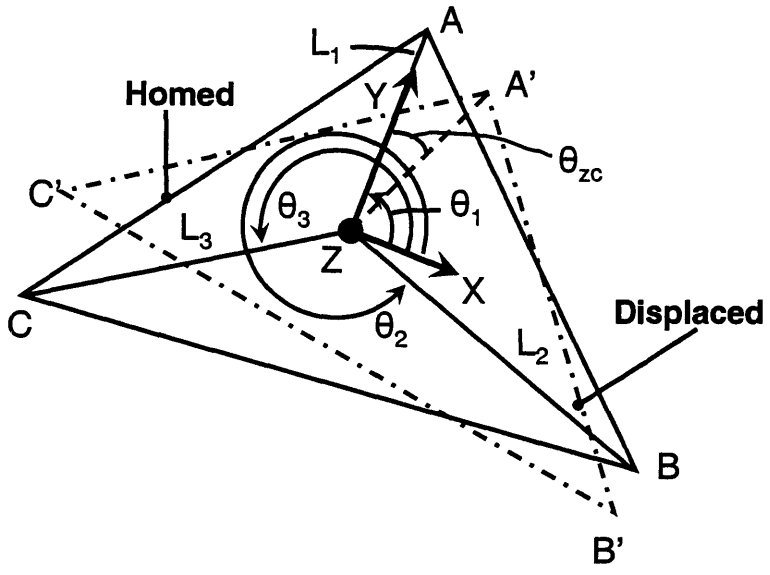

Figure B.2: Out-of-plane motion – homed and displaced locations

Coordinates defining homed and displaced locations are given in Equation B.7

$$\begin{bmatrix} A \\ B \\ C \\ A' \\ B' \\ C' \end{bmatrix} = \begin{bmatrix} L_1 \cdot c[\theta_1] & L_1 \cdot s[\theta_1] & 0 \\ L_2 \cdot c[\theta_2] & L_2 \cdot s[\theta_2] & 0 \\ L_3 \cdot c[\theta_3] & L_3 \cdot s[\theta_3] & 0 \\ L_1 \cdot c[\theta_1] - L_1 \cdot s[\theta_1] \cdot \theta_{zc} + X_c & L_1 \cdot s[\theta_1] + L_1 \cdot c[\theta_1] \cdot \theta_{zc} + Y_c & z_1 \\ L_2 \cdot c[\theta_2] - L_2 \cdot s[\theta_2] \cdot \theta_{zc} + X_c & L_2 \cdot s[\theta_2] + L_2 \cdot c[\theta_2] \cdot \theta_{zc} + Y_c & z_2 \\ L_3 \cdot c[\theta_3] - L_3 \cdot s[\theta_3] \cdot \theta_{zc} + X_c & L_3 \cdot s[\theta_3] + L_3 \cdot c[\theta_3] \cdot \theta_{zc} + Y_c & z_3 \end{bmatrix} \quad \textbf{(B.7)}$$

The next, step is to define normal vectors to the displaced and homed planes formed by the vertices listed in Equation B.7. The normal to homed plane is simply the unit vector $\hat{k}$ along Z-axis. Normal to displaced plane is given by Equation B.8.

$$\vec{N} = CB \times CA' = N_x\hat{i} + N_y\hat{j} + N_z\hat{k}$$

$$\begin{bmatrix} \hat{i} & \hat{j} & \hat{k} \\ (L_2 \cdot c[\theta_2] - L_2 \cdot s[\theta_2] \cdot \theta_{zc}) - (L_3 \cdot c[\theta_3] - L_3 \cdot s[\theta_3] \cdot \theta_{zc}) & (L_2 \cdot s[\theta_2] + L_2 \cdot c[\theta_2] \cdot \theta_{zc}) - (L_3 \cdot s[\theta_3] + L_3 \cdot c[\theta_3] \cdot \theta_{zc}) & \Delta z_2 - \Delta z_3 \\ (L_2 \cdot c[\theta_2] - L_2 \cdot s[\theta_2] \cdot \theta_{zc}) - (L_3 \cdot c[\theta_3] - L_3 \cdot s[\theta_3] \cdot \theta_{zc}) & (L_2 \cdot s[\theta_2] + L_2 \cdot c[\theta_2] \cdot \theta_{zc}) - (L_3 \cdot s[\theta_3] + L_3 \cdot c[\theta_3] \cdot \theta_{zc}) & \Delta z_1 - \Delta z_3 \end{bmatrix} \quad \textbf{(B.8)}$$

Where:

$$N_x = -L_1(s[\theta_1] + c[\theta_1] \cdot \theta_z) \cdot (\Delta z_2 - \Delta z_3) - L_2(s[\theta_2] + c[\theta_2] \cdot \theta_z) \cdot (\Delta z_3 - \Delta z_1) - L_3(s[\theta_3] + c[\theta_3] \cdot \theta_z) \cdot (\Delta z_1 - \Delta z_2) \quad \textbf{(B.9)}$$

$$N_y = -L_1(c[\theta_1] - s[\theta_1]\cdot\theta_z)\cdot(\Delta z_2 - \Delta z_3) - L_2(c[\theta_2] - s[\theta_2]\cdot\theta_z)\cdot(\Delta z_3 - \Delta z_1) - L_3(c[\theta_3] - s[\theta_3]\cdot\theta_z)\cdot(\Delta z_1 - \Delta z_2) \quad \textbf{(B.10)}$$

$$N_z = L_1 L_2 s[\theta_1 - \theta_2] + L_2 L_3 s[\theta_2 - \theta_3] + L_3 L_1 s[\theta_3 - \theta_1] \quad \textbf{(B.11)}$$

The magnitude of the normal vector is given by Equation B.12.

$$|N| = L_1 L_2 s[\theta_1 - \theta_2] + L_2 L_3 s[\theta_2 - \theta_3] + L_3 L_1 s[\theta_3 - \theta_1] \quad \textbf{(B.12)}$$

The unit vector along the normal to the displaced plane is given by Equation B.13 and shown graphically in Figure B.3.

$$\hat{n} = \frac{\vec{N}}{|N|} = -\sin[\theta_{yc}]\hat{i} + \sin[\theta_{xc}]\,\hat{j} + \hat{k} \approx -\theta_{yc}\hat{i} - \theta_{xc}\hat{i} + \hat{k} \quad \textbf{(B.13)}$$

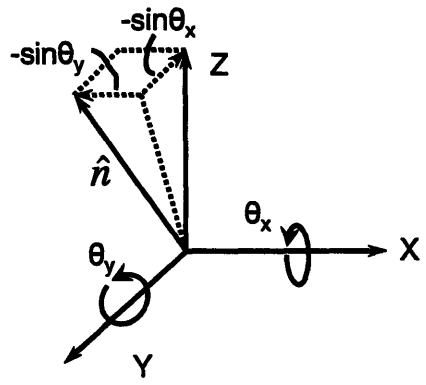

Figure B.3: Component of unit vector normal to displaced plane

From Equation B.13 and B.9-B.11 we obtain the out-of-plane motions of the fixture

$$\theta_{xc} \approx -\left(\frac{L_1.(s[\theta_1].\theta_z - c[\theta_1]).(\Delta z_2 - \Delta z_3) + L_2.(s[\theta_2].\theta_z - c[\theta_2]).(\Delta z_3 - \Delta z_1) + L_3.(s[\theta_3].\theta_z - c[\theta_3]).(\Delta z_1 - \Delta z_2)}{L_1.L_2.s[\theta_2 - \theta_1] + L_2.L_3.s[\theta_3 - \theta_2] + L_3.L_1.s[\theta_1 - \theta_3]}\right) \quad \textbf{(B.14)}$$

$$\theta_{yc} \approx \left(\frac{L_1.(s[\theta_1] + c[\theta_1].\theta_z).(\Delta z_2 - \Delta z_3) + L_2.(s[\theta_2] + c[\theta_2].\theta_z).(\Delta z_3 - \Delta z_1) + L_3.(s[\theta_3] + c[\theta_3].\theta_z).(\Delta z_1 - \Delta z_2)}{L_1.L_2.s[\theta_2 - \theta_1] + L_2.L_3.s[\theta_3 - \theta_2] + L_3.L_1.s[\theta_1 - \theta_3]}\right) \quad \textbf{(B.15)}$$

$$Z_c \approx L_1(\theta_{yc}.c[\theta_1] - \theta_{xc}.s[\theta_1]) + \Delta z_1 \quad \textbf{(B.16)}$$

B.3 Inverse kinematics

From Equation 4.1 we obtain relationship between motion of the groove surfaces ($\Delta g_{i1}, \Delta g_{i2}$) and motion of the corresponding ball center ($\Delta y_i, \Delta z_i$).

$$\Delta y_i = \frac{\Delta g_{i1} - \Delta g_{i2}}{2} \text{ and } \Delta z_i = \left(\frac{\Delta g_{i1} + \Delta g_{i2}}{2}\right).\tan\alpha \tag{B.7}$$

$$\Delta g_{i1} = \frac{\Delta z_i}{\tan\alpha} + \Delta y_i \text{ and } \Delta g_{i2} = \frac{\Delta z_i}{\tan\alpha} - \Delta y_i \tag{B.18}$$

From Equation B.16 we can obtain Equation B.19.

$$\Delta z_i = Z_c - L_i.(\theta_{yc}.c[\theta_i] - \theta_{xc}.s[\theta_i]) \tag{B.19}$$

From Equations 4.11, 4.12 and 4.15 we can obtain Equation B.20, B.21 and B.22.

$$\Delta y_i = \left(-(X_c - L_i.s[\theta_i].\theta_{zc}).s[\theta_i] + (Y_c + L_i.c[\theta_i].\theta_{zc}).c[\theta_i]\right) \tag{B.20}$$

$$\Delta g_{i1} = \left(\frac{Z_c - L_i.(\theta_{yc}.c[\theta_i] - \theta_{xc}.s[\theta_i])}{\tan\alpha}\right) + \left(-(X_c - L_i.s[\theta_i].\theta_{zc}).s[\theta_i] + (Y_c + L_i.c[\theta_i].\theta_{zc}).c[\theta_i]\right) \tag{B.21}$$

$$\Delta g_{i2} = \left(\frac{Z_c - L_i.(\theta_{yc}.c[\theta_i] - \theta_{xc}.s[\theta_i])}{\tan\alpha}\right) - \left(-(X_c - L_i.s[\theta_i].\theta_{zc}).s[\theta_i] + (Y_c + L_i.c[\theta_i].\theta_{zc}).c[\theta_i]\right) \tag{B.22}$$

Thus, for any desired motion of the fixture, the motion of the groove surfaces (actuators) may be calculated.

B.4 Excel spreadsheet – HPF kinematics

The forward and inverse kinematics of the HPF (Section 4.2, B.1, B.2) is implemented in an Excel spreadsheet and presented in Figure B.4.

Spreadsheet description and usage

Only the items that are bolded and italicized need to be entered.

- Enter the coupling geometry in the section marked coupling characteristics.
- Inverse kinematics: Enter the desired coupling motions in the row marked "Desired" under the Inverse kinematics section. The required groove/actuator motions are calculated and displayed under the column marked "Inverse" in the Groove motion section.
- Forward kinematics: Enter the groove/actuator motion under the column marked "forward" in the Groove Motion section. Next, run the solver in the location shown; the motion of the coupling is displayed in the row marked "Resultant" under the Forward kinematics section.

CNF Motion Kinematics

Do not change items in BLUE and RED

Coupling Characteristics

	degrees	radians
θ1	***90.00***	1.57
θ2	***330.00***	5.76
θ3	***210.00***	3.67

	microns	inches
L1	***80000.00***	3.15
L2	***80000.00***	3.15
L3	***80000.00***	3.15

Side Lengths	microns
Ls1	138564.06
Ls2	138564.06
Ls3	138564.06

Intial Config

	microns		microns		microns
X1	0.00	X2	69282.03	X3	-69282.03
Y1	80000.00	Y2	-40000.00	Y3	-40000.00
Z1	0.00	Z2	0.00	Z3	0.00

	degrees	radians
α (Groove	***60.00***	1.05

Groove Motion

	Forward	Inverse
δg11 (micrc	***0.600***	0.000
δg12 (micrc	***-0.600***	0.000
δg31 (micrc	***0.600***	0.866
δg32 (micrc	***-0.600***	-0.866
δg21 (micrc	***0.600***	-0.866
δg22 (micrc	***-0.600***	0.866

Local CS

	microns			microns			microns	
δx1	1.000	0.000	δx2	-0.500	0.000	δx3	-0.500	0.000
δy1	0.000	0.600	δy2	0.866	0.600	δy3	-0.866	0.600
δz1	0.000	0.000	δz2	0.000	0.000	δz3	0.000	0.000

Global CS

	microns			microns			microns	
δx10	0.000	-0.600	δx20	0.000	0.300	δx30	0.000	0.300
δy10	1.000	0.000	δy20	1.000	0.520	δy30	1.000	-0.520
δz10	0.000	0.000	δz20	0.000	0.000	δz30	0.000	0.000

Inverse Kinematics

	Xc (microns)	Yc (microns)	Zc (microns)	θx (μradians	θy (μradians	θz (μradians)
Desired	***0.000***	***1.000***	***0.000***	***0.000***	***0.000***	***0.000***

Forward Kinematics

	Xc (microns)	Yc (microns)	Zc (microns)	θx (μradians	θy (μradians	θz (μradians)
Resultant	0.000	0.000	0.000	0.000	0.000	7.500

Run solver here --->	**0.000**
Constraint 1	**0.000**
Constraint 2	**0.000**

Figure B.4: Excel worksheet – HPF kinematics

Appendix C - Stiffness modeling

Equations C.1 - C.4 define the generic transformation ***Tr*** used in Section 4.3.

$$Txyz = \begin{bmatrix} 1 & 0 & 0 & 0 & 0 & 0 \\ 0 & 1 & 0 & 0 & 0 & 0 \\ 0 & 0 & 1 & 0 & 0 & 0 \\ 0 & -Z & Y & 1 & 0 & 0 \\ Z & 0 & -X & 0 & 1 & 0 \\ -Y & X & 0 & 0 & 0 & 1 \end{bmatrix} \text{Linear translation} \qquad \textbf{(C.1)}$$

$$Rx = \begin{bmatrix} 1 & 0 & 0 & 0 & 0 & 0 \\ 0 & \cos(\theta_x) & -\sin(\theta_x) & 0 & 0 & 0 \\ 0 & \sin(\theta_x) & \cos(\theta_x) & 0 & 0 & 0 \\ 0 & 0 & 0 & 1 & 0 & 0 \\ 0 & 0 & 0 & 0 & \cos(\theta_x) & -\sin(\theta_x) \\ 0 & 0 & 0 & 0 & \sin(\theta_x) & \cos(\theta_x) \end{bmatrix} \text{Rotation about X axis} \qquad \textbf{(C.2)}$$

$$Ry = \begin{bmatrix} \cos(\theta_y) & 0 & \sin(\theta_y) & 0 & 0 & 0 \\ 0 & 1 & 0 & 0 & 0 & 0 \\ -\sin(\theta_y) & 0 & \cos(\theta_y) & 0 & 0 & 0 \\ 0 & 0 & 0 & \cos(\theta_y) & 0 & \sin(\theta_y) \\ 0 & 0 & 0 & 0 & 1 & 0 \\ 0 & 0 & 0 & -\sin(\theta_y) & 0 & \cos(\theta y) \end{bmatrix} \text{Rotation about Y axis} \qquad \textbf{(C.3)}$$

$$Rz = \begin{bmatrix} \cos(\theta_z) & -\sin(\theta_z) & 0 & 0 & 0 & 0 \\ \sin(\theta_z) & \cos(\theta_z) & 0 & 0 & 0 & 0 \\ 0 & 0 & 1 & 0 & 0 & 0 \\ 0 & 0 & 0 & \cos(\theta_z) & -\sin(\theta_z) & 0 \\ 0 & 0 & 0 & \sin(\theta_z) & \cos(\theta_z) & 0 \\ 0 & 0 & 0 & 0 & 0 & 1 \end{bmatrix} \text{Rotation about Z axis} \qquad \textbf{(C.4)}$$

The stiffness model developed in Section 4.2 was implemented in MATLAB™. All related MATLAB™ files are provided below.

Coupling_motion1.m

```
function [K,C] = Coupling_motion1(KC_data, loads, Flex_data)
% Updated 24th Nov 2004
% Function Calculates and returns [6x6] compliance and stiffness matrix for the HPF
% USAGE [K,C] = Coupling_motion1('Kc_data file','loads','Flex_data')
% 'Kc_data file'        - Characteristics of kinematic coupling
% 'Loads'               - External loads
% 'Flex_data'  -Characteristics of groove flexure
 read_KCdata(KC_data);          % Read in fixture characteristics
global pi Rb1 Rb2 Eb Gb Rg1 Rg2 Gg Eg vb vg mu Gr_ang
global L1c L2c L3c Theta1 Theta2 Theta3
pi = 3.14159;
F = (equilibrium_eq(loads))';   % Calculates the Normal contact forces
Ko = zeros(6,6);
[Pob, Pbc] = pos_matrix;        % Read location of ball centers and groove surfaces
% Transformation from CS at groove surface to CS at corresponding ball-center
for j  = 1:6
   K1{j}= Tr(Pbc,j)*Kmatrix1(F(j),j,Flex_data)*Tr(Pbc,j)';
   end
end
% Transformation from CS at ball-center to global CS at centroid of balled component
for j  = 1:6
      Ko = Ko + Tr(Pob,j)*K1{j}*Tr(Pob,j)';
end
K = Ko;                         % K = Stiffness Matrix
C = inv(Ko);                    % C = Compliance Matrix
% ------------------------------------ End of function ----------------------------------------
```

read_KCdata.m

```
function read_KCdata(file_name)
% Updated 24th November 2004
% Function for reading geometric and mechanical properties of fixture
% contained in text file "file_name", example KCproperties1.txt
global Rb1 Rb2 Eb Gb vb Rg1 Rg2 Eg Gg vg mu   % Properties of ball and grooves
global L1c L2c L3c Theta1 Theta2 Theta3       % Coupling geometric
global Gr_ang Gr_tilt  alpha                  % Groove geometry
file_id = fopen(file_name);
```

```
% Mechanical properties of ball
for i=1:5
   fgetl(file_id);
end
Rb1 = fscanf(file_id,'%e ',[1]);                    % Major radii
Rb2 = fscanf(file_id,'%e ',[1]);                    % Minor radii
Eb  = fscanf(file_id,'%e ',[1]);                    % Young's modulus
Gb  = fscanf(file_id,'%e ',[1]);                    % Shear modulus
vb  = fscanf(file_id,'%e ',[1]);                    % Poisson's ratio
% Mechanical properties of groove
for i=1:1
   fgetl(file_id);
end
Rg1 = fscanf(file_id,'%e ',[1]) ;                   % Major radii
Rg2 = fscanf(file_id,'%e ',[1]) ;                   % Minor radii
Eg = fscanf(file_id,'%e ',[1]);                     % Young's modulus
Gg = fscanf(file_id,'%e ',[1]);                     % Shear modulus
vg = fscanf(file_id,'%e ',[1]);                     % Poisson's ratio
fgetl(file_id);
mu = fscanf(file_id,'%e ',[1]);                     % Friction coefficient
% Fixture Geometry
for i=1:3
   fgetl(file_id);
end
 L1c = fscanf(file_id,'%e ',[1]);
 L2c = fscanf(file_id,'%e ',[1]);
 L3c = fscanf(file_id,'%e ',[1]);
 Theta1 = fscanf(file_id,'%e ',[1]);
 Theta2 = fscanf(file_id,'%e ',[1]);
 Theta3 = fscanf(file_id,'%e ',[1]);
% Groove geometry
fgetl(file_id);
Gr_ang = fscanf(file_id,'%e ',[1]);
alpha  = fscanf(file_id,'%e ',[1]);
fgetl(file_id);
Gr_tilt = fscanf(file_id,'%e ',[1,6]);
fclose(file_id);
% ---------- End of function ----------
```

Structure of text file "file_name" containing fixture properties

KCproperties1.txt
Fixture Properties

Material Properties

Rb1(m)	Rb2	Eb(Pa)	Gb(Pa)	vb
12.7e-3	12.7e-3	193e9	75.4e9	0.28
Rg1(m)	Rg2	Eg(Pa)	Gg (Pa)	vg
1e20	1e20	193e9	75.4e9	0.28

Friction Coeff (mu)
0.0
Geometry

L1c(m)	L2c	L3c	Theta1(deg)	Theta2	Theta3
80e-3	80e-3	80e-3	90	210	330

Gr_ang (deg)	alpha (deg)
60	90

Gr_Tilt Angles (deg)

180	360	-60	120	60	240

% ---------- End of file----------

equilibrium_eq.m

```
function F = equilibrium_eq (loads)
% Updated 24th Nov 2004
% Function calculates the normal forces at the ball-groove contacts based on
% equilibrium Equations. F is a matrix containing values of these forces.
global pi Rb Eb Gb Rg Gg Eg vb vg mu Gr_ang Gr_tilt
[P, Pos_P, L, Pos_L,Pos_C] = readloads(loads);  % Read in external loads data
% P = Preload, L = external load
% Pos_P = position of preload, Pos_C = position of external load
% Direction cosines
for j = 1:6
Alpha(j) = cos(Gr_tilt(j)*pi/180)*sin(Gr_ang*pi/180);
Beta (j) = sin(Gr_tilt(j)*pi/180)*sin(Gr_ang*pi/180);
Gamma(j) = cos(Gr_ang*pi/180);
end
for i = 1:6
dir_cos(i,1) = Alpha(i);
dir_cos(i,2) = Beta (i);
dir_cos(i,3) = Gamma(i);
end
A = zeros(6,6);
B = zeros(6,1);
% Equilibrium Equations
for j = 1:3
   B(j,1) = -(P(1,j)+P(2,j) + P(3,j) + L(j));      % RHS = preload + external load;
```

```
   for i=1:6
   A(j,i) = dir_cos(i,j);
   end
end
for(j = 4:6)
   for i = 1:3
   B(j,1) = B(j,1)-(-P(i,2)*Pos_P(i,3) +P(i,3)*P(i,2));
   end
end
B(4,1) = B(4 )+ L(2)*Pos_L(3) - L(3)*Pos_L(2);
B(5,1) = B(5) - L(1)*Pos_L(3) + L(3)*Pos_L(1);
B(6,1) = B(6) + L(1)*Pos_L(2) - L(2)*Pos_L(1);
for i=1:6
 A(4,i) =A(4,i) - dir_cos(i,2)*Pos_C(i,3)+ dir_cos(i,3)*Pos_C(i,2);
 A(5,i) =A(5,i) + dir_cos(i,1)*Pos_C(i,3)- dir_cos(i,3)*Pos_C(i,1);
 A(6,i) =A(6,i) - dir_cos(i,1)*Pos_C(i,2)+ dir_cos(i,2)*Pos_C(i,1);
end
% Solution of Equilibrium Equations
 F = A\B;
% ---------- End of function ----------
```

Structure of text file "loads" containing external loads

loads1.txt

Preload

px	py	pz	X	Y	Z
0	0	-225	0	0	22.5
0	0	0	0	0	0
0	0	0	0	0	0

External Load

Lx	Ly	Lz	X	Y	Z
0	0	0	0	0	0

Position of normal contact forces (mm)

Fx	Fy	Fz
11	80	-6.35
-11	80	-6.35
-74.782	-30.474	-6.35
-63.782	-49.526	-6.35
63.782	-49.526	-6.35
74.782	-30.474	-6.35

```
% ---------- End of file ----------
```

pos_matrix.m

```
function [Pob,Pbc] = pos_matrix
% Updated 24th Nov 2004
% Outputs [6 x 6] matrix containing the sequence of moves required
% to transform stiffness to global CS (at centroid of balled component).
% Pbo relates position of ball centers to balled-component's Centroid
% Pcb relates position of contact points to corresponding ball center

global pi Rb1 Rb2 Rg Gr_ang Theta1 Theta2 Theta3
global L1c L2c L3c
Xob    =  [L1c*cos(Theta1*pi/180), L1c*cos(Theta1*pi/180), L2c*cos(Theta2*pi/180),
L2c*cos(Theta2*pi/180), L3c*cos(Theta3*pi/180), L3c*cos(Theta3*pi/180)];
Yob    =  [L1c*sin(Theta1*pi/180), L1c*sin(Theta1*pi/180),
L2c*sin(Theta2*pi/180),L2c*sin(Theta2*pi/180), L3c*sin(Theta3*pi/180),
L3c*sin(Theta3*pi/180)];
Zob    =  [0, 0, 0,0, 0, 0];
thetaXob =  [0, 0, 0,0, 0, 0];
thetaYob =  [0, 0, 0,0, 0, 0];
thetaZob =  [Theta1+180, Theta1, Theta2+180,Theta2, Theta3+180, Theta3];
Pob = [ Xob; Yob; Zob; thetaXob; thetaYob; thetaZob] ;% [6 x 6 ]

Xbc    =  [0 0 0 0 0 0];
Ybc    =  [Rb1*sin(Gr_ang*pi/180) Rb1*sin(Gr_ang*pi/180) Rb1*sin(Gr_ang*pi/180)
Rb1*sin(Gr_ang*pi/180) Rb1*sin(Gr_ang*pi/180) Rb1*sin(Gr_ang*pi/180)];
Zbc    =  [-Rb1*cos(Gr_ang*pi/180) -Rb1*cos(Gr_ang*pi/180) -
Rb1*cos(Gr_ang*pi/180) -Rb1*cos(Gr_ang*pi/180) -Rb1*cos(Gr_ang*pi/180) -
Rb1*cos(Gr_ang*pi/180)];
thetaXbc =  [Gr_ang, Gr_ang, Gr_ang, Gr_ang, Gr_ang, Gr_ang];
thetaYbc =  [0 0 0 0 0 0 ];
thetaZbc =  [0 0 0 0 0 0 ];
Pbc= [ Xbc; Ybc; Zbc; thetaXbc; thetaYbc; thetaZbc]; % [6 x 6 ]
% ---------- End of function ----------
```

Tr.m

```
function T = Tr(P,j)
% Updated 24th Nov 2004
% Generic definition of transform from local to global coordinate system
% Given displacements with respect to local CS, the transformation
% gives displacements in the global CS
```

```
X = P(1,j);
Y = P(2,j);
Z = P(3,j);
pi = 3.14159;
thetaX = P(4,j);
thetaY = P(5,j);
thetaZ = P(6,j);
% Rotation about X axis
Rx = [ 1 0 0 0 0 0;
     0 cos(thetaX*pi/180) -sin(thetaX*pi/180) 0 0 0;
     0 sin(thetaX*pi/180) cos(thetaX*pi/180) 0 0 0;
     0 0 0 1 0 0 ;
     0 0 0 0 cos(thetaX*pi/180) -sin(thetaX*pi/180);
     0 0 0 0 sin(thetaX*pi/180) cos(thetaX*pi/180)];
% Rotation about Y axis
Ry = [ cos(thetaY*pi/180) 0 sin(thetaY*pi/180) 0 0 0;
     0 1 0 0 0 0;
     -sin(thetaY*pi/180) 0 cos(thetaY*pi/180) 0 0 0;
     0 0 0 cos(thetaY*pi/180) 0 sin(thetaY*pi/180);
     0  0 0 0 1 0;
     0 0 0 -sin(thetaY*pi/180) 0 cos(thetaY*pi/180)];
% Rotation about Z axis
Rz = [ cos(thetaZ*pi/180) -sin(thetaZ*pi/180) 0 0 0 0;
     sin(thetaZ*pi/180) cos(thetaZ*pi/180)  0 0 0 0;
     0 0 1 0 0 0 ;
     0 0 0 cos(thetaZ*pi/180) -sin(thetaZ*pi/180) 0;
     0 0 0 sin(thetaZ*pi/180) cos(thetaZ*pi/180) 0;
     0 0 0 0 0 1 ];
% Translation in X, Y and Z
Txyz = [ 1 0 0 0 0 0;
       0 1 0 0 0 0;
       0 0 1 0 0 0;
       0 -Z Y 1 0 0;
       Z 0 -X 0 1 0;
       -Y X 0 0 0 1];
T = Txyz*Rz*Ry*Rx;
% ---------- End of function ----------
```

Kmatrix1.m

```
function K = Kmatrix1 (F,j,flex_data)
% Updated 24th Nov 2004
% The function calculates the stiffness associated with each contact interface.
```

```
% USAGE K = Kmatrix1(F,j,flex_data), F = contact force (N),j = contact interface no.,
% flex_data = text file containing groove flexure properties example 'sqflexure.txt'

global pi Rb1 Rb2 Eb Gb Rg1 Rg2 Gg Eg vb vg mu alpha Gr_ang;
pi = 3.1415926;

Ee = ((1-vb.^2)/Eb + (1-vg.^2)/Eg).^(-1);
Ge = ((2-vb)/Gb + (2-vg)/Gg).^(-1);
A_plusB  = 0.5*(1/Rb1 + 1/Rb2 + 1/Rg1 + 1/Rg2);
B_minusA = 0.5*((1/Rb1 - 1/Rb2).^2 + (1/Rg1 - 1/Rg2).^2 + 2*(1/Rb1 - 1/Rb2)*(1/Rg1
- 1/Rg2)*cos(2*alpha*pi/180)).^0.5;
Ra = ( A_plusB - B_minusA).^-1;
Rb = ( A_plusB + B_minusA).^-1;
Re = (Ra * Rb).^0.5
e  = (1- (Rb/Ra).^ (4/3)).^0.5;                % Eccentricity of elliptical contacts
f1 = 1 - ((Ra/Rb).^0.0602 - 1).^1.456;         % Correction factors
f2 = 1 - ((Ra/Rb).^0.0684 - 1).^1.531;
c  = (3*F*Re/(4*Ee)).^(1/3)* f1;               % Equivalent radii of contact
a  = c*(1-e.^2).^-(0.25);                      % Major radii of contact
b  = c*(1-e.^2).^(0.25);                       % Minor radii of contact
po = 3*F/(2*pi*c.^2);                          % Maximum Normal Contact stress
% Contact stiffnesses
dn = (9*F.^2/(16*Ee.^2*Re)).^(1/3)*f2;         % Normal displacement
Kn = F/dn                                      % Normal Contact stiffness
phi = 1 + (1.4 - 0.8*vg)*log(b/a);
Kt = (16*a*Ge)/(3*phi);                        % Tangential Contact stiffness
C = [1/Kt 0 0 0 0 0 ;
   0 1/Kt 0 0 0 0 ;
   0 0  1/Kn 0 0 0;
   0 0 0  1e5 0 0;
   0 0 0  0 1e5 0;
   0 0 0  0 0 1e5;];
K = inv(C);
% Stiffness of Six Beam flexure (SBF)
[K_para,C_para] = Para_stiff('paraflexdata.txt');
% Combined stiffnesses of Piezo actuator and ball-groove mount, acting in series
Kact =((1/ball_groove(F)) + (1/(2e7)))^-1;
% Add stiffnesses of SBF, acting in parallel to actuator
K_para(3,3) = K_para(3,3) + Kact ;
% Transformation to groove coordinate system
L = 0.04;
w = 0.0127;
Ang = 90-Gr_ang;
Pos_para = [   0 0 0 0 0 0;
```

```
        -L/2 -L/2 -L/2 -L/2, -L/2 -L/2;
        -w  -w  -w -w -w -w;
        Ang Ang Ang Ang Ang  Ang;
        0 0 0 0 0 0;
        0 0 0 0 0 0 ];
K_para = Tr(Pos_para,j)* K_para*Tr(Pos_para,j)';
C_para = inv(K_para);

% Add stiffnesses of ball-groove contact, acting in series
C = C + C_para;
K = inv(C);
% Calculate stiffness matrix of groove flexure
[Kflex,Cflex] = squareflex(flex_data);
% Add stiffnesses of groove flexure, acting in series
C = Cflex + C;
K = inv(C);                          % Equivalent Stiffness of Contact
% ------------------------------------ End of function ----------------------------------------
```

Para_stiff.m

```
function [Ko, Co] = Para_stiff(file_name)
% Updated 24th Nov 2004
% Function returns stiffness/compliance matrix for a Six Beam flexure
% The flexure may be considered to be made of 6 beams with fixed-guided end condition

[E,G,v,L,w,t,d,e,h] = paraflex(file_name); % Read data file
Kxx   = E*t*w/L;
Kyy   = E*t*(w^3)/(L^3);
Ky_thz = 1e20;
Kzz   = E*w*(t^3)/(L^3);
Kz_thy = 1e20;
Kthx_thx = (G/L)*(w*t^3/16)*((16/3)-3.36*(t/w)*(1-t^4/(12*w^4)));
Kthy_z  = 1e20;
Kthy_thy = E*w*t^3/(12*L);
Kthz_y  = 1e20;
Kthz_thz = E*t*w^3/(12*L);
% Stiffness and Compliance matrix for each beam
Cf = [   1/Kxx  0 0   0 0 0;
       0 (1/Kyy+L/(G*w*t)) 0   0 0 1/Kthz_y;
       0 0 (1/Kzz+L/(G*w*t)) 0 -1/Kthy_z 0;
       0 0 0 1/Kthx_thx 0 0;
       0 0 -1/Kz_thy 0 1/Kthy_thy 0;
       0 1/Ky_thz 0 0 0 1/Kthz_thz];
Kf = inv(Cf);
```

```
% Pos matrix defines moves to go from local CS to base CS
Pos = [  e/2  -e/2 e/2 -e/2 e/2 -e/2;
       0  0  0  0 0 0;
       -h  -h  -(h+d) -(h+d) -(h+2*d) -(h+2*d);
       0  0  0 0 0 0;
       0  0  0 0 0 0;
       0  180  0 180 0 180 ];
% Transformation to base coordinate system
K = cell(1,6);
C = cell(1,6);
for j =1:6
K(1,j) = {Tr(Pos,j)*Kf*(Tr(Pos,j)')};
C(1,j) = {inv(K{1,j})};
end
% Combination of beam stiffness, acting in parallel;
Ko  = K{1,1} + K{1,2} + K{1,3} + K{1,4} + K{1,5} + K{1,6};
Co  = inv(Ko);

% Referring to discussion in section x.x, a modified compliance matrix is
% input for the SBF based on the CoMeT model
% Compliance matrix based on CoMeT model
Co  = [2.865e-6, 0 , -3.5e-8, 0 , 8.924e-5, 0;
       0  , 9.848e-7, 0, -1.942e-5, 0 , -1.02e-5;
       -3.5e-8 , 0 , 1.256e-6, 0 , -1.966e-7, 0;
       0 , -3.885e-5, 0 , 9e-4 , 0, 2.22e-4;
       1.785e-4, 0 , -3.93e-7 , 0 , 6e-3, 0;
       0 , -2.03e-5, 0, 2.22e-4, 0, 1.712e-3];

Ko = inv(Co); % Stiffness of SBF
% ---------- End of function ----------
```

paraflex.m

```
function [E, G, v, L, w, t, d, e, h] = paraflex(file_name)
% Updated 24th November 2004
% Function reads geometric and mechanical properties of SBF
% Usage paraflex( inputfile_name ), e.g.paraflexdata.txt
file_id = fopen(file_name);
for i=1:6
   fgetl(file_id);
end
E = fscanf(file_id,'%f ',[1]);   % Young's modulus
G = fscanf(file_id,'%f ',[1]);   % Shear modulus
v = fscanf(file_id,'%f ',[1]);   % Poisson's ratio
```

```
L = fscanf(file_id,'%f ',[1]);   % Length
w = fscanf(file_id,'%f ',[1]);   % Width
t = fscanf(file_id,'%f ',[1]);   % Thickness
d = fscanf(file_id,'%f ',[1]);
e = fscanf(file_id,'%f ',[1]);
h = fscanf(file_id,'%f ',[1]);
fclose(file_id);
% ---------- End of function ----------
```

Structure of text file, "file_name" containing SBF data

paraflexdata.txt

Parallel Flexure: material properties and Key dimensions
Material: Aluminum 6061

```
E(Pa)  G(Pa) v(m)    L(m)   w(m)  t(m)   d(m)   e(m)   h(m)
69e9   26e9 0.28 0.02   0.01588 0.000821  0.015  0.02   0.035
% ---------- End of file----------
```

squareflex.m

function [Ko, Co, Pos] = squareflex(file_name)

```
% Updated 24th Nov 2004
% Function returns stiffness/compliance matrix for the square groove flexure
% The flexure may be considered to be made of 8 beams, two each in series
% and total of 4 pairs acting in parallel

[E,G,v,t,w,a,L,d] = sqflexdata(file_name); % Read geometric and mechanical properties
Kxx =   E*t*w/a;
Kyy =   E*w*(t^3)/(4*(a^3));
Ky_thz = E*w*t^3/(6*a^2);
Kzz   = E*t*(w^3)/(4*(a^3));
Kz_thy = E*t*w^3/(6*a^2);
Kthx_thx = (G/a)*(w*t^3/16)*((16/3)-3.36*(t/w)*(1-t^4/(12*w^4)));
Kthy_z =  E*t*w^3/(6*a^2);
Kthy_thy = E*t*w^3/(12*a);
Kthz_y =   E*w*t^3/(6*a^2);
Kthz_thz = E*w*t^3/(12*a);
% Stiffness and Compliance matrix for each beam
Cflex = [ 1/Kxx  0 0   0 0 0;
      0 (1/Kyy+a/(G*w*t)) 0   0 0 1/Kthz_y;
      0 0 (1/Kzz+a/(G*w*t)) 0 -1/Kthy_z 0;
```

```
        0 0 0     1/Kthx_thx 0 0;
        0 0 -1/Kz_thy 0 1/Kthy_thy 0;
        0 1/Ky_thz 0 0 0 1/Kthz_thz];
Kflex = inv(Cflex);
Dist = (L/2) + d  + t/2 ;
% Position Matrix
Pos = [- Dist -Dist -w/2 0 0 0
       Dist -Dist -w/2 0 0 180
       Dist -Dist -w/2 0 0 90
       Dist Dist -w/2 0 0  270
       Dist Dist -w/2 0 0  180
      -Dist Dist -w/2 0 0  0
      -Dist Dist -w/2 0 0  270
      -Dist -Dist -w/2 0 0 90];
Pos = Pos';
% Transformation to global coordinate system
K = cell(1,8);
C = cell(1,8);
for j =1:8
K(1,j) = {Tr(Pos,j)*Kflex*(Tr(Pos,j)')};
C(1,j) = {inv(K{1,j})};
end
% Combination of beams, (1,8), (2,3) , (4,5) and (6,7) in Series
C1_8 = C{1,1} + C{1,8};
K1_8 = inv(C1_8);
C2_3 = C{1,2} + C{1,3};
K2_3 = inv(C2_3);
C4_5 = C{1,4} + C{1,5};
K4_5 = inv(C4_5);
C6_7 = C{1,6} + C{1,7};
K6_7 = inv(C6_7);
% Combination of pairs 1_8, 2_3, 4_5 and 6_7 in parallel
Ko  = K1_8 + K2_3 + K4_5 + K6_7;
Co  = inv(Ko);
% ---------------------------------- End of function----------------------------------------
```

sqflexdata.m

```
function [E, G, v, t, w, a, L, d] = sqflexdata(file_name)
% Updated 24th November 2004
% Function to read in geometric and material properties of square groove flexure
% Usage [E, G, v, t, w, a, L, d] = sqflexdata(file_name)
% file_name = Text file containing data example sqflex_24oct.txt
file_id = fopen(file_name);
```

```
for i=1:5
   fgetl(file_id);
end
E = fscanf(file_id,'%f ',[1]);
G = fscanf(file_id,'%f ',[1]);
v = fscanf(file_id,'%f ',[1]);
t = fscanf(file_id,'%f ',[1]);
w = fscanf(file_id,'%f ',[1]);
a = fscanf(file_id,'%f ',[1]);
L = fscanf(file_id,'%f ',[1]);
d = fscanf(file_id,'%f ',[1]);
fclose(file_id);
% ---------- End of function----------
```

Structure of text file, "file_name" containing groove flexure data

sqflex_24oct.txt

Square Flexure: material properties and Key dimensions

E(Pa)	G(Pa)	v(m)	t(m)	w(m)	a(m)	L(m)	d(m)
69e9	26e9	0.28	0.000826	0.0127	0.01	0.024	0.002

% ---------- End of file----------

ball_groove.m

```
function Kn = ball_groove(F)
% Updated 24th Nov 2004
% function returns the stiffness of the ball-groove mount, in the direction of actuator
% motion. USAGE - Kn = ball_groove(F), F = Normal force on corresponding groove
% flexure
% Geometric and material properties
Rb1     = 2.38e-3;
Rb2  = 2.38e-3;
Eb   = 193e9;                % 316 Stainless steel ball
Gb   = 75.39e9;
vb   = 0.28;
Rg1  = -2.675e-3;            % Estimated minor radius of indentation on groove
Rg2  = -2.675e-3;            % Estimated major radius of indentation on groove
Eg   = 69e9;                 % Aluminum 6061 groove
Gg   = 26e9;
vg   = 0.28;
alpha = 90;
```

```
pi = 3.1415926;
dpreload = 0e-6;                          % Amount of displacement preload
Fg = F*0.612+(dpreload/1.225)*1e6         % Normal force at ball-groove contact
Ee = ((1-vb.^2)/Eb + (1-vg.^2)/Eg).^(-1);
Ge = ((2-vb)/Gb + (2-vg)/Gg).^(-1);
A_plusB  = 0.5*(1/Rb1 + 1/Rb2 + 1/Rg1 + 1/Rg2);
B_minusA = 0.5*((1/Rb1 - 1/Rb2).^2 + (1/Rg1 - 1/Rg2).^2 + 2*(1/Rb1 - 1/Rb2)*(1/Rg1
- 1/Rg2)*cos(2*alpha*pi/180)).^0.5;
Ra = ( A_plusB - B_minusA).^-1;
Rb = ( A_plusB + B_minusA).^-1;
Re = (Ra * Rb).^0.5;
e  = (1- (Rb/Ra).^ (4/3)).^0.5;           % Eccentricity of elliptical contacts
f1 = 1 - ((Ra/Rb).^0.0602 - 1).^1.456;    % Correction factors
f2 = 1 - ((Ra/Rb).^0.0684 - 1).^1.531;
c  = (3*Fg*Re/(4*Ee)).^(1/3)* f1;         % Equivalent radii of contact
a  = c*(1-e.^2).^-(0.25);                 % Major radii of contact
b  = c*(1-e.^2).^(0.25);                  % Minor radii of contact
po = 3*Fg/(2*pi*a*b);                     % Maximum Normal Contact stress
% Contact stiffnesses
dn = (9*Fg.^2/(16*Ee.^2*Re)).^(1/3)*f2;   % Normal displacement
Kn = 2*Fg/dn                              % Net stiffness in direction of actuation
% ------------------------------------ End of file----------------------------------------
```

Appendix D - Displacement test results

This appendix presents the complete test data for the large displacement tests discussed in Section 5.3.1 and 5.3.2. Figure D.1 presents data for six-axis displacement tests without fixture position feedback. Figure D.2 presents data for six-axis displacement tests with fixture position feedback.

X			Parasitics					
Theory microns	Experiment microns	Error %	x microns	y microns	z microns	qx mradians	qy mradians	qz mradians
-20.000	-19.780	-1.1	—	0.389	1.232	8.88	-6.31	5.58
-10.000	-10.280	2.8	—	-0.067	0.020	2.89	4.05	1.31
0.000	0.000	0.0	—	0.000	0.000	0.00	0.00	0.00
10.000	9.265	-7.3	—	-0.050	-0.456	0.45	2.23	-3.94
20.000	19.697	-1.5	—	-0.069	-0.455	-0.42	0.70	-1.64

Y			Parasitics					
Theory microns	Experiment microns	Error %	x microns	y microns	z microns	qx mradians	qy mradians	qz mradians
-20.000	-19.520	2.5	0.097	—	0.040	0.58	-5.04	1.54
-10.000	-9.767	2.4	-0.105	—	0.081	-4.93	-4.53	-0.07
0.000	0.000	0.0	0.000	—	0.000	0.00	0.00	0.00
10.000	8.921	12.1	-0.175	—	-0.081	-7.27	-4.53	1.48
20.000	18.858	6.1	-0.130	—	0.082	-3.19	-2.52	-0.33

Z			Parasitics					
Theory microns	Experiment microns	Error %	x microns	y microns	z microns	qx mradians	qy mradians	qz mradians
-40.000	-40.239	-0.6	-0.695	0.435	40.324	-0.708	9.268	-4.76
-20.000	-19.553	2.3	-0.450	0.373	18.999	2.857	4.103	-5.58
0.000	0.000	0.0	0.000	0.000	0.000	0.000	0.000	0.00
20.000	18.999	5.3	-0.132	-0.214	-19.553	1.883	-3.697	0.49
40.000	40.324	-0.8	0.005	-0.487	-40.239	-1.095	-9.103	1.64

θx			Parasitics					
Theory microns	Experiment microns	Error %	x microns	y microns	z microns	qx mradians	qy mradians	qz mradians
-400.000	-409.455	2.4	-0.278	0.389	-0.708	—	1.412	5.64
-200.000	-194.969	-2.5	-0.092	0.390	0.055	—	0.917	1.80
0.000	0.000	0.0	0.000	0.000	0.000	—	0.000	0.00
200.000	195.522	-2.2	0.071	-0.494	0.015	—	-0.371	-2.79
400.000	404.491	1.1	0.327	-0.646	0.605	—	-1.865	-6.40

θy			Parasitics					
Theory microns	Experiment microns	Error %	x microns	y microns	z microns	qx mradians	qy mradians	qz mradians
-400.000	-388.120	3.1	-0.480	0.304	-0.132	-6.69	—	0.98
-200.000	-182.111	9.8	-0.519	0.379	-0.157	-0.93	—	-0.66
0.000	0.000	0.0	0.000	0.000	0.000	0.00	—	0.00
200.000	188.457	6.1	0.311	0.175	0.013	1.06	—	-0.98
400.000	398.729	0.3	0.277	0.313	-0.175	5.80	—	-1.31

θz			Parasitics					
Theory microns	Experiment microns	Error %	x microns	y microns	z microns	qx mradians	qy mradians	qz mradians
-200.000	-200.459	-0.2	0.082	-0.637	0.670	-5.670	1.284	—
-100.000	-96.785	3.3	-0.006	-0.289	0.033	-1.702	2.454	—
0.000	0.000	0.0	0.000	0.000	0.000	0.000	0.000	—
100.000	95.801	4.4	-0.052	0.363	-0.033	4.309	0.082	—
200.000	198.163	0.9	0.022	0.615	-0.475	2.792	-3.340	—

Figure D.1: Six-axis displacement test data (without fixture position feedback)

X			Parasitics					
Theory microns	Experiment microns	Error %	x microns	y microns	z microns	θx μradians	θy μradians	θz μradians
-20.00	-19.96	0.2	—	-0.37	0.99	7.7	4.3	-2.3
-10.00	-10.02	-0.2	—	0.07	0.99	1.6	-7.1	-1.3
0.00	0.00	0.0	—	0.00	0.00	0.0	0.0	0.0
10.00	9.96	0.4	—	0.13	0.01	1.0	-1.7	-1.0
20.00	19.96	0.2	—	0.23	0.22	-1.1	-7.1	-0.7

Y			Parasitics					
Theory microns	Experiment microns	Error %	x microns	microns	z microns	θx μradians	θy μradians	θz μradians
-20.00	-20.09	0.5	0.43	—	-0.10	11.6	-12.1	-2.3
-10.00	-10.03	0.3	0.14	—	-0.42	6.3	-7.3	-1.1
0.00	0.00	0.0	0.00	—	0.00	0.0	0.0	0.0
10.00	9.92	-0.8	-0.33	—	0.05	-15.8	5.2	1.7
20.00	19.93	-0.4	-0.48	—	0.46	-24.8	12.8	1.7

Z			Parasitics					
Theory microns	Experiment microns	Error %	x microns	y microns	z microns	θx μradians	θy μradians	θz μradians
-40.00	-40.09	0.2	0.17	-0.58	—	-4.2	-6.7	2.3
-20.00	-20.05	0.3	0.12	-0.32	—	-3.1	-1.7	0.7
0.00	0.00	0.0	0.00	0.00	—	0.0	0.0	0.0
20.00	19.95	-0.3	-0.20	0.33	—	6.8	4.3	-0.3
40.00	39.94	-0.1	-0.30	0.68	—	9.1	7.4	-0.3

θx			Parasitics					
Theory microns	Experiment microns	Error %	x microns	y microns	z microns	θx μradians	θy μradians	θz μradians
-400.0	-401.6	-0.4	-0.27	0.66	-0.86	—	3.0	5.9
-200.0	-201.5	-0.7	-0.17	0.39	-0.65	—	0.6	2.0
0.0	0.0	0.0	0.00	0.00	0.00	—	0.0	0.0
200.0	198.8	0.6	0.01	-0.34	1.59	—	1.0	-0.7
400.0	400.1	0.0	0.22	-0.73	2.01	—	-0.3	-1.3

θy			Parasitics					
Theory microns	Experiment microns	Error %	x microns	y microns	z microns	θx μradians	θy μradians	θz μradians
-400.0	-402.0	0.5	-0.18	-0.41	-0.58	-12.6	—	4.3
-200.0	-199.7	-0.2	-0.20	-0.07	-0.29	-5.0	—	2.0
0.0	0.0	0.0	0.00	0.00	0.00	0.0	—	0.0
200.0	200.1	0.1	-0.04	0.13	0.25	0.1	—	-0.3
400.0	400.6	0.1	0.14	0.09	0.47	0.7	—	-1.3

θz			Parasitics					
Theory microns	Experiment microns	Error %	x microns	y microns	z microns	θx μradians	θy μradians	θz μradians
-200.0	-200.8	0.4	-0.04	-0.69	2.10	-2.9	8.3	—
-100.0	-99.7	-0.3	-0.02	-0.25	1.74	2.1	3.3	—
0.0	0.0	0.0	0.00	0.00	0.00	0.0	0.0	—
100.0	100.1	0.1	0.02	0.31	-0.24	4.4	1.4	—
200.0	200.5	0.2	0.05	0.70	-0.44	7.7	-5.3	—

Figure D.2: Six-axis displacement test data (with fixture position feedback)